The development and applications of STEM ptychography using direct electron detectors

Colum O'Leary
Hertford College
University of Oxford

A thesis submitted for the degree of
Doctor of Philosophy

June 24, 2020

Abstract

Since the introduction of direct electron detectors to scanning transmission electron microscopy (STEM), electron ptychography – a technique which utilises the interference in diffraction patterns to reconstruct the sample-induced phase changes of a transmitted electron wave – has significantly extended the capabilities of electron microscopy. However, a number of limitations to electron ptychography exist, namely the poor contrast transfer for low and high spatial frequencies to the phase reconstruction, and the relatively slow detector speeds used to acquire the ptychographic data ($\sim$ 1,000 fps). In this thesis, a number of strategies are introduced to further improve the robustness and dose-efficiency of focused-probe electron ptychography (FPP), after which several applications of FPP techniques are demonstrated.

Firstly, the contrast transfer properties of single side-band (SSB) ptychography are experimentally measured from an amorphous carbon sample in order to determine the optimal experimental parameters for ptychography. It is demonstrated that the probe convergence semi-angle can be used to tune the phase-contrast transfer function (PCTF) for each experiment, such that the relevant sample information is transferred with high contrast. Furthermore, careful consideration of the noise in the ptychographic data can provide an enhanced PCTF which broadens the transfer window in the image plane. These strategies are combined with a 1-bit fast (12,500 fps) acquisition scheme to enable the atomic-resolution phase reconstruction of a beam-sensitive zeolite sample using a low electron dose of 1.0×10^5 e^- nm^{-2}.

By implementing these experimental and analytical strategies, the efficiency of FPP techniques can be significantly improved.

At the end of this thesis, several experimental challenges common to STEM are overcome using electron ptychography. Firstly, the precision of phase reconstructions are improved considerably by increasing the electron dose via multi-frame image acquisition, hence avoiding the slow-scan instabilities inherent to long STEM acquisition times. Furthermore, three-dimensional analysis of an unknown graphene defect is performed using a single ptychographic data set. Finally, electron ptychography is used to visualise oxygen vacancies in uranium dioxide for the first time.

Dedicated to my sister, Eilís

Acknowledgements

Firstly, I would like to thank my supervisors, Professors Peter Nellist and Angus Kirkland, for their consistent mentoring and advice during my DPhil studies. I am very grateful to Dr Gerardo Martinez and Dr Emanuela Liberti for their teaching and support; and to Dr Laura Clark, Emma Hedley and Dr Zezhong Zhang for providing constructive feedback and advice on my thesis writing. I would also like to thank the fellow members (past and present) of both research groups, the DCCEM facility staff and the ePSIC staff at Diamond Light Source. Finally, I would like to give special thanks to my family, my friends and Crystal for their constant encouragement and support, without whom this thesis would not exist.

Disclaimer

I hereby declare that this thesis is my own original work and was solely undertaken during my DPhil studies at the University of Oxford. I have acknowledged all main sources of help. Where the work in the thesis is based on a collaboration with others, I have explicitly stated what work was done by me, and what was done by others. For all the images used in this thesis which are not my own, I have received permission from the copyright holders and accredited them in the figure captions. I have clearly cited those research works that I have consulted throughout my work.

List of outputs

Peer-reviewed journal articles

[1] **C. M. O'Leary**, C. S. Allen, C. Huang, J. S. Kim, E. Liberti, P. D. Nellist and A. I. Kirkland, "Phase reconstruction using fast binary 4D STEM data", *Applied Physics Letters*, vol. 116, no. 12, p. 124101, 2020.

[2] T. Chen, I. Ellis, T. J. N. Hooper, L. Ye, B. Lo, **C. O'Leary**, A. A. Sheader, G. T. Martinez, L. Jones, P. Ho, P. Zhao, J. Cookson, P. T. Bishop, P. Chater, J. V. Hanna, P. D. Nellist and S. C. E. Tsang, "Interstitial Boron Atoms in Palladium Lattice of Industrial Type of Nano-catalyst: Direct Visualization, Properties and Structural Modifications", *Journal of Applied Chemical Sciences*, vol. 141, no. 50, pp. 19616–19624, 2019.

[3] J. Fatermans, A. J. den Dekker, K. Müller-Caspary, I. Lobato, **C. M. O'Leary**, P. D. Nellist and S. Van Aert, "Single Atom Detection from Low Contrast-to-Noise Ratio Electron Microscopy Images", *Physical Review Letters*, vol. 125, no. 5, p. 056101, 2018.

Pre-prints

[1] G. T. Martinez, T. C. Naginey, L. Jones, **C. M. O'Leary**, T. J. Pennycook, R. J. Nicholls, J. R. Yates, P. D. Nellist, "Direct Imaging of Charge Redistribution due to Bonding at Atomic Resolution via Electron Ptychography", arXiv:1907.12974 [cond-mat.mtrl-sci], 2019.

Conference proceedings

[1] **C. M. O'Leary**, E. Liberti, S. M. Collins, D. N. Johnstone, M. Rothmann, J. Hou, C. S. Allen, J. S. Kim, T. D. Bennett, P. A. Midgley, A. I. Kirkland, and P. D. Nellist, "Electron Ptychography Using Fast Binary 4D STEM Data", *Microscopy and Microanalysis*, vol. 25, no. S2, pp. 1662–1663, 2019.

[2] **C. M. O'Leary**, G. T. Martinez, E. Liberti, M. J. Humphry, A. I. Kirkland, and P. D. Nellist, "Contrast Transfer and Noise Minimization in Electron Ptychography", *Microscopy and Microanalysis*, vol. 25, no. S2, pp. 64–65, 2019.

[3] M. Huth, R. Ritz, **C. M. O'Leary**, I. Griffiths, P. Nellist, and H. Soltau, "Ultrafast Ptychography with 7500 Frames per Second," *Microscopy and Microanalysis*, vol. 25, no. S2, pp. 40–41, 2019.

[4] E. Liberti, G. T. Martinez, **C. M. O'Leary**, P. D. Nellist, and A. I. Kirkland, "Three-dimensional Electron Ptychography of Catalyst Nanoparticles using Combined HAADF STEM and Atom Counting," *Microscopy and Microanalysis*, vol. 25, no. S2, pp. 8–9, 2019.

[5] T. J. Pennycook, G. T. Martinez, **C. M. O'Leary**, H. Yang, and P. D. Nellist, "Efficient Phase Contrast Imaging via Electron Ptychography, a Tutorial," *Microscopy and Microanalysis*, vol. 25, no. S2, pp. 2684–2685, 2019.

[6] P. D. Nellist, G. T. Martinez, **C. O'Leary**, and L. Jones, "Exploring the Limits of Focused-Probe STEM Ptychography," *Microscopy and Microanalysis*, vol. 24, no. S1, pp. 190–191, 2018.

Contents

List of Figures

Chapter 1

Overview

From its conception by Ernst Ruska and Max Knoll in 1931 to the present day, transmission electron microscopy (TEM) has become a vital tool for materials characterisation. Modern electron microscopes can routinely perform atomic-resolution imaging, nanoscale spectroscopic mapping and a plethora of diffraction experiments. These techniques have provided solutions to many of the world's most pressing scientific problems, such as the investigation of COVID-19 [1, 2], performance testing of renewable energy devices [3, 4], and the search for robust materials for aerospace applications [5, 6]. However, not all materials can be easily imaged in a transmission electron microscope.

Some materials contain low-Z elements which interact weakly with the electron beam and provide little evidence of their presence in the resultant image. Other materials are sensitive to electron radiation and, as a result, are easily damaged under the electron beam. In order to image these materials, two aspects of TEM imaging must be developed: 1) fast detectors which are sensitive to single-electron events, and 2) data processing techniques which can provide meaningful structural characterisation using as few electrons as possible.

Over the last decade, a new family of low-noise, fast, modern detectors, known as *direct electron detectors*, have been developed for use in electron microscopy [7–11]. The subsequent improvement in TEM detection sensitivity has created a demand for processing techniques which can use this data as effectively as possible. One candidate technique is *electron ptychography* – using the interference information recorded by a detector, the phase changes to the electron wave introduced by a material can be reconstructed [12–14]. The phase is sensitive to very slight disturbances and can be detected using low electron flux, enabling atomic-resolution phase mapping of light elements and radiation-sensitive materials [15–17]. Although electron ptychography has been successfully applied to several challenging materials over the last decade [18–20], there exist a number of factors which limit its performance. These include the slow speed of direct electron detectors in comparison to conventional detectors for scanning TEM applications, and the restricted image contrast obtainable using electron ptychography.

In this thesis, I further develop the techniques of electron ptychography using direct electron detectors in scanning transmission electron microscopy. In the subsequent chapters, the context of electron ptychography will be outlined, including its limitations, before describing several technical developments which have been achieved in the course of this research. Finally, the application of ptychographic techniques will be demonstrated in order to overcome a variety of experimental challenges. The structure of this thesis is as follows:

- Chapter 2 contains an introduction to ptychography and its context within conventional transmission electron microscopy (CTEM) and scanning transmission electron microscopy (STEM). The applications and limitations of ptychography are discussed.

- Chapter 3 contains a mathematical description of four-dimensional (4D) STEM,

with further detail on two specific focused-probe electron ptychography methods: single side-band (SSB) and Wigner distribution deconvolution (WDD).

- Chapter 4 describes the experimental, analytical and computational methods required to perform electron ptychography. It is hoped that the reader can use this as a manual to replicate electron ptychography in their own laboratory.

- Chapter 5 provides a description and an experimental demonstration of the contrast transfer properties of electron ptychography.

- Chapter 6 builds upon the existing contrast transfer theory to account for noise in the data, in order to improve ptychographic imaging efficiency.

- Chapter 7 presents a solution to the slow acquisition speeds of direct electron detectors via binary data acquisition. The application of electron ptychography to the resultant data is demonstrated.

- Chapter 8 demonstrates three applications of electron ptychography, each of which overcome particular challenges that exist for many common STEM imaging techniques.

- Chapter 9 highlights the conclusions of this work. Several avenues of future work are proposed.

- Appendix A contains a glossary of terms for the reader to reference while reading this thesis.

- Appendix B provides a detailed mathematical description of the post-processing aberration correction procedure for SSB and WDD ptychography.

Chapter 2

Literature review

This chapter contains a review of the literature relevant to transmission electron microscopy, in order to aid the reader's understanding of subsequent chapters. Firstly, conventional and scanning transmission electron microscopy (CTEM and STEM) will be introduced, and their impact on science and technology will be highlighted. Next, electron scattering theory will be reviewed, highlighting the significance of the sample information encoded in the phase of transmitted waves. Common STEM imaging methods will then be discussed, before introducing adaptive reconstruction techniques which can solve for the phase of the transmitted wave. Particular emphasis will be placed on focused-probe electron ptychography, as this is the focus of subsequent chapters.

2.1 Introduction

Transmission electron microscopy has played a significant role in the development of research fields including nanotechnology, renewable energy and medicine, enabling characterisation of a cornucopia of materials. Nanoscale imaging and diffraction provide insights into the crystallography of materials [21]; spectroscopic capabilities allow the determination of the elemental composition of complex structures [22]; and modern instruments can provide high-resolution imaging of 2D materials [23, 24], nanoparticles [20, 25], proteins [26], viruses [27] and more.

There are two common instrumental geometries in transmission electron microscopy, both of which provide unique capabilities for nanocharacterisation: conventional transmission electron microscopy (CTEM) and scanning transmission electron microscopy (STEM).

2.1.1 CTEM imaging

In the case of CTEM as shown in Figure 2.1, electrons are emitted from a source and accelerated up to a significant fraction of the speed of light (i.e. $0.5\,c$ for 80 keV electrons). Electrons with kinetic energies of 80–300 keV possess characteristic wavelengths of $\sim$ 2–4 pm. This corresponds to a diffraction-limited resolution of approximately 1–2 pm – 100,000 times better than that for visible light microscopy. However, the practical resolution limit of TEM is much poorer than that determined by diffraction, such that most TEM instruments in the 20$^{\text{th}}$ century could only provide imaging resolution on the order of nanometres. Fortunately, there have been several advances in TEM instrumentation over the last half-century which have led to the development of modern instruments with imaging resolutions greater than 0.1 nm. These developments will be discussed in further detail throughout this chapter.

The electrons pass through a series of electromagnetic lenses – carefully shaped circularly symmetric electromagnets which use the Lorentz force to deflect the electrons. In this way, the electrons can be focused into a parallel or convergent beam, and be directed along the microscope column. Unlike optical microscopy, the focal length of an electromagnetic lens is smoothly tunable by adjusting the current. As such, a variety of experimental configurations can be realised, some of which will be discussed in further detail throughout this thesis.

Before the electron beam is transmitted through the sample, it passes through a condenser lens system, which typically consists of two or three separate lenses. For the schematic shown in Figure 2.1, condenser lens 1 is used to image the source in the front focal plane of condenser lens 2, which creates a broad parallel beam at the sample plane.

Following transmission through a thin (<100 nm) sample, the electrons pass through an *objective lens* which forms a real image of the object. The objective lens is the most important lens in a transmission electron microscope, not only because it forms the image of the object, but also because it accepts the largest range of angular scattering and thus the image formation process is most vulnerable to the effects of lens imperfections at this point. An objective lens aperture can be used to control the scattering which contributes to image formation. For example, the angular range of scattering can be limited by a circular aperture to prevent divergent electron paths from contributing to high-resolution images; specific diffracted beams can be centred within the aperture in order to form an image of a particular crystallographic feature; and structured apertures can give rise to spiralling electron wavefronts which possess angular momentum.

Next, the intermediate and projector lenses magnify the image formed by the objective lens and project the electrons onto a pixellated detector (e.g. CCD, CMOS). The intensity of the electron wave on the detector provides a highly magnified image of the sample. For high-resolution applications using modern instruments, this mode of imaging is known as high-resolution TEM (HRTEM).

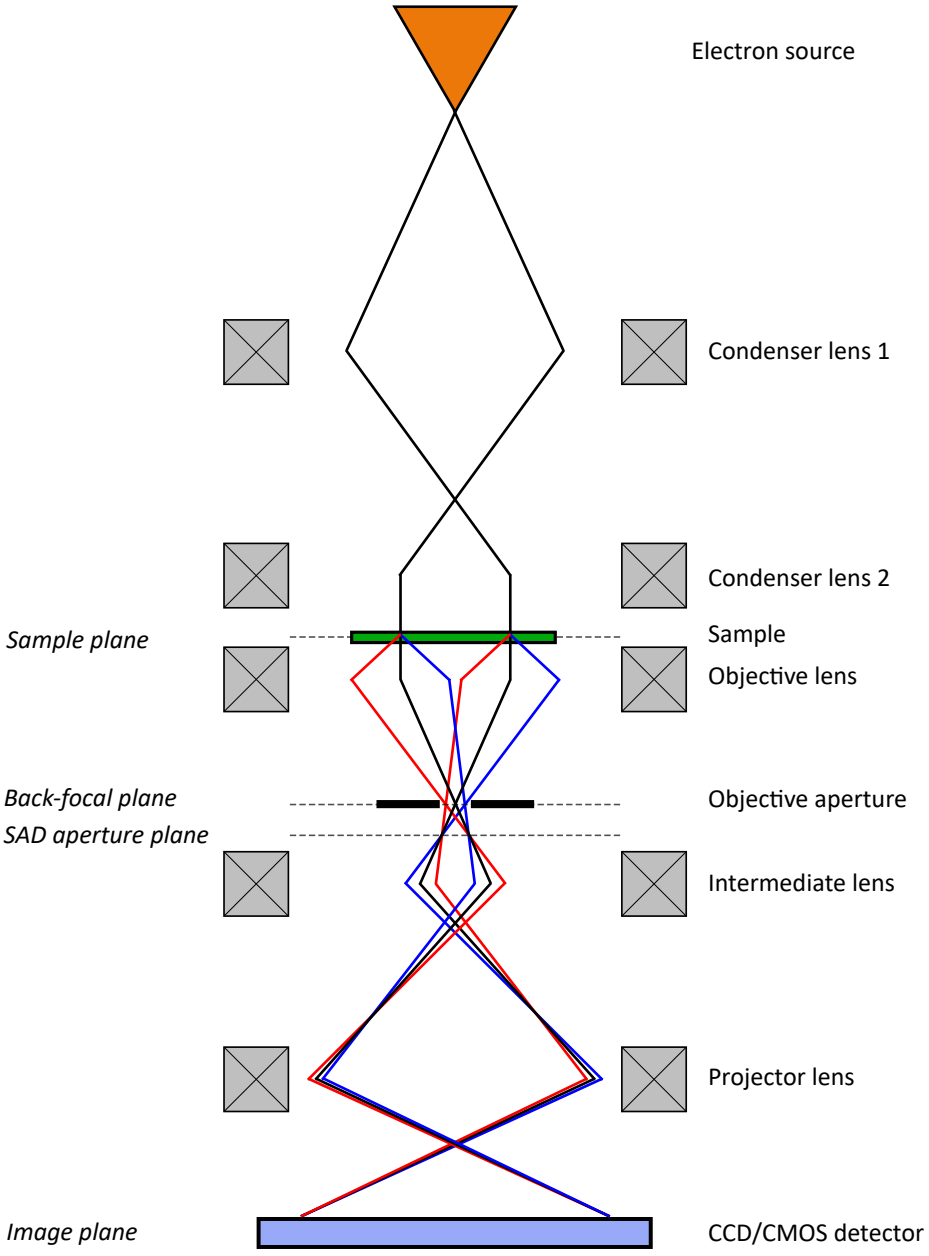

Figure 2.1: Basic schematic of conventional transmission electron microscopy (CTEM). A beam of electrons is accelerated down the microscope column. The condenser lens system creates a broad parallel beam which is transmitted through the sample. Most electrons do not interact with the sample upon transmission (black paths) while others are scattered (red and blue paths). An objective lens focuses the electrons in the back-focal plane, where an objective aperture can limit the angular range of electrons that contribute to image formation. Finally, the intermediate and projector lenses produce a magnified image of the sample on a CCD or CMOS detector. The strength of the intermediate lens can be changed to form a diffraction pattern on the detector. In order to select a specific sample region on which to obtain a diffraction pattern, a selected area aperture can be inserted into the image plane of the objective lens.

2.1.2 CTEM diffraction

Real-space imaging is one of an array of CTEM experiments which can be performed. In the case of CTEM with a broad parallel beam of electrons, incident plane waves which are transmitted through a crystalline sample are focused by the objective lens into an array of *diffraction spots* in the back-focal plane. An objective aperture is sometimes placed in this plane to mitigate the effects of lens imperfections on the formation of an image (Section 2.1.1). Each of these diffraction spots represent a set of crystal lattice planes, and can provide valuable information about sample structure and orientation. The intermediate lens strength (Figure 2.1) can be changed such that the array of diffraction spots, known as the *diffraction pattern*, of a sample section can be projected onto a pixellated detector at the bottom of the microscope column. A selected area aperture, located in a real-space plane below the objective lens, can be used to study the diffraction pattern of a specific sample region. As a result, this technique is generally known as selected area electron diffraction (SAD, or SAED) [28]. The SAD technique is commonly used to determine crystal structure, orientation and defect geometry [28, 29].

By converging the parallel beam, the range of angles of incidence increases such that the diffraction spots broaden into discs in the back-focal plane, forming a convergent beam electron diffraction (CBED) pattern. The CBED patterns in CTEM can be analysed to determine additional sample information that cannot be obtained using parallel diffraction techniques, such as crystal symmetry, structure factors and lattice strains [30, 31]. The CBED pattern also plays a vital role in the formation of images in another configuration of TEM, known as scanning TEM (STEM). The basic principles of STEM are now discussed.

2.1.3 STEM imaging

In many TEM instruments, the strength of the lenses can be adjusted such that one can form a scanning TEM (STEM) configuration. A basic schematic of a TEM instrument in STEM mode is illustrated in Figure 2.2. The 'objective lens' is located above the sample plane, and is known as the *condenser* in CTEM/STEM instruments. The condenser converges the electron beam into a *probe* on the sample [28, 32]. For modern STEM instruments, the probe diameter is on the order of 0.1 nm for atomic-resolution imaging [33]. This probe is then scanned in a raster across a region of interest using a set of scanning coils. Once transmitted through a crystalline sample, the electron beam is scattered and forms a CBED pattern in the detector plane as shown in Figure 2.2. When a large objective aperture is used (or alternatively, if no aperture is used), this is also referred to as a *ronchigram*, named after Vasco Ronchi for his work on the determination of optical aberrations [34].

Typically, single channel detectors integrate over a region of the detector plane at each position in a 2D scan, to produce an 'image' of the specimen [33]. The nature of the resulting image is dependent on the geometry of the detector. For example, disc-shaped bright-field (BF) detectors collect a small circular region of the CBED pattern close to the optic axis, providing an imaging method whose contrast is dependent on the interference between direct and diffracted electron beams. Conversely, annular dark-field (ADF) detectors collect signal from high-angle electron scattering which can be used to provide images with contrast that is not dependent on interference effects. Instead, the image contrast can be directly related to the composition and thickness of a sample [35]. The theory behind these imaging methods will be discussed in further detail in Sections 2.2.2 and 2.3.

Alternatively, each CBED pattern can be recorded on a pixellated detector, after

which post-processing is performed on the data to form images [36]. This method of data acquisition is essential for STEM ptychography, and will be discussed in detail throughout this thesis.

2.1.4 Relationship between CTEM and STEM configurations

It should be noted that there is a strong relationship between the CTEM and STEM configurations. In 1969, Cowley demonstrated that, if the positions of the source and detector in a CTEM setup are switched, one would obtain a STEM setup [37]. This is known as the *principle of reciprocity*. Although only strictly true for elastic scattering, the principle of reciprocity has been frequently used to compare imaging modalities in the CTEM and STEM, and can be useful to determine whether CTEM or STEM is more suited to a specific materials characterisation problem [38–41]. This is an important factor to consider in electron ptychography, and will be discussed in further detail at the end of this literature review.

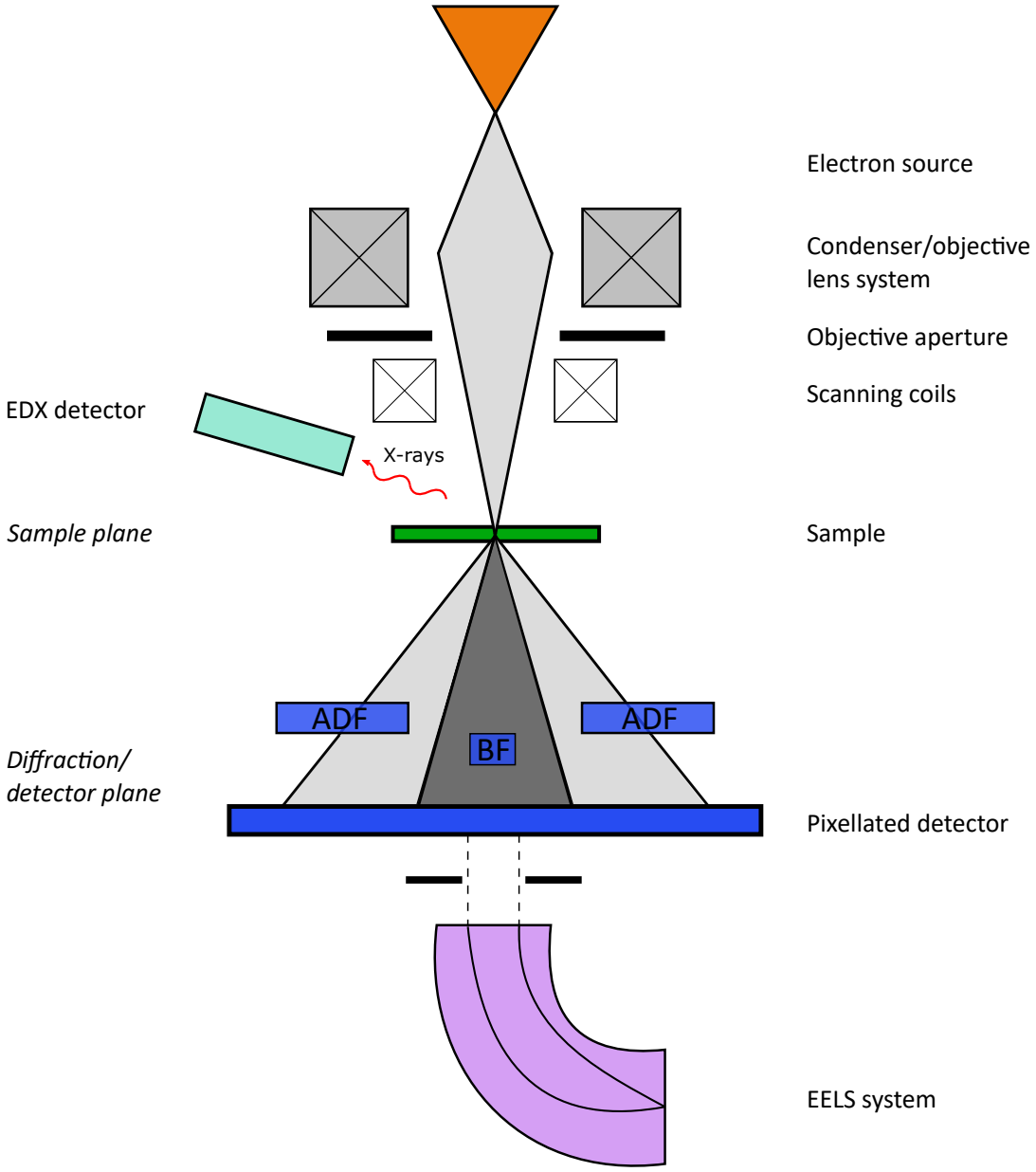

Figure 2.2: Basic schematic of scanning transmission electron microscopy (STEM). The condenser/objective lens system converges the beam into a sub-nanometre probe on the sample. The scanning coils move the probe in a raster across the sample. The bright-field (BF) detector collects the most coherent electrons, while the annular dark-field (ADF) detector collects electrons scattered to high angles. An energy-dispersive X-ray (EDX) detector, inclined at an angle above the sample, collects characteristic X-rays which can be used to map elemental composition. The electron energy-loss spectrometer can be used to acquire an energy spectrum of the transmitted beam to analyse the chemical and electronic fine structure of materials.

2.1.5 Spectroscopic techniques

Many CTEM and STEM instruments possess spectrometers for compositional analysis and electronic structure determination. The most common spectroscopic techniques include energy-dispersive X-ray spectroscopy (EDX, or EDS, or EDXS) and electron energy-loss spectroscopy (EELS).

EDX involves the detection of characteristic X-rays from the specimen due to the electron beam. The high energy incident electrons (10^2–10^3 keV) induce electron excitations within the sample, the decay of which leads to the emission of characteristic X-rays which can be used to determine elemental composition [22]. The EDX detector is located above the sample plane and away from the optic axis to avoid blocking the electron beam, such that STEM imaging and spectroscopy can be performed simultaneously [42]. The detector is inclined at a specific *take-off angle* to optimise collection efficiency ($\sim$20° for modern STEM instruments) [43]. A spectrum can be obtained for each probe position in a STEM scan, or alternatively, the average spectrum of the entire STEM scan can be plotted. EDX acquisition can also be performed using CTEM to obtain an average spectrum of a particular field of view [44].

Electron energy-loss spectroscopy (EELS) involves acquiring a spectrum of electron energies after transmission through the sample using a magnetic prism [45, 46]. The energy differences between the incident and inelastically scattered electrons can be related to the electronic structure of the atoms in the sample. In the case of STEM, this allows for a point-by-point chemical and electronic state mapping of the sample, including for example, the local oxidation state in complex oxides [47] and bimetallic catalyst nanoparticles [48]. The EELS detector is placed below the imaging detectors, such that annular detector imaging and EELS acquisition can be performed simultaneously [42]. In addition, energy filters can be used in CTEM and STEM

configurations to choose a specific energy range of electrons that contribute to image formation. This is known as energy filtered TEM (EFTEM), and has applications in both life sciences and physical sciences [43, 49, 50].

2.1.6 Challenging materials

Despite the wealth of experimental techniques already discussed, CTEM and STEM methods are not universally applicable to all materials. This is mainly due to the damage of the sample by the incident electrons. The high voltage electron beam can displace atoms, break bonds and cause major structural changes to materials [51]. This sensitivity to electron radiation leads to limits on the electron dose (electrons per unit area) or dose rate for image acquisition, which in turn limit the achievable image resolution. For the case of samples containing light elements such as lithium and carbon, the restrictions on electron dose are compounded by weak scattering, thus limiting the contrast obtainable without damaging the structure for many imaging techniques [51, 52]. Low-dose spectroscopy is even more difficult to perform, as the probabilities of signal collection (*scattering cross-section* [33]) for EDX and EELS detection are much smaller than for ADF imaging [53, 54]. To maximise the contrast and dose-efficiency (i.e. the amount of sample information obtainable at a given dose) of electron imaging, one must first understand the scattering processes present in electron microscopy, and the imaging methods that utilise the scattered electrons.

2.2 Scattering, coherence and imaging

Electron scattering processes are the fundamental source of contrast in CTEM and STEM imaging. Due to the Coulomb force, the probability of electron-specimen interactions is much greater than that of photon-specimen interactions. As such, the

likelihood of multiple scattering in electron microscopy is much higher than for X-ray or optical microscopy, putting stricter requirements on sample thickness [28]. To avoid the effects of multiple scattering, samples in CTEM and STEM rarely exceed 100 nm, and if the sample is very thin, image interpretation simplifies dramatically [55].

Regardless of sample thickness, the nature of the illumination and image formation process, in particular the *coherence*, will influence the information that can be obtained from an experiment, and should be understood in detail. In the following sections, electron scattering and coherence in the context of TEM will be discussed, with particular emphasis on how they affect the formation of images for thin samples.

2.2.1 Elastic and inelastic scattering

The mechanisms by which the incident electrons are scattered by the sample in TEM are generally separated into two categories: elastic and inelastic scattering. If an electron is scattered by a sample but does not lose energy in the process, it is said to be elastically scattered. The mean free path of elastic scattering, λ_{el}, represents the sample thickness below which plural scattering of single electrons can be neglected. For most elements in the periodic table, λ_{el} varies between 10 nm and 80 nm [56].

If an electron loses energy upon transmission through the sample, it is said to be inelastically scattered [33]. The probability of inelastic scattering processes is characterised by the inelastic mean free path, λ_{in}, defined as the average distance that an electron travels within a particular sample between consecutive inelastic scattering events [56]. For most common crystal structures, λ_{in} is on the order of 100 nm [21]. However, it has recently been shown that low-loss inelastic scattering is non-negligible at sample thicknesses as low as 10 nm [57].

Both elastic and inelastic scattering can provide valuable sample information. For example, elastic scattering is commonly used for coherent imaging techniques [35], while inelastic scattering can be used to determine electronic structure using electron energy loss spectroscopy (EELS), or to map specific elements in a sample using energy-filtered TEM (EFTEM) (Section 2.1.5) [46]. For the research shown in this thesis, the samples are sufficiently thin ($\leq$10 nm) such that the effects of inelastic and plural scattering of high-energy TEM electrons (30 – 300 keV) can be neglected.

2.2.2 Coherence

The coherence of an electron microscopy experiment is defined by the ability to observe interference effects due to scattering. This is dependent on both the spatial origin of the electrons (known as *spatial* coherence) and the energy of the electrons (known as *temporal* coherence). There are several factors which limit the degree of spatial and temporal coherence in CTEM and STEM imaging, some of which will be described below.

2.2.2.1 Effects of electron source

For a perfectly coherent imaging mode, an infinitesimally small, monochromatic electron source is required such that each electron is emitted from the same point of the source and with the same energy. In this case, the electron waves emitted from the source are both fully spatially and temporally coherent. However, due to their finite size, practical electron sources are only partially spatially coherent [33]. The extent of spatial coherence is defined by a parameter known as the *coherence width*. In HRTEM, sample features with spacings smaller than the coherence width are imaged coher-

ently [58]. Furthermore, the finite energy spread of electrons from practical sources gives rise to partial temporal coherence, the extent of which is defined by a characteristic *coherence length*. Both spatial and temporal coherence produce envelopes (discussed in further detail in Section 2.2.4) which ultimately limit the obtainable resolution of HRTEM and STEM experiments.

2.2.2.2 Sample and detector incoherence

Once the partially coherent electron wave has been emitted from the source, there are several other factors which can affect the coherence. Upon transmitting the sample, the coherent intensity of the electron wave is further reduced by the inelastic scattering of electrons. The detector geometry can also affect the coherence of TEM, particularly in the case of STEM. The coherence of STEM imaging is dependent on the relationship between the convergence semi-angle of the electron probe (typically 5-40 mrad) and the geometry of the detector [33]. To achieve a coherent imaging mode using STEM, a small integrating detector is typically used to collect only the signal from the central region of the CBED pattern, i.e. within 20% of the bright-field disc radius. This imaging mode is known as bright-field (BF) STEM, and is the STEM-equivalent of coherent HRTEM imaging. In this way, the interference effects present in the overlap of the diffracted discs can be recorded [35]. However, if the detector covers most, or all, of the bright-field disc, an incoherent bright-field (IBF) imaging mode is realised where the interference effects are averaged over and hence do not contribute to image formation [33]. Referring to the principle of reciprocity, increasing the detector collection angle in STEM is the equivalent to using a source with greater beam divergence in CTEM. In 1974, Misell and co-workers described how one could collect and integrate the entire CBED pattern at each probe position in a STEM scan to provide a perfectly incoherent imaging mode, i.e. zero image

contrast for an electron-transparent sample [59]. Alternatively, an annular detector can be used to collect only the electrons scattered to high angles. This detector geometry, known as annular dark-field (ADF), has been used to provide a high-resolution quantitative incoherent imaging technique for beam resilient samples. The contrast approaches a Z^2 dependence for Rutherford scattering of unscreened atomic nuclei, enabling quantification of contrast from atomic columns. In practice, the contrast is approximately proportional to $Z^{1.7}$ due to the screening of the potential by the atom core electrons [33, 60]. Unfortunately, due to the low probability of high-angle scattering events, ADF imaging is often impractical for samples which are 1) easily damaged by the electron beam, or 2) contain light elements that have a low probability of scattering electrons to high angles (Section 2.1.6).

Fortunately, there exist several coherent imaging techniques that can exploit a large proportion of the transmitted electrons without averaging over the interference effects, and hence can form images using much lower electron doses than required for incoherent imaging (Section 2.3) [18, 52, 61, 62]. One of the most sensitive imaging approaches is to map the phase shifts of the transmitted electron wave caused by interaction with the sample [63, 64]. However, there exists one major challenge: the phase shifts cannot be directly measured from experimental data. This is known as the *phase problem*, and will be discussed in the following section.

2.2.3 The phase problem

The phase information encoded in a transmitted wave can provide key insights into the local structure of a material. To demonstrate its significance, consider two images of my DPhil project supervisors, Professors Peter Nellist (PDN - Figure 2.3(a)) and Angus Kirkland (AIK - Figure 2.3(b)). By performing a Fourier transform of each

image with respect to the real-space plane, one obtains a complex function which contains both a real amplitude and an imaginary phase. Now let us mix the amplitude of FT(PDN) with the phase of FT(AIK) by taking their product. Following an inverse Fourier transform back to the image plane and plotting the real component of the result, Figure 2.3(c) is obtained: an image very similar to the initial image of AIK (Figure 2.3(b)). Performing the same 'image mixing' using the amplitude of FT(AIK) and the phase of FT(PDN), Figure 2.3(d) is obtained. This suggests that the phase in the Fourier transform of the image encodes a large proportion of the structural information. With this in mind, microscopists and crystallographers have spent decades developing phase-imaging and analysis methods for structure determination [63–65]. However, measuring these phase values is not a trivial task.

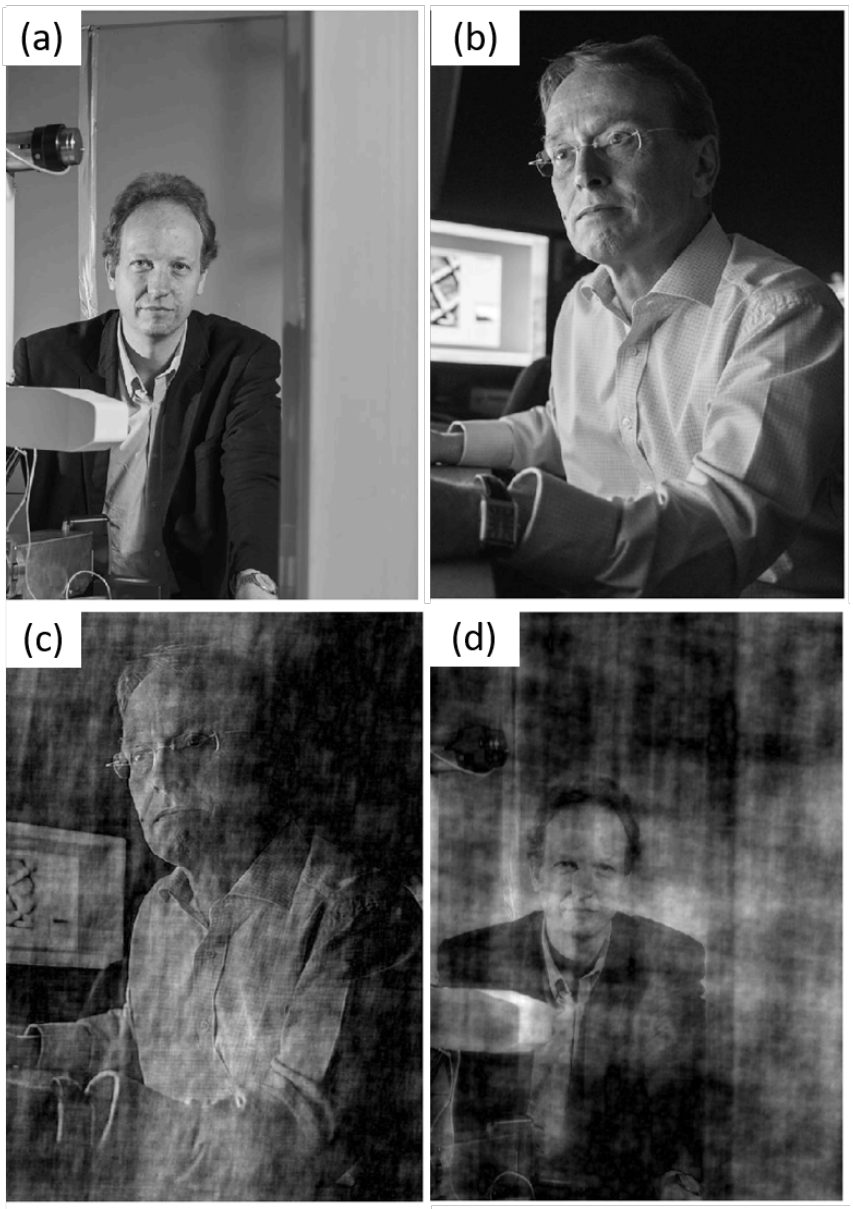

Figure 2.3: (a) Image of PDN (b) Image of AIK. Taking the product of the modulus of FT(PDN) and the phase of FT(AIK), and performing an inverse Fourier transform back to the image plane, sub-figure (c) is obtained. It can be seen that much of the local information is encoded in the phase of the Fourier transform. Applying the same process to the modulus of FT(AIK) and phase of FT(PDN), sub-figure (d) is obtained. *With permission from the University of Oxford Development Office. Photograph credit: John Cairns.*

Consider an experiment where monochromatic radiation is transmitted through a sample and collected in a far-field diffraction plane. Unfortunately, one does not have

direct access to the phase of a wave in a diffraction experiment. Only the intensity (i.e. the square modulus) of a diffraction pattern can be directly recorded on a detector. As a result, the phase information is effectively lost. This problem, known as the *phase problem*, poses a challenge for both X-ray crystallographers and electron microscopists [66, 67]. In the case of optical microscopy, the diffracted waves can be re-interfered in the image plane with the use of high-quality lenses. Experimental configurations can be realised such that the image contrast is directly proportional to the phase of the transmitted waves (*phase-contrast imaging* - Section 2.2.5). However, uncorrected lenses for X-ray and electron optics are much poorer than the lenses used in visible optics[1]. X-ray and electron imaging are widely used characterisation techniques, but the resulting resolutions are typically 2–3 orders of magnitude worse than the diffraction limit of the radiation [64]. Over the last 80 years, several solutions to the phase problem have been proposed and developed for experimental application [64, 66, 67]. In the following subsections, a number of these solutions will be introduced.

2.2.3.1 Beginnings: X-ray crystallography

A solution to the phase problem was first proposed in the field of X-ray crystallography in 1934 by Arthur Lindo Patterson. By acquiring an experimental diffraction intensity and calculating the Fourier transform of its square, Patterson could map the interatomic distances of hexachlorobenzene and potassium dihydrogen phosphate [68]. Since then, a variety of solutions to the phase problem have been implemented for X-ray diffraction experiments, including direct methods [69], multiple isomorphous replacement [70], multiwavelength anomalous dispersion [71] and molecular replacement [72]. These methods have been crucial for the structural determination of biological macromolecules [63], with modern techniques achieving resolutions better

[1] To compensate for the poor performance of electron lenses, additional multipole lenses can be installed in the microscope column to correct for aberrations. These are known as *aberration correctors*, and will be formally introduced in Section 2.2.4.

than 0.4 nm [73]. However, these methods are very often dependent on *a priori* information to infer the phase from calculated diffraction experiments.

In the 1970s and 1980s, a series of iterative algorithms were proposed to solve the phase problem for non-crystalline materials, such as the Gerchberg-Saxton algorithm [74] and the Fienup input-output method [75]. The application of these algorithms to diffraction data gave rise to the development of coherent diffraction imaging, which will now be discussed.

2.2.3.2 Coherent diffraction imaging for non-crystalline materials

First proposed by Sayre in 1952 [76], coherent diffraction imaging (CDI) is the process by which the intensities measured in diffraction experiments can be used to solve the phase of a non-crystalline isolated structure. CDI was first demonstrated experimentally by Miao and co-workers [77] by combining the oversampling method [78] with iterative phase retrieval algorithms [79, 80]. Since then, several variants of CDI have been developed [64], and the techniques have been applied to a variety of radiation sources, such as hard and soft X-ray sources [81,82], electrons [83–85] and free-electron lasers [86, 87]. Most CDI techniques are highly dependent on the constraint that the structure under observation is isolated (i.e. away from the edge of the field of view and not in contact with any other structures). In the case of scanning CDI, more commonly known as ptychography, this constraint is relaxed such that phase retrieval of extended, non-crystalline objects is feasible [12,88,89]. Electron ptychography will be introduced in Section 2.6 and described in further detail throughout this thesis.

In electron microscopy, several imaging and reconstruction techniques have been developed which can overcome the phase problem and reconstruct the phase of the specimen transmission function, such as phase-contrast TEM [90,91], exit-wave recon-

struction [92–94], electron holography [95, 96] and electron ptychography [13, 88, 97]. Before discussing these methods in further detail, the assumptions under which these methods are valid will be introduced.

2.2.4 Phase-objects, contrast transfer functions and aberrations

For a thin sample, the effects of electron wave propagation within the sample can be ignored and it can be assumed that only the phase of the electron wave changes. This approximation is known as the phase-object approximation (POA) [98] and is described by the following equation for the exit-wave:

$$\psi_{exit}(\mathbf{r}) = e^{i\sigma V_p(\mathbf{r})} = 1 + i\sigma V_p(\mathbf{r}) - \frac{\sigma V_p(\mathbf{r})^2}{2} - ... \tag{2.1}$$

where $\psi_{exit}(\mathbf{r})$ is the exit-wave, $V_p(\mathbf{r})$ is the projected potential of the sample, and σ is an interaction constant which relates the phase shift to $V_p(\mathbf{r})$ [28]. Performing a Taylor series expansion of the exponential equation on the right-hand side of Equation (2.1), the scattering can be separated into individual terms, each of which correspond to an order of scattering, i.e. the first term corresponds to the zero-order beam, the second term corresponds to single scattering events, etc. In the case of very thin samples of light atomic elements where the sample-induced phase shift is very small, a weak-phase-object approximation (WPOA) [55] can be used whereby the strength of scattering is diminished such that multiple scattering events can be neglected, i.e. only the interaction between single-scattered and unscattered electron waves is significant. In this case, Equation (2.1) can be simplified to:

$$\psi_{exit}(\mathbf{r}) \approx 1 + i\sigma V_p(\mathbf{r}) \tag{2.2}$$

Equation (2.2) shows that, in this regime, the imaginary component of the exit-wave is linearly proportional to the sample's projected atomic potential $V_p(\mathbf{r})$. Therefore the complex exit-wave should provide linear image contrast and hence quantitative, easily interpretable sample information. However, as discussed in Section 2.2.3, it is the intensity of the electrons that is recorded in the detector plane, not the complex amplitude. Furthermore, the electrons scattered to first order are 90 degrees out of phase with the unscattered electrons after transmission through the sample, as demonstrated schematically in Figure 2.4(a). Thus, for CTEM or STEM imaging with ideal lenses, the scattered electron waves do not manifest as intensity fluctuations in the exit-wave. In other words, the scattering from a phase-object would provide zero contrast in the resulting image.

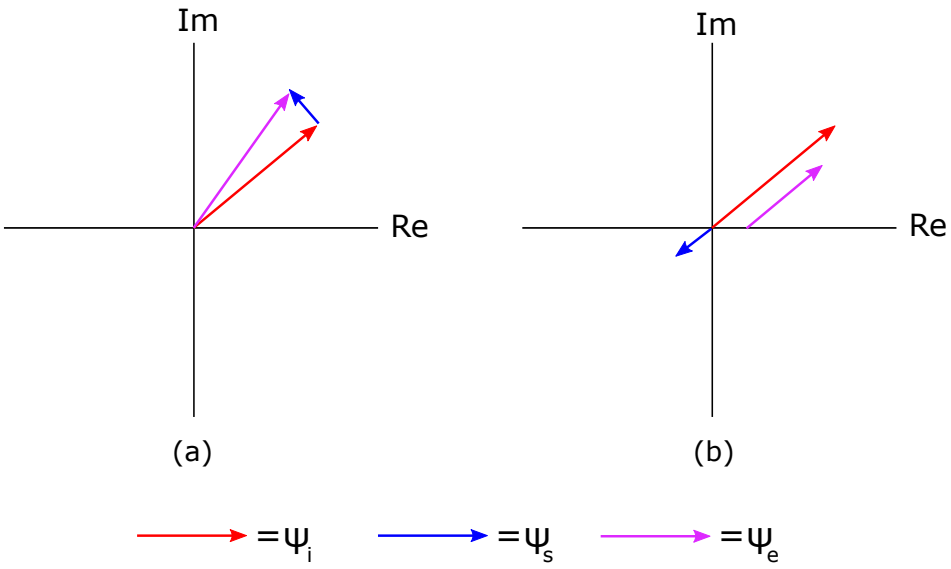

Figure 2.4: Argand diagrams representing the superposition of the incident electron wave, ψ_i, and a scattered electron wave, ψ_s, to generate an exit-wave, ψ_e. (a) When ψ_s is 90 degrees out of phase with ψ_i, the intensity of ψ_e is similar to the intensity of ψ_i. (b) When ψ_s is 180 degrees out of phase with ψ_i, the effects of ψ_s are manifested as intensity variations in ψ_e.

Due to the the effects of imperfect electron optics, or *aberrations*, on image formation, contrast for WPOs is non-zero in CTEM and STEM images [99]. For example, electron optical aberrations can alter the phase differences between unscattered and scattered electron waves such that the sample-induced phase shifts can be manifested as intensity fluctuations in the detector plane. This is shown schematically in Figure 2.4(b). Aberrations are both advantageous and disadvantageous to electron microscopy, in that they can provide contrast for samples that satisfy the WPOA, but ultimately limit the imaging resolution [100]. Traditional, *uncorrected* CTEM and STEM images are dominated by uncorrectable *spherical aberration* caused by the increase of lens focusing strength away from the optic axis [101]. Asymmetric aberrations may also be present in uncorrected instruments, such as axial coma and two-fold astigmatism [93, 102]. The contrast which is transferred to the detector plane is dependent upon these aberrations, and can generally be described by a

phase-contrast transfer function (PCTF) [103]:

$$PCTF(Q) = sin(\chi(Q)) \tag{2.3}$$

where

$$\chi(Q) = \frac{C_{1,0}\lambda Q^2}{2} + \frac{C_{3,0}\lambda^3 Q^4}{4} \tag{2.4}$$

$\chi(Q)$ is the aberration function, Q is the modulus of the spatial frequency (inverse of real-space displacement r), $C_{1,0}$ is the defocus and $C_{3,0}$ is the coefficient of third-order spherical aberration. The effects of asymmetric and higher-order aberrations will influence the PCTF, but are generally much weaker than $C_{3,0}$ for uncorrected instruments [104]. An example PCTF for conventional uncorrected CTEM imaging is shown in Figure 2.5. The coherence of electron sources is limited by their finite spatial extent and energy range (Section 2.2.2.1), and PCTFs should incorporate spatial and temporal *coherence envelopes*, $E_s(Q)$ (SC) and $E_t(Q)$ (TC), to account for this[2] [28].

[2]Note that both spatial and temporal coherence envelopes can only be defined for weak-phase-objects. For stronger phase-objects, transmission cross-coefficients or numerical methods must be considered [105].

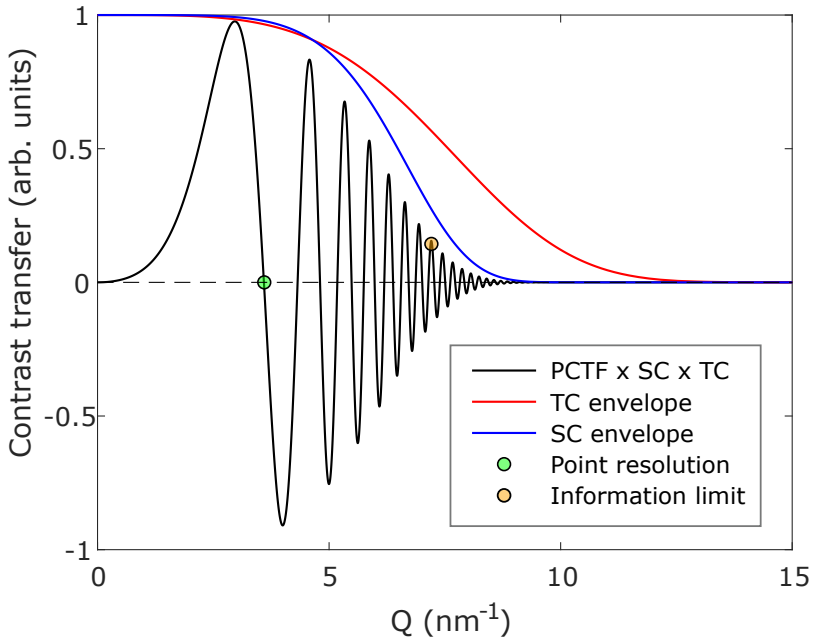

Figure 2.5: Phase-contrast transfer function (PCTF - black) incorporating spatial (SC - blue) and temporal (TC - red) coherence envelope functions at 200 kV with $C_{1,0}$ = 10 nm, $C_{3,0}$= 1.5 mm and a chromatic defocus spread $\delta = 3$ nm. The point resolution and information limit are labelled with green and orange markers respectively.

The PCTF for a given imaging geometry can be experimentally measured by analysing the power spectrum of images of an amorphous specimen [106]. The dark rings in the power spectrum, known as Thon rings, indicate the spatial frequency intercepts of the PCTF. However, in the image plane, the contrast of regions of the specimen can be either positive (e.g. dark atoms) or negative (e.g. bright atoms) with respect to the contrast of the vacuum [28]. This oscillation in the PCTF renders it difficult to obtain a qualitative understanding of a specimen for spatial frequencies past the first intercept, known as the *point resolution* (green marker in Figure 2.5) [103]. Scherzer showed that by using a particular defocus value to mitigate the effect of spherical aberration, the first contrast transfer 'window' could be extended and thus the point resolution optimised [99]. Image interpretation is more complicated for values of spatial frequency past the point resolution, however, useful sample infor-

mation is still present [100]. The spatial and temporal coherence envelopes dampen the contrast transfer to the point where the associated specimen information becomes indistinguishable from experimental recording noise. The limit of spatial frequency at which this occurs is known as the *information limit* (orange marker in Figure 2.5), and has been defined as the point at which the information transfer falls to 13.5% (or e^{-2}) of its maximum value [107, 108]. The point resolution and information limit of a TEM instrument is primarily set by the brightness of electron sources and the quality of electromagnetic lenses in the microscope column. In the latter case, the spherical electromagnetic lenses can only converge electrons down the column. This gives rise to spherical aberration which severely limits the point resolution of the microscope. At the turn of the 21$^{\text{st}}$ century, aberration correctors were developed for TEM instruments using multipole electromagnetic lenses [109–112]. By breaking the axial symmetry down the microscope column, divergent electron lenses could be manufactured in order to compensate for the convergence caused by spherical lenses. The most common aberration corrector configuration is a pair of double-hexapole lenses combined with two pairs of round lenses [111]. The hexapoles are aligned such that their net asymmetric aberrations are minimised, but induce a residual negative $C_{3,0}$ value which compensates for the inherent positive $C_{3,0}$ value of the objective lens [103]. Initial results using $C_{3,0}$-corrected machines saw the improvement of point resolution to 0.12 nm for a 200 kV CTEM and 0.123 nm for a 100 kV STEM [111,112]. With the advent of phase-contrast image reconstruction methods, data can exceed the point resolution and information limit of electron microscopes [13, 88, 113, 114]. The mechanisms of phase-contrast imaging in electron microscopy will now be discussed.

2.2.5 Phase-contrast imaging

Although the advent of hardware aberration correctors, improved electron sources and the improved stability of modern HRTEM and STEM instruments has enabled routine atomic resolution, the nature of the PCTF can still strongly influence the usefulness of sample information visible in a HRTEM or STEM image. For example, crystalline materials with small atomic spacings require high contrast transfer at high spatial frequencies (i.e. 10 nm^{-1}), while the longer range distribution of atoms in amorphous or biological materials is transferred by low spatial frequencies (i.e. 0.1 nm^{-1}) [115]. To image both an amorphous material and a crystalline material with high contrast in the same image requires an imaging method which allows continuous contrast transfer over a wide range of spatial frequencies [115].

From Equation (2.3) it can be seen that for low spatial frequencies, the value of the PCTF is low. Zernike demonstrated that by using a *phase plate* to introduce a relative phase shift of $\pi/2$ radians between scattered and unscattered electrons, the resulting PCTF will be maximum for very low spatial frequencies [90]. This provides an imaging method where contrast is linearly dependent on the sample-induced phase shifts of the electron wave, for a suitably thin sample (i.e. a WPO). Phase plates can be crudely synthesised by deliberate injection of aberrations [99]. However, physical phase plates are increasingly used in electron microscopes for biological applications, and comprise carefully manufactured carbon films which are placed in the back-focal plane of the TEM column [90]. Historically, Zernike phase plates were the most commonly used, consisting of a micron-sized hole for the central unscattered electrons to pass through while introducing a $\pi/2$ phase shift of the scattered electrons [91]. In more recent years, phase plates have been developed which comprise a completely continuous film heated to 200°C to prevent contamination, and make use of a beam-induced Volta potential to improve contrast transfer [116]. These are

known as Volta phase plates, and have played a vital role in improving structural determination in cryo-electron microscopy [117]. However, charging of these phase plates can cause experimental errors and unreliability [118]. Therefore, there has been ongoing development of imaging and reconstruction techniques which do not rely on phase plates for broad contrast transfer, such as electron holography and electron ptychography [13, 96, 97, 119].

2.2.6 Imaging thicker samples

The nature of contrast transfer in TEM varies dramatically as the thickness or atomic number of the sample is increased. If the sample scatters too strongly for the WPOA to be applicable, but is still sufficiently thin that beam propagation within the specimen can be neglected, the POA can be used. If the sample is too thick to obey the POA but is sufficiently thin such that only single scattering events occur, the *kinematical approximation* can be used. In this case, it is assumed that the electrons undergo Bragg reflection only once upon transmission through the sample [120]. The diffraction intensities transferred to the detector plane can be inferred from the intersection of the Ewald sphere with the reciprocal lattice points [121]. X-rays are less likely to scatter more than once for a given sample, hence the kinematical approximation holds for much greater sample thicknesses than for electron microscopy [98]. However, it should be noted that the disadvantages of X-ray microscopy versus HRTEM and STEM are poorer resolution and dose-efficiency. In 1995, Henderson determined that the amount of damage per useful elastic scattering event for X-rays was 'several hundred times greater than for electrons at all wavelengths and energies' [122].

When multiple scattering and propagation effects cannot be neglected, a dynamical theory of diffraction is required [123, 124]. This involves a Bloch wave or multislice

computational analysis to determine the intensity variations of each diffracted beam and the associated image contrast [55]. With strong scattering, phase shifts greater than 2π radians will be induced, resulting in the phase 'resetting' to zero. Some image reconstruction methods are more robust to dynamical effects [125, 126], and will be referred to in subsequent chapters.

2.3 Imaging in the CTEM and STEM

2.3.1 Dark-field CTEM

In conventional CTEM and STEM imaging modes, i.e. BF (S)TEM, the image recorded represents the intensity of the unscattered and scattered electron waves that have passed through the objective aperture and are detected. An alternative CTEM imaging mode is dark-field (DF-) CTEM, whereby the illumination is tilted such that a particular set of diffraction beams is located inside the objective aperture [28]. Applications of DF-CTEM imaging include identifying specific diffraction features in a crystal, such as dislocations and materials phases [127–129].

2.3.2 Bright-field STEM

In the bright-field (BF) STEM configuration, electrons are collected from a central CBED disc using a small BF detector [33]. Using the principle of reciprocity (Section 2.1.4), it can be shown that BF STEM is the STEM-equivalent to HRTEM imaging [37]. However, due to the small detector area, only a small fraction (5–10%) of the transmitted electrons are collected. Hence, to acquire images with reasonable SNRs, the electron dose required (10^7–10^8 e^- nm^{-2}) is typically much greater than that needed for HRTEM imaging [38]. As a result of the superior dose-efficiency,

coherent electron microscopy has historically been performed using HRTEM.

2.3.3 Annular dark-field STEM

Due to the divergent nature of the transmitted electron beam in STEM, electron microscopists began to implement detectors with various geometries to detect electrons scattered within specific angular ranges. Crewe showed the first experimental example of high-resolution imaging in a STEM configuration, using annular dark-field (ADF) imaging [60]. Inserting an annular detector with a large inner radius into the electron column, collection of the coherent component of the electron signal can be avoided. As a result, the detector intensity is dependent on the thickness and atomic number of the specimen [35]. Crewe's incoherent imaging mode, known as high-angle ADF (HAADF) imaging or, more poignantly, *Z-contrast imaging*, imaged individual uranium and thorium atoms, with image contrast related to the atomic number Z and the number of atoms at each probe position [60]. In recent years, HAADF imaging has evolved into a fully quantitative technique commonly used for routine characterisation of heavy nanoparticles [130], with additional applications in areas such as catalysis and semiconductors [25, 131]. One of the disadvantages of HAADF imaging, however, is the poor dose-efficiency: the inner angle for HAADF imaging is approximately three times the radius of the bright-field disc, and as such, only a small proportion of the total signal is collected ($\sim$10%) [33]. The use of ADF detectors with smaller inner radii can increase the proportion of signal used. For example, low-angle ADF (LAADF) imaging uses an inner radius slightly larger than the bright-field disc, and has been applied to imaging light elements [132] and two-dimensional materials [133]. Using this range of inner angles, LAADF imaging is not fully incoherent and is not solely dependent on atomic number. Diffraction contrast contributes to image formation, which has been used to visualise material phases, de-

fects and strain [134]. Medium-angle ADF (MAADF), used to describe ADF imaging with inner angles between HAADF and LAADF, can be used if a specific balance of diffraction contrast and Z-contrast is required for materials interpretation [135].

2.3.4 Annular bright-field STEM

Incoherent imaging in STEM became a powerful and widely used technique throughout the 1970s, but coherent imaging was still advantageous in CTEM. First proposed by Rose in 1974, annular *bright-field* (ABF) STEM uses an annular detector with an inner angle inside the bright-field disc, and an outer angle equal to the probe convergence semi-angle α [38]. As such, the signal collected in ABF imaging is much greater than for HAADF imaging (30-50% vs 10% of transmitted electrons) [33]. ABF imaging has been used to image light element columns amongst heavier elements, such as oxygen in perovskites [136], lithium in cathode materials [137] and hydrogen in VH_2 crystals [138]. ABF STEM was initially proposed as a phase-contrast imaging technique dependent on aberrations for contrast [38,139]. More recent work by Findlay *et al.* proposed ABF as an channelling contrast technique, whereby the positive charge of heavy atomic columns causes a lensing effect which 'channels' the transmitted electrons in specific directions [136]. In practice, both contrast mechanisms contribute to ABF image formation, and as such, the dependence of light-element contrast on defocus, thickness and aberration conditions can complicate image quantification [33,140]. There exist other STEM imaging methods which use simpler contrast mechanisms for image formation, such as (integrated) differential phase-contrast. These methods will now be introduced.

2.3.5 Differential phase-contrast STEM

In the same year that Rose published his initial work on ABF imaging, Dekkers and de Lang introduced the concept of differential phase-contrast (DPC) imaging in STEM [141]. A DPC detector comprises of at least one pair of diametrically opposed segments. Four segments are most commonly used [62] such as shown in Figure 2.6, with other prototypes containing 16 segments [61]. Taking the difference between opposing detector segments for each probe position in a 2D scan provides a map of the potential gradient across the sample. There are several factors which can give rise to these potential gradients, including changes in the electric field, magnetisation, density and thickness of the sample. DPC was demonstrated at atomic resolution by Shibata *et al.* in 2012, in which the mesoscopic and nanoscopic polarisation in $BaTiO_3$ was detected [61]. Furthermore, the technique also been applied to map the electric field of graphene defects [142].

In 2014, Müller *et al.* adopted Waddell's quantum mechanical approach to DPC, whereby using Ehrenfest's theorem, the momentum transfer of the electrons to the sample could be related to the atomic-scale electric fields [143]. This is known as the 'first-moment' or 'centre-of-mass' (CoM) method [144]. As is the case for phase-imaging techniques, *field-imaging* techniques such as DPC and CoM imaging can provide quantitative sample information for phase-objects [144, 145]. In recent years, Lazic *et al.* have demonstrated *integrated* differential phase-contrast (iDPC) imaging, whereby DPC data can be integrated to obtain the transmission function of a thin sample [62, 146].

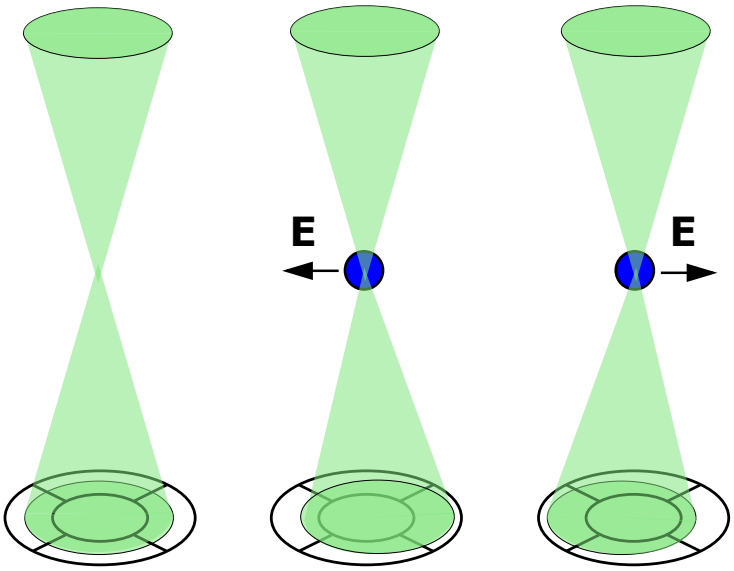

Figure 2.6: Detector configurations for differential phase-contrast (DPC) microscopy. The beam deflection is dependent on the direction of the electric field in the sample. After Chapman *et al.* [147].

Alternatively, an entire two-dimensional CBED pattern (or 'ronchigram' - Section 2.1) can be acquired for each position in a two-dimensional STEM scan, as shown in Figure 2.7, producing a *four-dimensional* data set. This image acquisition mode has been named four-dimensional scanning transmission electron microscopy, or 4D STEM. Although ronchigrams have been recorded for determining aberrations for many decades [34, 148, 149], practical difficulties have limited the acquisition of 4D STEM data sets. These difficulties, and the advances that are being used to overcome them, will now be discussed.

2.4 Evolution of pixellated detectors

Traditional pixellated detectors in the electron microscope have typically comprised charge-coupled devices (CCDs) or complementary metal-oxide semiconductor (CMOS)

devices coupled to a scintillator, and are commonly used in HRTEM imaging. These detectors possess typical operating speeds in the range of 30–60 frames per second (fps) [8]. For a frame rate of 60 fps, a 4D STEM scan of 256×256 CBED patterns would take over 18 minutes to acquire (excluding dead time between probe positions), and would be greatly affected by practical limitations such as scan distortions and stage drift (in the order of nm/minute) [150]. At such speeds, 4D STEM is impractical. In addition, the *signal-to-noise ratio* (SNR) of the data, which is theoretically determined by the level of shot (Poisson) noise for a given intensity on the detector, is further lowered by additional noise introduced by the scintillator and coupling optics [151]. For samples sensitive to electron radiation where low electron dose is necessary, these noise components may obscure any signal present, rendering the data unusable.

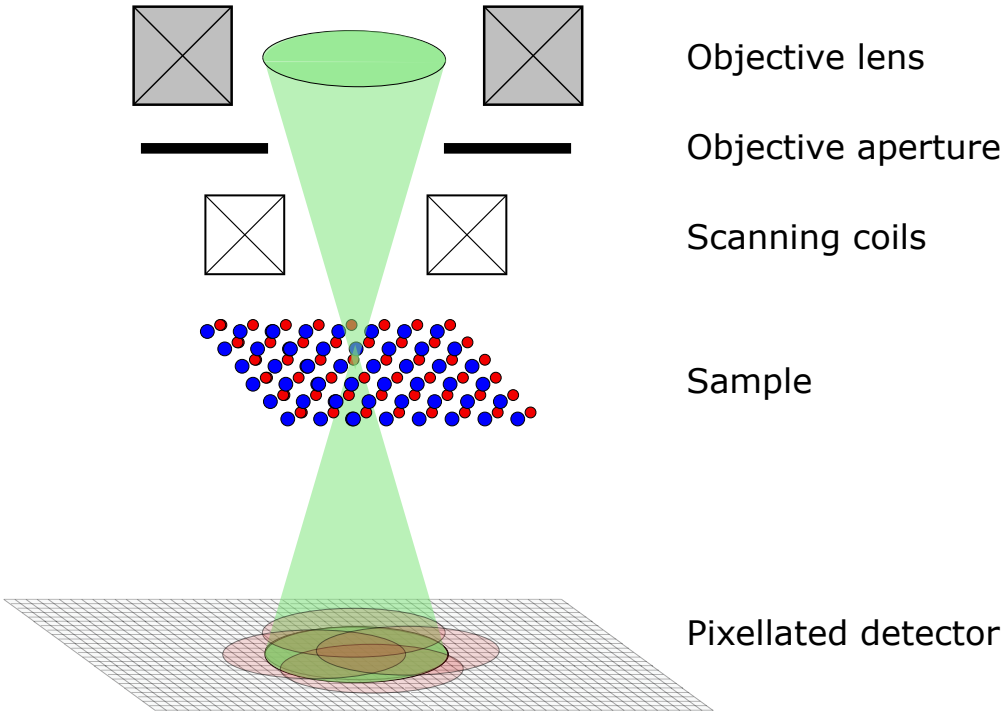

Figure 2.7: Basic schematic for four-dimensional scanning transmission electron microscopy (4D STEM). A 2D convergent beam electron diffraction (CBED) pattern is recorded for each probe position in a 2D raster scan.

In recent years, *direct electron detectors* (DEDs) have been implemented in electron microscopy. Unlike conventional CCD/CMOS devices, DEDs require no scintillators or coupling, such that the detection process adds little or no noise to the acquired data. Detectors which can operate in *counting mode* can count each electron event for a sufficiently low beam exposure and as such, the detection process adds zero readout noise to the data. On the other hand, detectors operating in *integrating mode*, which sum the charge deposited by electrons during a single exposure, add some readout noise due to the finite energy spread of electrons. The reader is referred to Refs. [8] and [152] for a detailed comparison of detection modes.

Two specific technologies have been developed for electron microscopy that improve the signal-to-noise ratio at fast (>1,000 fps) readout speeds: (monolithic) active

pixel sensors ((M)APS) [153–155] and hybrid pixel array detectors (PAD) [156, 157]. As a reference, Table 2.1 contains the specifications for four commercial direct electron detectors available for purchase at the time of writing this thesis.

APS technology typically consists of complementary metal-oxide semiconductor (CMOS) chips below an epitaxial layer [153, 154]. The epitaxial layer generates a large number of low energy electrons which can be read-out, providing single electron sensitivity at frame rates over 1,000 fps [7, 9]. The small pixel sizes and ease of fabrication of large arrays enable MAPS detectors to comprise many pixels on a single chip. For example, the DE-16 camera contains 4096×4096 pixels [9]. Conversely, hybrid APS detectors with thicker active layers such as the JEOL 4DCanvas contain a smaller number (264×264) of larger pixels [7, 158]. Prototype APS systems have achieved frame rates close to 10^5 fps, approaching conventional speeds of ADF STEM imaging [159].

PAD technology consists of an array of photodiodes bump bonded to an application-specific integrated circuit (ASIC). These detectors convert electron counts to a voltage signal, providing single electron sensitivity and high dynamic range at frame rates above 1,000 fps. The pixel width and pixel number varies between manufacturers. For example, the Medipix3 chip on a MerlinEM Direct Electron Detector contains 256×256 pixels[3], each with a pixel width of 55μm [160], while the EMPAD Detector possesses 128×128 pixels, each 150μm wide [11].

The advent of fast DEDs in STEM has led to a universal detector system which can be applied to most pre-existing imaging modes using virtual detector geometries.

[3]It should be noted that the MerlinEM system can also be provided as a Quad detector, i.e. four single chips bonded together [160]. However, for consistency, only the specifications of single-chip detectors have been discussed here.

Name	DE-16	4D Canvas	MerlinEM	EMPAD
Type	MAP(CMOS)	Hybrid APS	Hybrid PAD	Hybrid PAD
Dimensions				
# pixels	4,096×4,096	264×264	256×256	128×128
Pixel width (μm)	6.5	48	55	150
Active area (mm^2)	26.6×26.6	12.7×12.7	14.1×14.1	19.2×19.2
Speed				
Pixel readout speed (MHz)	1,544	70	79	18
Max full-frame rate (fps)	92	1,150	1,200*	1,100
Binning/windowing?	Yes	Yes	No	No
Change bit depth?	No	No	Yes	No
Modified frame rate (fps)	4,237	20,000	14,400	1,100
Dynamic range				
Dynamic range metric	e$^-$/px	e$^-$/px/s	counts/px	counts/px
Max dynamic range	4.0×10^5	1.0×10^3	1.0×10^6	1.7×10^7
References	[9]	[7, 158]	[160]	[11]

Table 2.1: Comparison of specifications for commercial direct electron detectors. *The maximum full-frame rate of 1,200 fps for the MerlinEM system is specified for a 12-bit counting depth.

With new prototype DEDs reaching frame rates of 87,000 fps [159], the acquisition of distortion-free, minimal-drift 4D STEM data sets in the future may only be limited by network speeds. In addition, a wide range of 4D STEM imaging capabilities have been made possible, or more readily achievable, such as crystal orientation and strain mapping [161–163], and atomic-resolution electric field and charge density mapping [164–166]. Furthermore, the combination of 4D STEM acquisition and phase reconstruction algorithms such as electron ptychography has provided high signal-to-noise atomic-resolution reconstructions of light elements [17], single atomic layers [19] and radiation-sensitive materials [18]. The next section will introduce some of these phase reconstruction algorithms, with particular emphasis on focused-probe STEM ptychography.

2.5 Phase reconstruction methods in electron microscopy

Although lenses and phase plates can be used to achieve phase contrast in electron microscopy, the resolution of the data is still limited by the poor quality of circularly-symmetric electron lenses and high cost of aberration correctors (£500k - £1M). A combination of HRTEM and STEM acquisition and post-processing methods have been developed to solve the phase problem and reconstruct the electron wave as it leaves the sample. Three reconstruction methods will be introduced in the following subsections: exit-wave reconstruction, holography and ptychography.

2.5.1 Exit-wave reconstruction

Although the intensity of the electron wave incident on the detector is related to the specimen under illumination, the effects of post-specimen lenses in HRTEM and their associated aberrations cannot be ignored. Throughout the late 1960s and 1970s, Schiske and Hawkes separately proposed methods of 'back-propagating' the detected electron wave through the post-specimen lenses to where it exited the specimen, by compensating for the effects of propagation from the specimen to the detector plane [167, 168]. These methods involved recording a series of images with a varying spatial parameter. In particular, Schiske and Hawkes performed *focal series* exit-wave reconstruction, whereby images taken at sequential values of defocus were collectively processed in order to reconstruct the exit-wave. Recording the electron intensity at a range of defocus values allowed for the compensation of PCTF reversals and the reconstruction of the complex exit-wave [115]. Knowledge of imaging conditions is crucial such that aberrations can be compensated for in post-processing. Once the data is obtained, the exit-wave can be recovered via computational reconstruction methods, such as the Wiener filter [169] or the maximum likelihood method [170]. Exit-wave reconstruction via focal series methods boosted resolution from the point resolution limit (i.e. just under 0.2 nm in the early 1980s) to the information limit set by the spatial and temporal coherence envelope functions (i.e. 0.078 nm in 2001) [171].

An alternative, and arguably more powerful method of series image acquisition is *tilt series* imaging. In a similar fashion to focal series imaging, Kirkland *et al.* recorded a series of images with sequential illumination angles in order to reconstruct high spatial frequency information that could not be obtained from conventional axial imaging [114, 172]. The added value of using a tilt series over a focal series for exit-wave reconstruction was that the effective coherence envelopes could be extended and hence the information limit further increased. Focal- and tilt series imaging methods

have been combined to form tilt-defocus series imaging, the geometry of which is shown in Figure 2.8, which provides super-resolution and enhanced contrast transfer of the exit-wave [102]. Haigh *et al.* demonstrated how adding tilt shifts to a focal series could increase the continuous information transfer of a corrected HRTEM instrument from 0.11 nm to 0.071 nm [93].

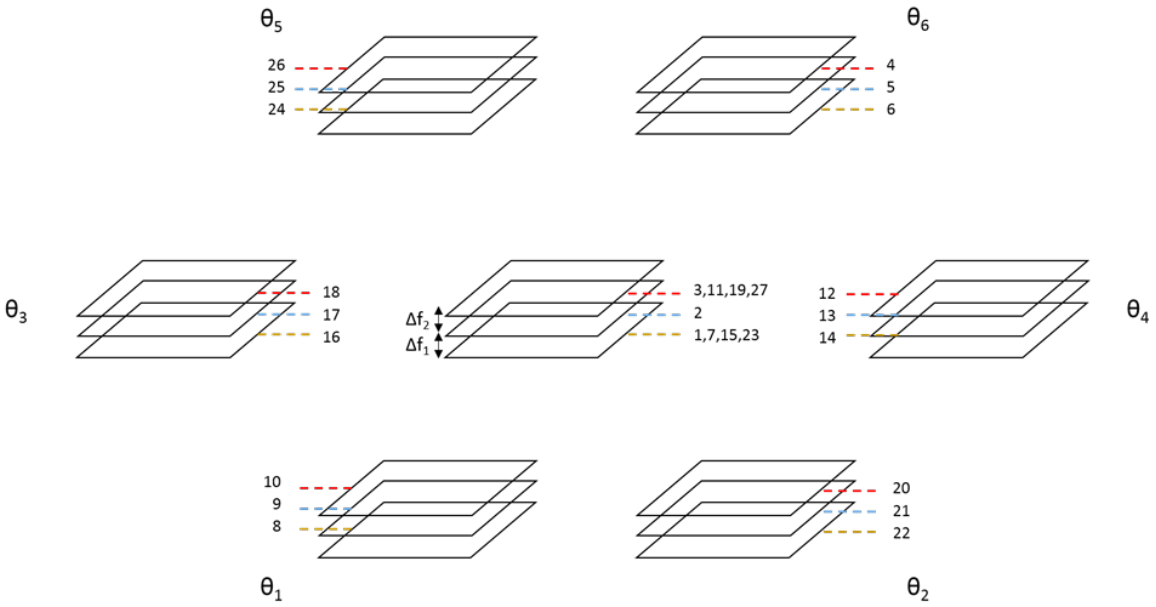

Figure 2.8: Tilt-defocus series experimental setup proposed by Haigh *et al.* [93, 102]. The 27 steps of the series are arranged such that stage- and optical drifts are minimised.

2.5.2 Electron holography

Holography was initially proposed as a potential electron microscopy technique (although demonstrated with light optics) by Dennis Gabor[4] in 1948 [173]. Using the interference between 1) waves which have been scattered by the sample, and 2) a

[4]Gabor was awarded the Nobel Prize in Physics in 1971 for his work on holography.

reference wave of known form, the pattern of fringes resulting from the interference of these two waves, known as a hologram, could be recorded on a photographic film. Upon further illumination of the film, a conjugate pair of exit-waves could be recovered. Holographic experiments were first applied in electron microscopy by Haine and Mulvey in the early 1950s, obtaining nm-resolution exit-wave reconstructions for zinc oxide crystals [174]. Nowadays, electron holograms are recorded by a detector and are 'illuminated' using computational analysis.

The first holographic techniques used in TEM instruments were *in-line* techniques. For in-line holography, a sample is placed in the path of a divergent electron beam before recording a hologram in the detector plane. Thus, the reference and scattered waves lie on the same optic axis [56]. As a result, when the hologram is illuminated, the conjugate pair of exit-waves can be difficult to separate [174]. This complicates the interpretation of sample information. With the development of the electron biprism in 1955 to separate the conjugate exit-waves [175], *off-axis* holography became commonly used in electron microscopy. Both in-line and off-axis methods are implemented in modern holographic experiments. There are a plethora of holographic techniques for electron microscopy, twenty of which have been outlined in a publication by Cowley [176]. Applications of electron holography include nanoscale charge density mapping [177], characterising semiconductor device materials [178, 179] and imaging at atomic resolution [119].

One of the main advantages of electron holography over HRTEM exit-wave reconstruction methods is that holography is inherently energy filtered and as such, the linear (elastic) and nonlinear (inelastic) components can be separated in the reconstruction process [180]. Furthermore, holographic capabilities are not limited by the point resolution of the electron microscope [181]. The nature of the hologram's

interference fringes determine the obtainable resolution: the fringe spacing must be approximately 2–3 times smaller the maximum resolution desired, and there must be sufficient contrast to provide meaningful interference measurements [96]. These constraints require broad angular coherence and stable electron-optical conditions [182]. In the case of off-axis electron holography, the stability of the biprism must also be considered [183]. However, recent experiments in STEM holography have used a phase grating and selected area aperture to carefully separate adjacent diffracted beams and form an interference pattern on a pixellated detector, thus removing the need for a biprism to separate the conjugate exit-waves [184].

2.6 Electron ptychography

In the late 1960s, Walter Hoppe outlined a potential solution to the phase problem as an alternative to holography, known as ptychography [12, 12, 185]. Hoppe proposed that, if one could obtain a diffraction pattern of a sample region such that two diffracted beams would overlap, the interference within the overlap would reveal the relative phase shifts induced by the sample, enabling the reconstruction of both the amplitude and phase of the exit-wave [12]. If a single diffraction intensity measurement is obtained for a centrosymmetric material, the intensity of the separate diffracted beams and their overlap regions are recorded. However, due to the directional ambiguity of the phase of each beam, a range of possible solutions for the complex exit-wave may still exist [65]. By applying a small lateral shift to the sample (or illumination) and recording a second diffraction measurement, the ambiguity would be removed and a unique solution to the complex exit-wave could be determined [12,66]. Although Hoppe *et al.* published several papers on ptychography in the 1960s and 1970s [12,185,186] with specific emphasis on applying ptychography

to electron microscopy, the method was left relatively untouched for over two decades due to experimental limitations (Section 2.4) [187].

2.6.1 Focused-probe ptychography

2.6.1.1 Beginnings

The dawn of experimental ptychography arrived with the application of a number of algorithms used to reconstruct the exit-wave from 4D STEM data. In 1989, Rodenburg highlighted the potential of overcoming the information limit of the microscope using CBED patterns acquired in STEM mode [66].

The first algorithm proposed was the Wigner distribution deconvolution (WDD) method [13,188]. Using a 4D STEM data set acquired as shown in Figure 2.7, a series of Fourier transforms could be performed, before expressing the result as a product of two Wigner distribution functions. The microscope and specimen functions could then be separated via deconvolution. In 1993, a simpler yet powerful reconstructive method: the $\rho'/2$ ('half-rho-dash') method, was introduced by Rodenburg, McCallum and Nellist [189]. Assuming the WPOA, the deconvolution process used in the WDD method could be neglected, and simple integration of the most coherent Fourier components from one *side-band* of interference could be used to directly reconstruct the phase of the complex transmission function. Improved electron sources and hardware aberration correctors enabled the integration of the entire side-bands to be used for phase reconstruction. This is known the single side-band (SSB) method [97], and will be discussed in further detail in Chapter 3.

These developments were significant because of the robustness and simplicity of ptychographic experiments and reconstructions versus electron holography. There

was no requirement to obtain an experimental reference wave: once an experimental data set was acquired, the non-overlapping regions of the diffraction discs in that data set could be used as a reference [66]. Furthermore, it was demonstrated that ptychography could be implemented using a partially coherent electron source, the effects of which could be separated from the ptychographic exit-wave as part of the reconstruction [13]. Finally, once the relative phase of diffracted beams had been calculated, the phase difference between that diffracted beam and a higher resolution diffracted beam could be calculated, providing resolutions beyond the information limit of the microscope [190, 191]. This was first experimentally demonstrated by Nellist *et al.* on a sample of Si<110> [190]. A reconstructed resolution of 0.136 nm was achieved on a VG Microsocopes HB501 STEM: an instrument with a point resolution and information limit of 0.42 nm and 0.33 nm, respectively. The WDD method was subsequently used to achieve super-resolution with X-ray microscopy, where it is still frequently implemented [192, 193]. The SSB and WDD methods are the two most commonly used methods for *focused-probe ptychography* (FPP), which will form the focus of this thesis.

Unfortunately, limitations of instrumentation, computation and detector technology in the 1990s hindered the advancement of electron ptychography. Firstly, the method of improving the resolution beyond the information limit was highly sensitive to dynamical effects for standard (S)TEM instruments [125] – a problem which can now be avoided using modern aberration-corrected instruments [18, 97, 194]. In addition, the TV-rate CCDs used to acquire the CBED patterns were too slow to avoid the effects of stage drift and scan distortions [189, 195, 196]. These slow scan speeds, combined with the sensitivity to dynamical effects, limited the application of ptychography to thin, beam resilient samples such as crystalline silicon, amorphous carbon and gold nanoparticles [189–191]. Furthermore, the large amount of data re-

quired for ptychographic reconstruction placed restrictions on the usable field of view. As a result, further applications of FPP were not seen until these restrictions were lifted by a combination of fast computation and modern detectors (Section 2.4).

2.6.1.2 Advances using direct electron detectors

Combining DEDs (Section 2.4) with post-processing techniques such as ptychography has provided rapid advances in atomic-resolution phase reconstruction. The introduction of noise-free DEDs in combination with hardware aberration correctors and improved instrument stability has led to the rejuvenation of focused-probe, non-iterative ptychography in the last decade [17,18,97,194,197]. Faster, larger memory CPUs and GPUs enable routine data collection and reconstruction for fields of view much greater than that initially achieved by Nellist *et al.* in 1995 [190]. The first demonstration of FPP using DEDs was performed by Yang *et al.* in 2015 [198], where data was collected for a gold nanoparticle, a bulk GaN crystal, and Nd, Ti doped $BiFeO_3$ using a PNDetector with frame rates of up to 4,000 fps. Atomic-resolution reconstructions were obtained for all the above data sets using FPP methods. Subsequently, FPP has been applied to many systems, and will be discussed both at the end of this literature review and in Chapter 8.

2.6.2 Defocused-probe ptychography

Using the phase retrieval algorithms proposed by Gerchberg and Saxton [74] and Fienup [75], Rodenburg and colleagues devised an iterative procedure whereby the object function in a CTEM was initially guessed and subsequently corrected using data obtained from a series of shifted far-field diffraction patterns [88]. This was achieved experimentally in CTEM by shifting the sample with respect to the objective lens aperture, or, more commonly, in STEM by acquiring a raster scan of

CBED patterns. To ensure that consecutive probes of adjacent scan positions overlap, the probe is typically defocused before acquisition [14, 19, 199]. As such, this ptychographic technique will henceforth be referred to as *defocused-probe electron ptychography* (DPP). One of the most common methods of DPP is the extended ptychographic iterative engine (ePIE) [14], which performs iterations to correct for both the electron probe and specimen functions, providing aberration-free exit-wave reconstructions. The ePIE method has also been successfully applied to X-ray [200] and optical [201] microscopy, with applications in both physical and biological sciences [15, 19, 202]. Recently, the efficiency of DPP has been improved by accounting for the modal decomposition of the partially coherent electron probe [203, 204].

It should be noted that FPP and DPP do not need to be non-iterative or iterative respectively, although this is the case for most of the literature. Both SSB and WDD methods are non-iterative methods, using only direct integrals and deconvolution methods. FPP will be the main focus of this manuscript, whereas DPP will be frequently introduced for comparative purposes.

2.6.3 Fourier ptychography

From the principle of reciprocity (Section 2.1.4) [37], it can be shown that each illumination angle in HRTEM images corresponds to a single detector pixel in STEM; and the HRTEM detector plane corresponds to the STEM probe scan [40]. Thus, interference of the superimposed plane waves from tilt series imaging (Section 2.5.1) is equivalent to the diffraction information recorded in the detector plane for an FPP experiment. Tilt series imaging is thus often referred to as a type of *Fourier* ptychography, the first experiments of which were performed by Kirkland *et al.* using uncorrected microscopes on gold nanoparticles and H-Nb_2O_5 [114, 172] (Section

2.5.1). With the introduction of aberration-corrected instruments, tilt series imaging has been applied to produce atomic-resolution reconstructions of crystalline silicon, nanomaterials and α-copper phthalocyanine [93, 115]. As for STEM ptychography, pixellated detectors should increase the capabilities of Fourier electron ptychography, although recent results in this field are currently limited to optical microscopy [89].

2.6.4 Applications

2.6.4.1 High contrast light-element imaging

The introduction of DEDs in STEM instruments has enabled routine light-element imaging using electron ptychography. Pennycook *et al.* showed that multilayer graphene could be visualised using FPP with greater contrast than for ABF, ADF and DPC imaging [97]. Light-element imaging has also been performed using DPP: Wang *et al.* visualised boron atoms in a LaB_6 sample [15].

Ptychography need not replace all other imaging methods: 4D STEM and ADF detector data can be acquired simultaneously, enabling light- and heavy-element imaging from a single scan. This has been demonstrated by Yang *et al.* for an iodine-doped carbon heterostructure: the structure of fullerenes and carbon nanotubes were visualised with ptychography, while the iodine atom locations could be identified using ADF imaging [18].

2.6.4.2 Aberration correction *after* data acquisition

Post-acquisition correction of residual aberrations using FPP was demonstrated by Yang *et al.* using a matrix-inversion method known as singular-value decomposition [18]. Conversely, defocus can be applied to the wave-function to extract a depth-sectioned series from a single ptychographic data set. This has been applied to de-

termine the position of individual carbon nanotubes within a cluster [18, 205], and will be further developed in Chapter 8. Aberration correction is inherent in DPP algorithms such as ePIE, where the probe and specimen transmission functions are determined simultaneously [14]. This capability relieves the experimentalist of fine-tuning the aberrations before data acquisition, reducing beam damage to the sample and increasing experimental throughput.

Overall, ptychography has simplified imaging of previously experimentally challenging samples.

2.6.4.3 Energy materials

Energy materials are challenging to characterise using conventional STEM methods due to their light/heavy-element composition, and air and radiation sensitivity. STEM imaging of lithium was first reported in 2009 by Findlay *et al.* using ABF imaging (Section 2.3) [52, 137]. Careful consideration of electron channeling conditions and wave aberrations can provide atomic-resolution imaging with high contrast for both light and heavy elements [136, 206].

A recent study by Lozano *et al.* demonstrated the application of FPP to lithium cathode materials to study the effects of degradation and battery cycling, and compared this to ABF imaging [17]. By reducing the beam current to below 1 pA, atomic-resolution images of lithium were observed using ptychography, mitigating any structural changes or degradation caused by beam damage. The two main advantages of ptychography over ABF imaging are the ability to correct for aberrations after acquisition, and its extended PCTF window [207]. However, the speed of acquisition of 4D STEM data is still much slower than for ABF data [17]: a problem which will be discussed in further detail in Chapter 7.

Another recent study performed FPP methods in combination with EELS, to identify boron atoms doped at interstitial sites of palladium nanoparticles to modify their catalytic activity [20]. The ptychographic reconstructions confirmed that the interstitial doping was not uniform throughout the crystal lattice, but concentrated in various regions of the nanoparticle.

2.6.4.4 2D materials

HRTEM and STEM imaging have been vital tools for the structural characterisation of two-dimensional materials at the atomic scale. Over the last five years, ptychographic reconstructions have been used to study twisted bilayer graphene [97] and monolayer MoS_2 [19], one-dimensional channels in semiconductors [166] and charge distribution of atoms in hexagonal BN [24]. Using a combination of low electron dose, direct electron detectors and ptychographic methods, the imaging of single-layer beam-sensitive nanomaterials is now routinely achievable [165].

2.6.4.5 Low-dose applications

The high dose-efficiency of electron ptychography shows promise for imaging materials which are sensitive to electron radiation such as zeolites [208], organic-inorganic hybrid perovskites [3] and metal-organic frameworks [209]. Such materials are damaged at electron doses above 10^5 e^- nm^{-2}. To date, there have been few applications of electron ptychography at these low doses. Atomic-resolution ptychography has been performed on MoS_2 at 4×10^4 e^- nm^{-2} [19,199], while macromolecules have been visualised with a dose of 4×10^3 e^- nm^{-2} [210]. Furthermore, a recent cryo-ptychography study has reported reconstructions of viruses using doses below 10^3 e^- nm^{-2} [211].

2.7 Conclusions

In this chapter, the literature relevant to CTEM and STEM has been reviewed. Scattering mechanisms have been discussed, and several common STEM imaging modalities have been outlined. The phase problem, and its solutions, have been introduced, with particular emphasis on focused-probe electron ptychography. The next chapter will describe the mathematical details of STEM ptychography.

Chapter 3

Background theory

In this chapter, the necessary theory used in this thesis will be described, with particular focus on four-dimensional scanning transmission electron microscopy (4D STEM) and focused-probe ptychography (FPP). Firstly, the equations which describe the electron wave travelling from the emission source to the detector plane will be introduced. These equations will be adapted to describe the theory of two FPP methods: single side-band (SSB) and Wigner distribution deconvolution (WDD). To aid the reader's understanding of subsequent experimental results, some of the theory described in this chapter will be further developed throughout this thesis.

3.1 From source to detector

3.1.1 The electron gun

The electron gun consists of a cathode emission source and an anode accelerator system which focuses a beam of electrons along the microscope column. The most important properties of the source for high-resolution imaging applications are 1) brightness, 2) spatial coherence, and 3) temporal coherence.

3.1.1.1 Source brightness

The source brightness, β, is defined as the current density, j_e, per unit solid angle Ω subtended by the source [33, 103]:

$$\beta = \frac{j_e}{\Omega} \tag{3.1}$$

Values for β range from $10^9 A\ m^{-2} sr^{-1}$ for tungsten filament sources to $10^{12} A\ m^{-2} sr^{-1}$ for cold field-emission guns (CFEGs) [56]. Alternatively, a normalised source brightness can be defined by dividing β by the accelerating voltage V_{acc}. The brightness achievable for a given electron source affects the coherent imaging capabilities of the electron microscope. The essential equations which describe source coherence will now be discussed.

3.1.1.2 Spatial coherence

As discussed in Section 2.2.2.1, due to the finite size and energy spread of practical emission sources, electron beams exhibit partial spatial and temporal coherence. The spatial coherence of a source can be determined by measuring the effective source width for coherent illumination, d_c:

$$d_c = \frac{\lambda_e}{2\theta_i} \tag{3.2}$$

where λ_e is the electron wavelength, and θ_i is the semi-angle of the illumination aperture at the source [28]. The effective source width can be decreased significantly by using field-emission sources instead of thermionic sources. For example, CFEGs possess the smallest inherent values for d_c (2 nm), which is three orders of magnitude smaller than that for LaB_6 sources (5–10 μm) [103].

The coherence of STEM imaging is strongly influenced by the brightness of the electron source. If the de-magnified source image incident on the specimen is much smaller than the diffraction-limited probe, it is said to be coherent. However, the de-magnification process significantly reduces the beam current incident on the sample. It was only with the advent of field-emission sources, possessing large β and small d_c values, that sufficient probe currents could be achieved to enable high-resolution STEM imaging [33, 60, 212].

3.1.1.3 Temporal coherence

The temporal coherence of an electron source is often defined in terms of the coherence length[1], λ_c, of electrons emitted from the source:

$$\lambda_c = \frac{\Delta E}{h\nu} \tag{3.3}$$

where ΔE is the energy spread, ν is the electron velocity and h is Planck's constant [28]. For modern aberration-corrected HRTEM/STEM instruments with small CFEG sources, the temporal coherence is the primary resolution-limiting factor, i.e. the temporal coherence envelope is narrower than the spatial coherence envelope (see

[1] c.f. coherence *width* for spatial coherence (Section 3.1.1.2).

Section 2.2.4). The coherence length λ_c can be further increased by decreasing ΔE with the use of a monochromator [213] and is crucial for high-resolution EELS experiments [214]. However, the selection of a narrow energy range of electrons via monochromation significantly reduces the beam current available for HTREM and STEM imaging [103].

3.1.2 The aperture function $A(\mathbf{K})$

On acceleration down the microscope column, the electrons are focused by the condenser lens and objective lens pre-field (Section 2.1) into a small probe at the sample plane. An aperture is usually inserted after the condenser which limits the angular range of electrons incident on the sample and hence reduces the detrimental effects of aberrations (see Figure 2.2). The function describing the electron wave in the aperture plane with respect to the reciprocal-space vector $\mathbf{K}$ is known as the *aperture function*, $A(\mathbf{K})$, where:

$$A(\mathbf{K}) = H(\mathbf{K}) \exp\{i\chi(\mathbf{K})\} \tag{3.4}$$

$A(\mathbf{K})$ is a complex function comprising an amplitude $H(\mathbf{K})$ and phase $\chi(\mathbf{K})$. $H(\mathbf{K})$ is the *aperture shape function* (generally circular) described by:

$$H(\mathbf{K}) = 1, \text{ if } |\mathbf{K}| < K_{max}$$

$$H(\mathbf{K}) = 0, \text{ if } |\mathbf{K}| \geqslant K_{max}$$

where K_{max} represents the largest modulus of $\mathbf{K}$ allowed through the aperture.

The exponential term, $\chi(\mathbf{K})$, in Equation (3.4) describes the *phase surface* of the aperture. For a perfectly coherent source and ideal imaging lenses, the incident phase of the wave would be constant as far as the aperture outer angle α (i.e. the probe

convergence semi-angle). In practice, electron-optical aberrations cause distortions in the phase surface (Section 2.2.4). The aberrations can be described by the wave aberration function, given to third order as

$$\chi(\mathbf{K}) = \sum_{\substack{m\,=\,0,\ n\,=\,0 \\ m+n\,=\,2l-1}}^{\infty} \chi_{m,n}(\mathbf{K}) = \frac{2\pi}{\lambda}\Bigg[\lambda\,(C_{0,1}K^{*}) + \frac{\lambda^{2}}{2}\,(C_{1,0}\,K^{*}\,K + C_{1,2}\,K^{*2}) + \frac{\lambda^{3}}{3}\,(C_{2,1}\,K^{*2}\,K + C_{2,3}\,K^{*3}) + \frac{\lambda^{4}}{4}\,(C_{3,0}\,K^{*2}\,K^{2} + C_{3,2}\,K^{*3}K + C_{3,4}\,K^{*4}) + \ldots\Bigg] \tag{3.5}$$

where m, n and l are non-negative integers, and the Krivanek notation for aberration coefficients has been used [215]. A complex position variable, $K = K_x + iK_y$, has been used to allow for the convenient grouping of terms [216]. The function $\chi(\mathbf{K})$ is a polynomial with an infinite number of terms, each of which corresponds to a particular aberration. In practice, only aberrations up to 3$^{\text{rd}}$ or sometimes 5$^{\text{th}}$ order are usually considered. A list of aberrations up to 3$^{\text{rd}}$ order for aberration-corrected HRTEM and STEM imaging is shown in Table 3.1. In uncorrected HRTEM and STEM instruments, due to the inherently large values of spherical aberration (i.e. $C_{3,0}$ can exceed 1 mm), only the first two radially symmetric terms of Equation (3.5), $C_{1,0}$ and $C_{3,0}$, are considered (see Equation (2.4)). However, for an aberration-corrected instrument (Chapter 2), $C_{3,0}$ can be reduced to less than 0.1% of its original value, and thus the contributions of the other aberrations to $\chi(\mathbf{K})$ become non-negligible. It should be noted that the correction of $C_{3,0}$ may also introduce asymmetric lens aberrations, which must be subsequently corrected for.

Typke	Krivanek	Order in k	Azimuthal symmetry	Name
A_0	$C_{0,1}$	1	1	Image shift
C_0	$C_{1,0}$	2	∞	Defocus
A_1	$C_{1,2}$	2	2	Two-fold astigmatism
B_2	$C_{2,1}$	3	1	Axial coma
A_2	$C_{2,3}$	3	3	Three-fold astigmatism
C_3	$C_{3,0}$	4	∞	Spherical aberration
S_3	$C_{3,2}$	4	2	Star aberration
A_3	$C_{3,4}$	4	4	Four-fold astigmatism

Table 3.1: Aberration coefficients up to 3$^{\text{rd}}$ order for HRTEM and STEM imaging. Adapted from Refs. [102], [215] and [217].

3.1.3 The probe function $P(\mathbf{r})$

The condenser lens system acts to focus the electron beam into a probe in real-space which, for most STEM imaging methods, is focused at, or near, the plane of the sample. The function which describes this probe, known as the *probe function* $P(\mathbf{r})$, can be expressed via an inverse Fourier transform of $A(\mathbf{K})$:

$$P(\mathbf{r}) = \int A(\mathbf{K}) \, \exp\{i2\pi\mathbf{K}\cdot\mathbf{r}\} \, d\mathbf{K} \tag{3.6}$$

where $\mathbf{r}$ is a real-space position vector. One of the main differences between electron microscopy and X-ray or light microscopy is the greater strength of interaction with the sample, caused by the charged particle nature of electrons. The advantage of this is that very thin samples (<5 nm thick) can be imaged with high contrast and at atomic resolution. However, for thicker samples, dynamical diffraction can complicate image interpretation (Section 2.2.6). Thus, for ptychographic experiments, the sample must be thin enough such that the POA, or *multiplicative sample approximation*, can

be used (Equation (2.1)), i.e. it is assumed that only the phase of the wave is changed by transmission through the sample. The wave exiting the specimen, $\psi(\mathbf{r}, \mathbf{R_p})$, can then be described by

$$\psi(\mathbf{r}, \mathbf{R_p}) = P(\mathbf{r} - \mathbf{R_p}) \cdot \phi(\mathbf{r}) \tag{3.7}$$

where $\phi(\mathbf{r})$ is a complex transmission function, $\mathbf{R_p}$ is the probe position vector and $P(\mathbf{r} - \mathbf{R_p})$ represents the probe shifted to $\mathbf{R_p}$.

3.1.4 The detector plane

After transmission through the sample, the intermediate and projector lenses magnify the electron beam and direct it towards a series of detectors. This process can be expressed by performing a Fourier transform of Equation (3.7) with respect to a real-space coordinate $\mathbf{r}$. Applying the Fourier shift and convolution theorems [218], the complex amplitude of the wave in the reciprocal-space detector plane can be expressed as

$$\psi(\mathbf{K_f}, \mathbf{R_p}) = [A(\mathbf{K_f}) \exp\{i2\pi \mathbf{K_f} \cdot \mathbf{R_p}\}] \otimes \Phi(\mathbf{K_f}) \tag{3.8}$$

where $\mathbf{K_f}$ corresponds to the reciprocal-space vector in the detector plane, and $\Phi(\mathbf{K_f})$ is the Fourier transform of $\phi(\mathbf{r})$. For phase reconstruction techniques such as ptychography and HRTEM exit-wave reconstruction, the multiplicative sample approximation is generally assumed [103, 219], and this assumption will be carried forward to other sections unless explicitly stated otherwise.

3.2 2D STEM, 4D STEM and virtual imaging

Once the electrons have been transmitted through the sample at a probe position $\mathbf{R_p}$, the convergent beam electron diffraction (CBED) pattern, or *ronchigram*, can be recorded by one or more detectors. In conventional STEM imaging modes (i.e. 2D STEM) which use integrating bright-field (BF) or annular-dark-field (ADF) detectors, the signal in the CBED pattern is integrated over the entire detector to output a single intensity value. When repeated for all $\mathbf{R_p}$ over a two-dimensional scan, a two-dimensional image is formed, the contrast of which is dependent upon the detector geometry. For BF imaging, a disc-shaped detector is positioned such that only the most coherent signal from the centre of the CBED pattern is recorded [35]. Alternatively, segmented detectors such as DPC detectors can be centred around the bright-field disc to measure sample-induced electromagnetic fields [61, 141, 220].

In the case of four-dimensional STEM (4D STEM), a pixellated detector records the complete two-dimensional CBED pattern at each probe position $\mathbf{R_p}$ in a two-dimensional scan. The complex amplitude of the wave at the detector plane can be denoted $M(\mathbf{K_f}, \mathbf{R_p})$. However, only the intensity of the complex wave can be recorded in the detector plane (Section 2.2.3), and thus $|M(\mathbf{K_f}, \mathbf{R_p})|^2$ is recorded. One of the most straightforward applications of 4D STEM data is *virtual* imaging: conventional STEM detector configurations can be synthesised in post-processing by integrating specific geometric combinations of detector pixels. For example, in the case of a synthetic disc-shaped or annular-shaped detector, the integrated intensity at each probe position $\mathbf{R_p}$ can be described by

$$I_{syn}(\mathbf{R_p}) = \int_{K_{min}}^{K_{max}} |M(\mathbf{K_f}, \mathbf{R_p})|^2 \, d\mathbf{K_f} \tag{3.9}$$

where K_{min} and K_{max} represent the inner and outer collection angles of the synthetic detector. It should be noted that Equation (3.9) can also be applied to hardware integrating detectors of the same geometry, as long as the appropriate detector response function has been included. Alternatively, 4D STEM data can be used to synthesise more complex detector geometries, such as DPC and annular segmented detectors [61, 206].

For the case of electron ptychography, the entire two-dimensional CBED pattern at each probe position is required to reconstruct the complex wave. Assuming a phase-object (POA – Section 2.2.4 and Equation (2.1)), the intensity recorded in the detector plane can be expressed as the squared modulus of Equation (3.8):

$$|M(\mathbf{K_f}, \mathbf{R_p})|^2 = |[A(\mathbf{K_f}) \exp\{i2\pi \mathbf{K_f} \cdot \mathbf{R_p}\}] \otimes \Psi(\mathbf{K_f})|^2 \tag{3.10}$$

where $\Psi(\mathbf{K_f})$ corresponds to the Fourier transform of $\psi(\mathbf{r})$, defined henceforth as the complex transmission function[2]. An example subsection of $|M(\mathbf{K_f}, \mathbf{R_p})|^2$ from an experimental 4D STEM data set obtained from a graphene monolayer is shown in Figure 3.1(a). The ronchigrams in Figure 3.1(a) are noisy - there are no discernible diffracted beams in the CBED patterns. Figure 3.1(b) shows a subsection of the synthetic BF image intensity with respect to probe position $\mathbf{R_p}$, obtained by summing all $\mathbf{K_f}$ values in the BF disc within an outer collection angle of 0.2 α (6.3 mrad). The BF image provides very little structural information about the graphene sample, and is dominated by noise. Conversely, performing ptychography on $|M(\mathbf{K_f}, \mathbf{R_p})|^2$ enables the reconstruction of $\psi(\mathbf{r})$ with a high SNR. The mathematical processes which are used to achieve this will be discussed in the following sections.

[2]To adhere to convention in the literature, the complex transmission function has been defined as $\phi(\mathbf{r})$ in the context of general STEM imaging, and as $\psi(\mathbf{r}, \mathbf{R_p})$ in the context of electron ptychography.

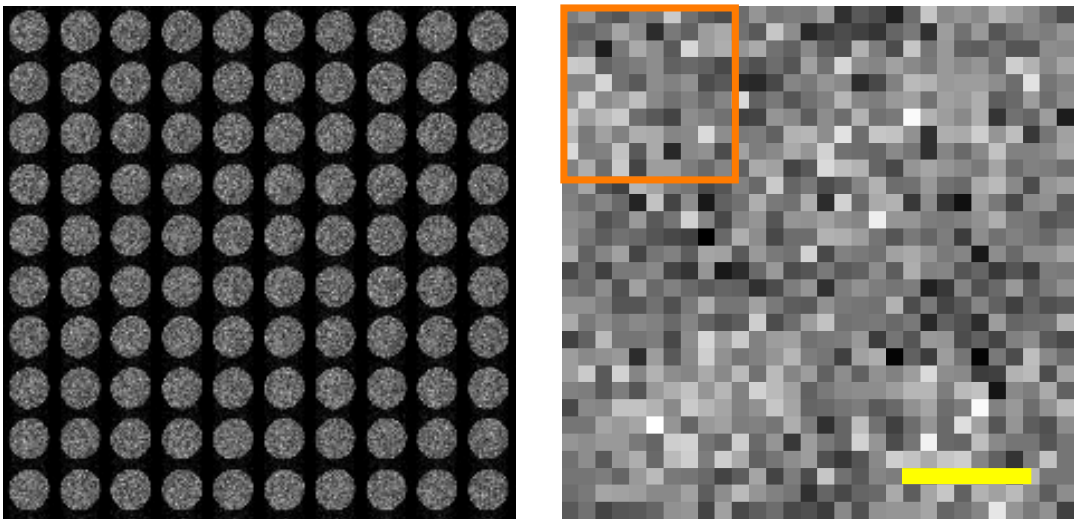

Figure 3.1: (a) Subsection of a 4D STEM data set acquired from a monolayer graphene sample using the JEOL 4DCanvas. (b) Synthetic bright-field image intensity as a function of $\mathbf{R_p}$ obtained by summing all $\mathbf{K_f}$ values within an outer collection angle of 0.2 α (6.3 mrad). The CBED patterns displayed in (a) were used to to synthesise the region in (b) enclosed by the orange square. Scale bar: 0.2 nm.

3.3 Focused-probe ptychography

3.3.1 The phase problem and the Fourier transform

To visualise the phase of the exit-wave in STEM, the complex amplitude of the wave in the detector plane, $M(\mathbf{K_f}, \mathbf{R_p})$, is required. However, as discussed in Section 2.2.3, only the intensity of the CBED patterns, $|M(\mathbf{K_f}, \mathbf{R_p})|^2$, can be recorded on a detector, such that the information about the specimen-induced phase shifts of the electron wave is effectively lost. One solution to unlocking the phase from the acquired 4D STEM data is to perform a Fourier transform of Equation (3.10) with respect to probe position $\mathbf{R_p}$. In order to do this, it is convenient to first evaluate the convolution in Equation (3.10) to obtain:

$$|M(\mathbf{K_f}, \mathbf{R_p})|^2 =$$

$$\iint A(\mathbf{K}')\, A^*(\mathbf{K}'')\, \Psi(\mathbf{K_f} - \mathbf{K}')\, \Psi^*(\mathbf{K_f} - \mathbf{K}'')\, \exp\{i2\pi(\mathbf{K}' - \mathbf{K}'') \cdot \mathbf{R_p}\}\, d\mathbf{K}'\, d\mathbf{K}'' \tag{3.11}$$

where $\mathbf{K}'$ and $\mathbf{K}''$ are dummy variables. Performing the Fourier transform of Equation (3.11) with respect to $\mathbf{R_p}$ gives:

$$G(\mathbf{K_f}, \mathbf{Q_p}) = FT\Big[|M(\mathbf{K_f}, \mathbf{R_p})|^2\Big] =$$

$$\iiint A(\mathbf{K}')\, A^*(\mathbf{K}'')\, \Psi(\mathbf{K_f} - \mathbf{K}')\, \Psi^*(\mathbf{K_f} - \mathbf{K}'')\, \exp\{i2\pi(\mathbf{K}' - \mathbf{K}'' + \mathbf{Q_p}) \cdot \mathbf{R_p}\}\, d\mathbf{K}'\, d\mathbf{K}''\, d\mathbf{R_p} \tag{3.12}$$

This equation can be simplified by firstly evaluating the integral over $\mathbf{R_p}$:

$$\int \exp\{i2\pi(\mathbf{K}' - \mathbf{K}'' + \mathbf{Q_p}) \cdot \mathbf{R_p}\}\, d\mathbf{R_p} = \delta(\mathbf{K}' - \mathbf{K}'' + \mathbf{Q_p}) \tag{3.13}$$

where $\delta(\mathbf{K}' - \mathbf{K}'' + \mathbf{Q_p})$ denotes the Dirac delta function centred at $\mathbf{K}' - \mathbf{K}'' + \mathbf{Q_p}$ [218]. By performing a substitution of variables using $\mathbf{K}''' = \mathbf{K}'' - \mathbf{Q_p}$, Equation (3.12) can be expressed as:

$$G(\mathbf{K_f}, \mathbf{Q_p}) =$$

$$\iint A(\mathbf{K}')\, A^*(\mathbf{K}''' + \mathbf{Q_p})\, \Psi(\mathbf{K_f} - \mathbf{K}')\, \Psi^*(\mathbf{K_f} - \mathbf{K}''' - \mathbf{Q_p})\, \delta(\mathbf{K}' - \mathbf{K}''')\, d\mathbf{K}'\, d\mathbf{K}'''$$

$$= \int A(\mathbf{K}''')\, A^*(\mathbf{K}''' + \mathbf{Q_p})\, \Psi(\mathbf{K_f} - \mathbf{K}''')\, \Psi^*(\mathbf{K_f} - \mathbf{Q_p} - \mathbf{K}''')\, d\mathbf{K}''' \tag{3.14}$$

Finally, the definition of the convolution [218] can be applied to Equation (3.14) to

obtain:

$$G(\mathbf{K_f}, \mathbf{Q_p}) = A(\mathbf{K_f})\, A^*(\mathbf{K_f} + \mathbf{Q_p}) \otimes_{\mathbf{K_f}} \Psi(\mathbf{K_f})\, \Psi^*(\mathbf{K_f} - \mathbf{Q_p}) \tag{3.15}$$

where $G(\mathbf{K_f}, \mathbf{Q_p})$ is the *Fourier overlap function* [97, 189]. The function $G(\mathbf{K_f}, \mathbf{Q_p})$ can be described as a convolution of two functions: one describing the overlap of two aperture functions separated by $\mathbf{Q_p}$; the other corresponding to the product of two Fourier transmission functions separated by $\mathbf{Q_p}$. The significance of the Fourier overlap function is that it is both complex and free of square terms, such that the phase information of the exit-wave is accessible. The nature of $G(\mathbf{K_f}, \mathbf{Q_p})$ can be illustrated by plotting its power spectrum with respect to $\mathbf{K_f}$. This is obtained by summing $|G(\mathbf{K_f}, \mathbf{Q_p})|^2$ over $\mathbf{K_f}$ and plotting as a function of $\mathbf{Q_p}$. Figure 3.2 displays the power spectrum of $G(\mathbf{K_f}, \mathbf{Q_p})$ (PSG) obtained for the same data set used in Figure 3.1. For specific $\mathbf{Q_p}$ values at which the power spectrum value is large, both the amplitude and phase of $G(\mathbf{K_f}, \mathbf{Q_p})$ have been plotted as a function of $\mathbf{K_f}$. Interference is clearly visible in the overlaps between direct and diffracted beams, particularly in the phase of $G(\mathbf{K_f}, \mathbf{Q_p})$. However, as the specimen information is also tied to the electron-optical information via convolution, $\psi(\mathbf{r})$ cannot be determined directly from Equation (3.15). The two most commonly used methods to retrieve $\psi(\mathbf{r})$ from Equation (3.15) are the single side-band method and Wigner distribution deconvolution method, both of which will be described in the following sections.

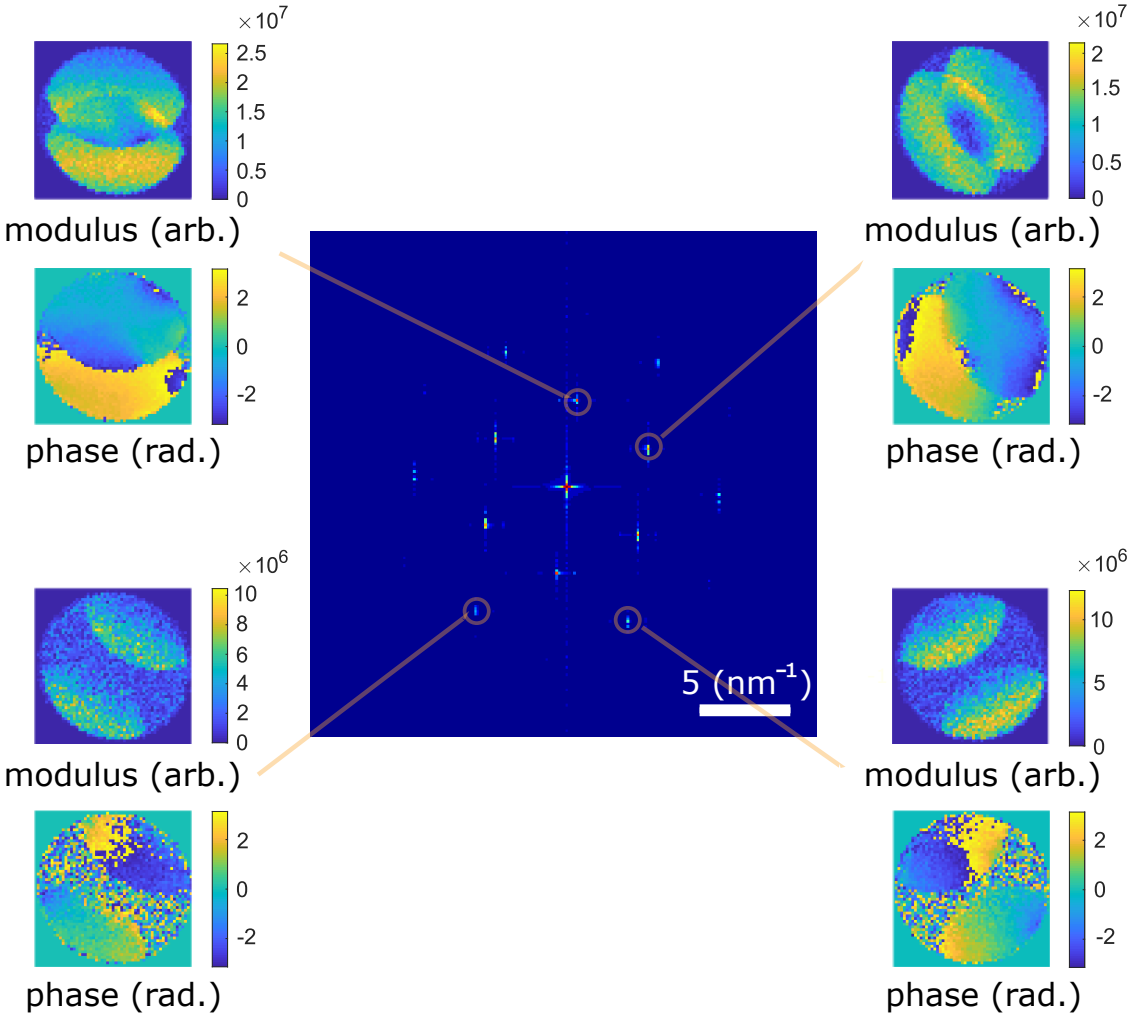

Figure 3.2: Power spectrum of $G(\mathbf{K_f}, \mathbf{Q_p})$ with respect to $\mathbf{K_f}$. For spatial frequencies $\mathbf{Q_p}$ with large power spectrum values, the modulus (arbitrary units) and phase (radians) of $G(\mathbf{K_f}, \mathbf{Q_p})$ have been plotted.

3.3.2 The single side-band method

For the case of a very thin sample where the WPOA can be applied (Section 2.2.5 and Equation (2.2)), Equation (3.15) can be simplified such that the complex transmission function $\psi(\mathbf{r})$ can be directly determined from the Fourier overlap function. Taking the WPOA (Section 2.2.4), the complex transmission function can be expressed as

$$\psi_{wp}(\mathbf{r}) \approx 1 + i\sigma V_p(\mathbf{r}) = 1 + i\psi'(\mathbf{r}) \tag{3.16}$$

where σ is the interaction constant, $V_p(\mathbf{r})$ is the projected potential, and 1 and $\psi'(\mathbf{r})$ represent the direct and scattered components of $\psi_{wp}(\mathbf{r})$, respectively [97]. Applying Equation (3.16) to Equation (3.15), the Fourier overlap function can be simplified for a WPO to:

$$G(\mathbf{K_f}, \mathbf{Q_p}) = |A(\mathbf{K_f})|^2\delta(\mathbf{Q_p}) + A(\mathbf{K_f})A^*(\mathbf{K_f} + \mathbf{Q_p})\Psi'^*(-\mathbf{Q_p}) + A^*(\mathbf{K_f})A(\mathbf{K_f} - \mathbf{Q_p})\Psi'(\mathbf{Q_p}) \tag{3.17}$$

where $G(\mathbf{K_f}, \mathbf{Q_p})$ now comprises a sum of three terms. The first term corresponds to the direct (unscattered) beam, while the other two terms describe the interference between the direct and scattered beams for each value of $\mathbf{Q_p}$. To visualise Equation (3.17), Figure 3.3 shows $G(\mathbf{K_f}, \mathbf{Q_p})$ for two example spatial frequencies, where Q_p is defined as the magnitude of the two-dimensional spatial frequency vector $\mathbf{Q_p}$. As Q_p increases, the distance between the direct and diffracted beams also increases. In the regions where the the direct (0) beam and one diffracted beam interfere (i.e. in a *double overlap* (DO) region), the relative phase difference between the two beams can be determined. For $Q_p < \alpha$ (left of Figure 3.3), there is a region where $-Q_p$, 0 and $+Q_p$ beams overlap (i.e. the *triple overlap* (TO) region) and interfere destructively, providing zero phase information. However, residual aberrations may give rise to nonzero amplitude in the TO region, as is the case for the TO regions shown in Figure 3.2. For $\alpha < Q_p < 2\alpha$ (right of Figure 3.3), the $-Q_p$ and $+Q_p$ beams no longer overlap and the TO region disappears. As Q_p is increased further, the area of the DO regions decreases until the beams completely separate at $Q_p = 2\alpha$. The area of the DO regions influences the contrast with which each sample feature is transferred

to the image plane after ptychographic reconstruction, and this will be discussed in further detail in Chapter 5. In addition, the complex components of the aperture functions (i.e. the aberrations) will affect the phase values determined for the two interference terms in Equation (3.17). Fortunately, the effect of the aberrations can be compensated for using post-processing aberration correction, and will be discussed in Section 3.3.4.

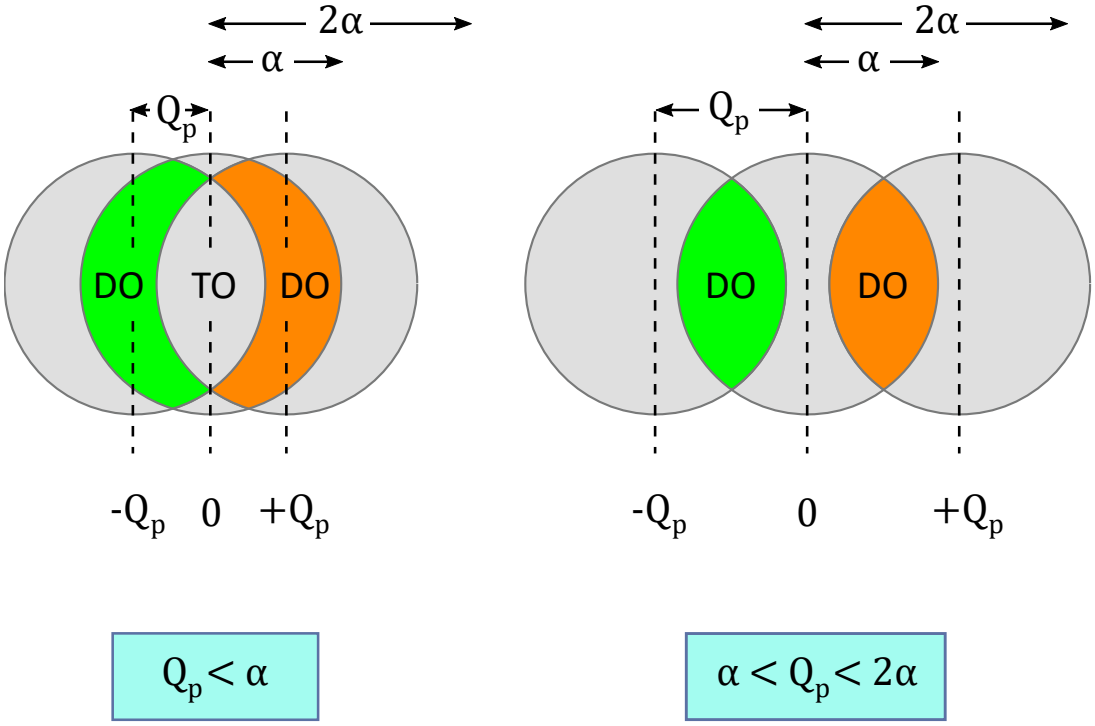

Figure 3.3: Graphical representation of $G(\mathbf{K_f}, \mathbf{Q_p})$ for two example spatial frequencies. The interference of the 0 beam and one of the $\pm Q_p$ beams in the double-overlap (DO) regions provides the phase information used to reconstruct the complex transmission function $\psi(\mathbf{r})$. The overlap of all three beams in the triple-overlap region (TO) provides no phase infromation in the case of a WPO, due to destructive interference.

Retrieving the exit-wave from Equation (3.17) consists of three steps. Firstly, the complex amplitude of either the $-\mathbf{Q_p}$ or $+\mathbf{Q_p}$ DO region in Equation (3.17) (i.e. one *side-band*) is summed over all $\mathbf{K_f}$ for each value of $\mathbf{Q_p}$ to obtain the Fourier trans-

mission function $\Psi'(\mathbf{Q_p})$. Secondly, a 2D inverse Fourier transform is performed to obtain the real-space complex transmission function, $\psi'(\mathbf{R_p})$. Finally, the complex component of $\psi'(\mathbf{R_p})$ can be plotted for each probe position in the STEM scan to produce a real-space, two-dimensional phase reconstruction. Figure 3.4 displays the SSB reconstruction of a graphene monolayer for the CBED subsection used in Figure 3.1. For a very thin sample such as monolayer graphene, there is a negligible change in the amplitude of the electron wave, as seen in Figure 3.4(a). In contrast to the amplitude reconstruction and the BF image in Figure 3.1(b), a hexagonal ring of carbon atoms is clearly visible in the phase reconstruction shown in Figure 3.4(b).

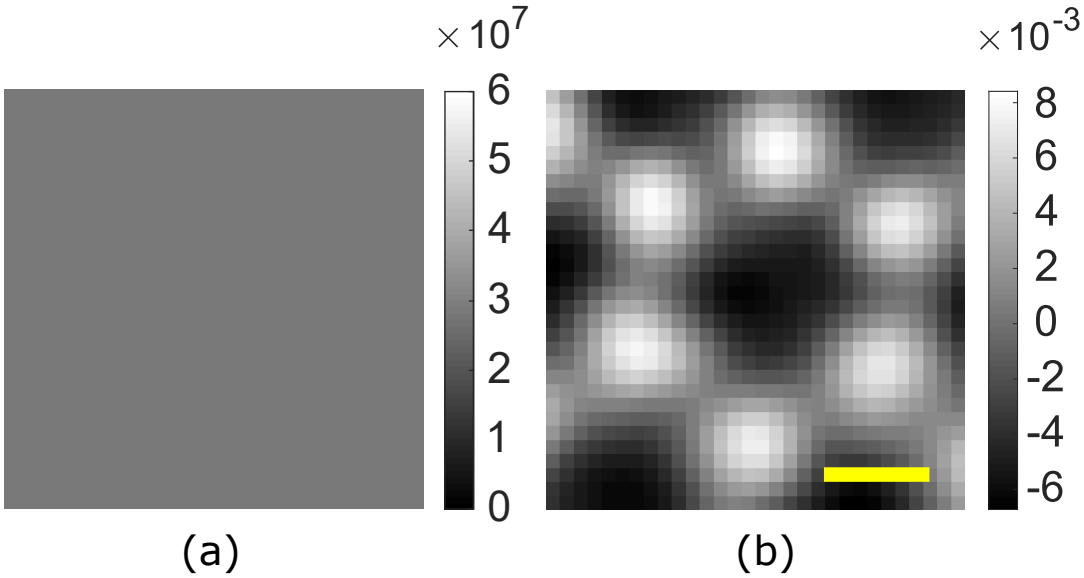

Figure 3.4: (a) Amplitude (arbitrary units) and (b) phase (radians) reconstruction from a graphene monolayer sample using the single side-band method. Scale bar: 0.1 nm.

3.3.3 The Wigner distribution deconvolution

For general phase-objects, the phase of $\psi(\mathbf{r})$ is no longer linearly proportional to the projected potential of the sample, and the convolution in Equation (3.15) cannot be

simplified further. In this case it is necessary to perform a deconvolution to retrieve the specimen information. Following the derivation described by Rodenburg *et al.* [13], the next step after Equation (3.15) is to perform an inverse Fourier transform of $G(\mathbf{K_f}, \mathbf{Q_p})$ with respect to $\mathbf{K_f}$, to obtain:

$$\begin{aligned} H(\mathbf{r}, \mathbf{Q_p}) = \int P^*(\mathbf{m}) P(\mathbf{m}+\mathbf{r}) \exp\left(-i2\pi \mathbf{Q_p} \cdot \mathbf{m}\right) d\mathbf{m} \\ \cdot \int \psi^*(\mathbf{n}) \psi(\mathbf{n}+\mathbf{r}) \exp\left(i2\pi \mathbf{Q_p} \cdot \mathbf{n}\right) d\mathbf{n} \end{aligned} \tag{3.18}$$

where $P^*(\mathbf{m})$ and $P(\mathbf{m}+\mathbf{r})$ represent probe functions with respect to real-space coordinates $\mathbf{m}$, $\mathbf{n}$ and $\mathbf{r}$. This is a convenient step as Equation (3.18) is now expressed as the product of two *Wigner distribution functions* (WDFs), where:

$$\xi_q(\mathbf{a}, \mathbf{b}) = \int q^*(\mathbf{c}) q(\mathbf{a}+\mathbf{c}) \exp\left(i2\pi \mathbf{b} \cdot \mathbf{c}\right) d\mathbf{c} \tag{3.19}$$

such that Equation (3.18) can be rewritten as:

$$H(\mathbf{r}, \mathbf{Q_p}) = \xi_P(\mathbf{r}, -\mathbf{Q_p}) \cdot \xi_\psi(\mathbf{r}, \mathbf{Q_p}) \tag{3.20}$$

where $\xi_a(\mathbf{r}, -\mathbf{Q_p})$ and $\xi_\psi(\mathbf{r}, \mathbf{Q_p})$ represent microscope and specimen WDFs, respectively. The specimen WDF can subsequently be obtained by applying a Wiener deconvolution:

$$\xi_\psi(\mathbf{r}, \mathbf{Q_p}) = \frac{\xi_P^*(\mathbf{r}, -\mathbf{Q_p}) \cdot H(\mathbf{r}, \mathbf{Q_p})}{|\xi_P(\mathbf{r}, -\mathbf{Q_p})|^2 + \varepsilon} \tag{3.21}$$

where ε is a small term used to prevent division-by-zero errors and minimise noise

amplification. Typically, ε is chosen to be a constant equal to small fraction of $|\xi_P(\mathbf{r}, -\mathbf{Q_p})|^2$. Hence it is convenient to define an *epsilon ratio*, ε_r, as:

$$\varepsilon_r = \frac{\varepsilon}{|\xi_P(\mathbf{r}, -\mathbf{Q_p})|^2} \tag{3.22}$$

In the existing literature literature, ε_r values of 0.1 and 0.01 have been used [18, 194], but noisy data sets may require ε_r to be larger, or alternatively, a variable function dependent on the SNR at each value of $\mathbf{r}$ and $\mathbf{Q_p}$ [13]. The effect of ε_r on ptychographic reconstructions will be discussed in further detail in Chapter 6.

Once $\xi_\psi(\mathbf{r}, \mathbf{Q_p})$ has been deconvolved from the probe-related functions, the next step is to extract the ptychographic exit-wave $\psi(\mathbf{r})$. Performing a 2D Fourier transform with respect to $\mathbf{r}$, and applying the definitions of the convolution integral and convolution theorem, one obtains

$$D(\mathbf{K_f}, \mathbf{Q_p}) = \Psi(\mathbf{K_f})\Psi^*(\mathbf{K_f} - \mathbf{Q_p}) \tag{3.23}$$

which is solely expressed in terms of specimen-related functions. Assigning a particular phase as a reference, the Fourier transform of the transmitted wave, $\Psi(\mathbf{Q_p})$, can now be obtained via suitable algebraic manipulation. For example, as illustrated by Rodenburg *et al.* [13], $\Psi(0)$ can be assigned as real and equal to $\sqrt{D(0,0)}$, enabling the solution of $\Psi(\mathbf{Q_p})$ via:

$$\Psi(-\mathbf{Q_p}) = \frac{D^*(0, \mathbf{Q_p})}{\sqrt{D(0,0)}} \tag{3.24}$$

The complex transmitted wave $\psi(\mathbf{R_p})$ can be retrieved via inverse Fourier transform, after which the sample-induced phase shifts can be plotted as a function of probe position. Furthermore, $\Psi(\mathbf{Q_p})$ can be used to assign the phase in the detector plane to scattered CBED discs which do not overlap with the direct beam, in a process known as *stepping out* [13, 190, 191]. As such, super-resolution phase reconstruction is possible via FPP.

3.3.4 Post-processing aberration correction

A unique advantage of electron ptychography over other common STEM imaging techniques is the determination and correction of residual aberrations *after* data acquisition, enabled by the redundancy of 4D STEM data. Applying the WPOA as in Equation (3.17), the phase of $G(\mathbf{K_f}, \mathbf{Q_p})$ for the $-\mathbf{Q_p}$ side-band can be expressed as:

$$\angle G_{-\mathbf{Q_p}}(\mathbf{K_f}, \mathbf{Q_p}) = \chi(\mathbf{K_f}) - \chi(\mathbf{K_f} + \mathbf{Q_p}) - \angle \Psi'(-\mathbf{Q_p}) \tag{3.25}$$

Because the number of *known* measurements of $\angle G(\mathbf{K_f}, \mathbf{Q_p})$ (i.e. 10^4–10^5 pixels within the DO regions) is much larger than the number of *unknown* aberration coefficients up to third order (12), $\chi(\mathbf{K_f})$ can be solved using matrix inversion methods such as singular value decomposition (SVD) [18, 221]. The aberration determination procedure can equally be performed using the $+\mathbf{Q_p}$ side-band, if desired.

Once determined, the aberrations can be used to improve the quality of the ptychographic reconstructions. In SSB ptychography, the determined aberrations are used to synthesise aberration-corrected aperture functions for Equation (3.17). Performing the final steps of the SSB method results in phase reconstructions which are free from the effects of lens aberrations. This approach has been developed as part

of this project work, and will be further described in Chapter 4.

In WDD ptychography, the aberration coefficients can be used to synthesise appropriately aberrated probe functions, and deconvolution of these functions via Equation (3.21) provides aberration-free specimen information which is used to reconstruct the exit-wave. A detailed mathematical description of the aberration determination technique is presented in Appendix B.

3.4 Conclusions

In this chapter, the theory of STEM imaging has been introduced in the context of focused-probe electron ptychography. The key mathematical steps of single side-band (SSB) and Wigner distribution deconvolution (WDD) ptychography were presented. In the next section, the experimental and analytical methods used for the research presented in this thesis will be described.

Chapter 4

Methodology

In this chapter, the experimental and computational workflow for 4D STEM and focused-probe electron ptychography (FPP) will be outlined. Firstly, the microscopes and detectors used throughout this research project will be introduced. Secondly, the experimental procedure for FPP will be outlined. Thirdly, the data processing workflow will be described in detail. Finally, the software and methods for simulation of 4D STEM data will be discussed. The methodology for defocused-probe ptychography (DPP) will not be described here, but DPP will be mentioned throughout this chapter for comparative purposes. Variations in the methods of 4D STEM experiments and ptychographic analysis, which were developed during this research project, will be introduced in the appropriate results chapters.

4.1 Instruments

All 4D STEM experiments were performed on one of two local aberration-corrected electron microscopes installed with a direct electron detector (DED): 1) a JEM ARM200CF with a JEOL 4DCanvas, and 2) a JEM ARM300CF with a MerlinEM system.

4.1.1 JEM ARM200CF

The JEM ARM200CF (Figure 4.1) is based at the David Cockayne Centre for Electron Microscopy (DCCEM) in the Department of Materials, University of Oxford. It is a probe-corrected 80/200 kV (S)TEM instrument with a cold field-emission source and capabilities for incoherent imaging, coherent imaging, EDX and EELS. In 2016, the ARM200CF was installed with a prototype version of the JEOL 4DCanvas pixellated detector system for 4D STEM experiments. This instrument was used for the experiments described in Chapters 5, 6 and 8.

Figure 4.1: The JEM ARM200CF probe-corrected microscope, installed at the DCCEM, Department of Materials, University of Oxford. *Courtesy of JEOL (UK) Ltd.*

4.1.1.1 JEOL 4DCanvas

The JEOL 4DCanvas (Figure 4.2) is an integrating monolithic active pixel sensor (MAPS) direct electron detector that can operate at frame rates of 1,150 fps for full-frame imaging. Recent prototype software upgrades of the 4DCanvas at DCCEM have enabled maximum frame rates of 7,500 fps with binning [222]. Table 4.1 displays the corresponding frame speeds for different imaging modes of the 4DCanvas.

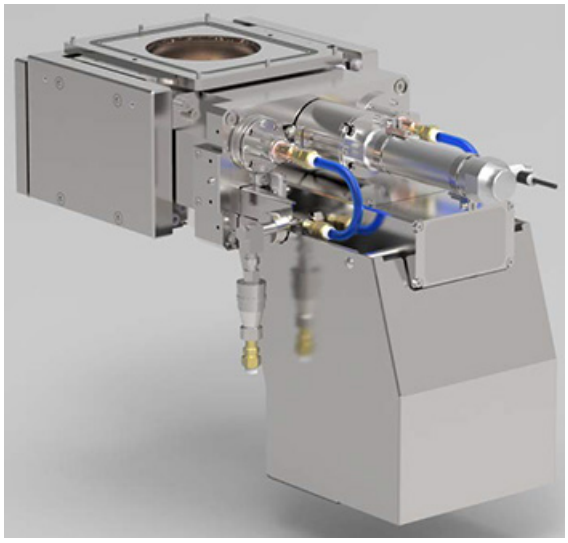

Figure 4.2: The JEOL 4DCanvas, a prototype of which is installed in the ARM200CF at the University of Oxford. *Courtesy of JEOL (UK) Ltd.*

Binning	**Pixels**	**Speed (fps)**	**Fast speed (fps)**
Full-frame	264 × 264	1,150	2,000
2-fold	128 × 264	2,000	4,000
4-fold	66 × 264	4,000	7,513

Table 4.1: Frame speeds of different binning modes for the 4DCanvas system.

4.1.2 JEM ARM300CF

The JEM ARM300CF (Grand ARM) is based at the electron Physical Sciences Imaging Centre (ePSIC) at Diamond Light Source, UK. It is a 30–300 kV double-corrected (S)TEM instrument with a cold FEG source. As well as an EDX detector, it is installed with two cameras: a Gatan OneView camera for HRTEM imaging; and a MerlinEM system for 4D STEM and dynamic TEM imaging. This instrument was used for the experiments described in Chapters 7 and 8.

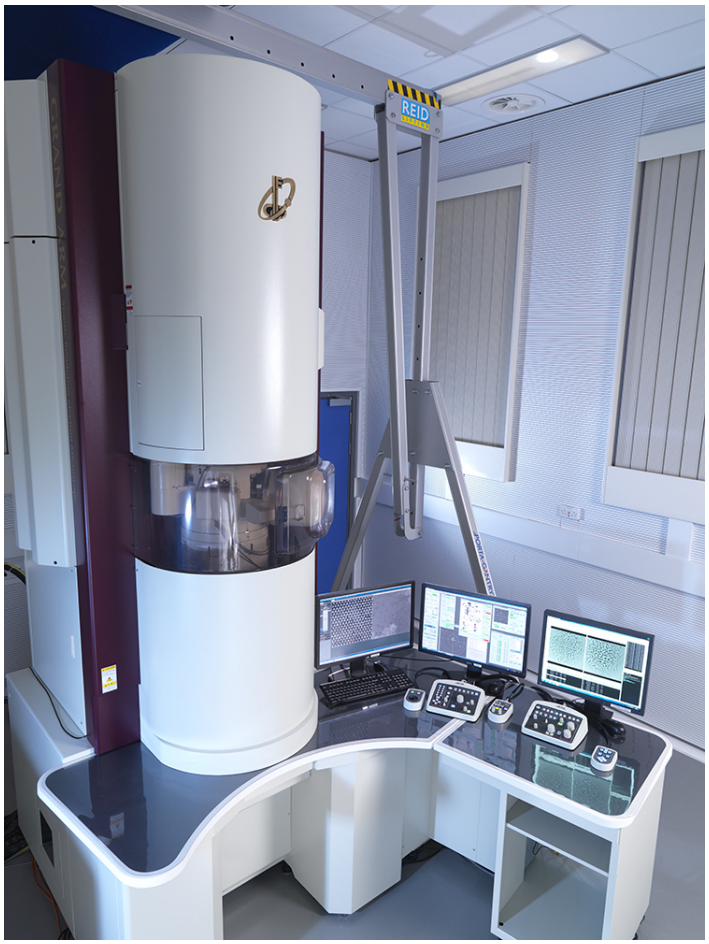

Figure 4.3: The JEM ARM300CF double-corrected microscope, installed at ePSIC, Diamond Light Source, UK. *Courtesy of Diamond Light Source and ePSIC.*

4.1.2.1 MerlinEM system

The MerlinEM system is a hybrid pixel array detector (PAD) consisting of a Medipix3 chip with 256×256 detector pixels operating in a counting mode (Figure 4.4). The maximum frame rate depends on the *counting bit depth* or *dynamic range* (i.e. the range of possible values that can be recorded by a single pixel), the values of which are listed in Table 4.2. The maximum dynamic range is 24-bit (i.e. 2^{24} grayscale levels), and is required for diffraction techniques where both the intense zero-order

diffraction beam and significantly weaker, higher-order diffraction spots are present. Conversely, 4D STEM data sets recorded with a counting depth of 1-bit can be used for phase imaging applications. This will be further discussed in Chapter 7.

Figure 4.4: The Quantum Detectors MerlinEM Camera, a prototype of which is installed in the ARM300CF at ePSIC, Diamond Light Source, UK. *Courtesy of Quantum Detectors Ltd.*

Counting depth	**Max. value**	**Max. speed (fps)**
24-bit	16,777,215	600
12-bit	4,095	1,200
6-bit	63	2,400
1-bit	1	12,500

Table 4.2: 4D STEM speeds using different modes for the MerlinEM system. Source: Ref. [10].

4.2 Experimental procedure

4.2.1 Aberration correction

Before acquiring data on the sample of interest, the microscope aberrations are corrected using a double-hexapole aberration corrector. Firstly, low-order aberrations such as defocus, axial coma and two-fold astigmatism are manually corrected. Secondly, all aberrations are accurately diagnosed using automated software, either by a) acquiring defocused images of the electron probe over a wide range of beam tilt angles on a standard sample (i.e. using the CEOS software correction routines installed on the ARM200CF) [111], or b) by acquiring over-focused and under-focused images of the ronchigram on an amorphous sample (i.e. using the JEOL COSMO software correction routines installed on the ARM300CF) [223]. Finally, the hexapole lens currents are automatically adjusted to minimise the aberrations. Iterative aberration diagnosis and correction is performed until all aberration coefficients up to third order are corrected (see Table 3.1).

4.2.2 4D STEM data acquisition

The DEDs used in this project have been synchronised to the microscopes' STEM scan via the user interface for JEOL (S)TEM instruments (TEM Center). For both the 4DCanvas and MerlinEM systems, the detector settings are controlled using separate software. In the case of the 4DCanvas, only the number of probe positions in a scan is controlled by TEM Center, whereas for the MerlinEM system, TEM Center controls both the dwell time and number of probe positions in a 4D STEM scan.

Once a sample is inserted into the microscope and a suitable region of interest is chosen, a 4D STEM data set can be recorded. This is performed by setting the scan mode in TEM Center to 'Free Mode'. Data can be acquired simultaneously

on both DED and ADF detectors, enabling simultaneous imaging of light and heavy elements. However, to obtain ptychographic data, it is important to consider the sampling requirements for both the electron probe and the pixellated detector. These considerations are now discussed.

4.2.3 Sampling considerations

4.2.3.1 Sampling in real-space

The condition for sufficient sampling (i.e. the Nyquist limit) is defined by the requirement to represent all spatial features within the resolution limit of a system. The maximum spatial frequency, $\mathbf{Q_{pmax}}$, with which the intensity in the detector plane can oscillate is determined by the diameter of the aperture, i.e. $2\alpha/\lambda$. For FPP techniques, the Nyquist sampling rate is dependent on the step size between adjacent probe positions. Using $\alpha = |\mathbf{K}|\lambda$, the maximum spacing between adjacent probe positions required to detect the waveform represented by $\mathbf{Q_{pmax}}$ can be defined as

$$\Delta R_{x/y_{max}} = \frac{\lambda}{4\alpha} \tag{4.1}$$

where $\Delta R_{x/y_{max}}$ is the Nyquist limit for the probe step size in the x/y direction, λ is the electron wavelength and α is the probe convergence semi-angle. For example, for an acceleration voltage V_{acc} = 200 kV (λ = 2.51 pm) and α = 22 mrad, $\Delta R_{x/y_{max}}$ = 0.0285 nm. Undersampled 4D STEM data will give rise to aliasing in the ptychographic phase reconstruction, such that periodic artefacts with lower spatial frequencies will be present. Conversely, oversampled data provides no further improvement in resolution or image quality. Thus, to minimise beam damage to the sample, the probe step size is set to be slightly smaller than $\Delta R_{x/y_{max}}$. It is possible to relax the sampling requirements by lowering V_{acc} (increasing λ) and decreasing α. However, data quality would be reduced as a result of decreased temporal coherence

at lower voltages and poorer resolution for smaller values of α.

4.2.3.2 Sampling requirements in the detector plane

The resolution in the detector plane corresponds to the angular extent of each pixel in reciprocal-space, measured in units of milliradians per pixel. Higher detector resolution can be obtained by using the projector lens system to lengthen the effective distance between the objective image plane and the detector (i.e. the *camera length*). In the case of FPP, the stringent probe sampling required for successful phase reconstruction somewhat relaxes the sampling requirements at the detector plane. Yang *et al.* previously studied the relationship between detector sampling and the peak signal-to-noise ratio (PSNR) of ptychographic reconstructions [207], concluding that there were diminishing gains in PSNR for FPP beyond using 16×16 pixels to sample the bright-field disc. The relaxation of detector sampling requirements also reduces the computer memory needed to obtain ptychographic reconstructions with high SNR, and allows for the acquisition of both ptychographic data and high-angle scattering in a single 4D STEM data set [224].

In contrast to FPP, the probe sampling requirements for defocused-probe ptychography depend on the illumination overlap between adjacent probe positions. In the case of electron ptychography, this overlap ratio has typically been set to 70–75% to optimise ptychographic reconstruction quality [16,199,225], although smaller overlaps have been reported for low-dose applications [199].

Now that the considerations for ptychographic data acquisition have been discussed, the next sections will outline the data handling and processing procedures required to perform ptychography.

4.3 Data management and pre-processing

4.3.1 JEOL 4DCanvas data

The experimental 4D STEM data were transferred from the detector PC onto a desktop PC via Secure File Transfer Protocol (SFTP). Once transferred, the data were converted from raw '.frms6' files to '.mat' files using MATLAB.

4.3.2 MerlinEM data

The 4D STEM data were transferred from the file server at Diamond Light Source to the desktop PC for processing. In most cases, the processed data sets were converted from raw full-frame (256×256 detector pixels) '.mib' files to binned (64×64 detector pixels) '.hdf5' files.

4.4 Data processing

The majority of the data processing used for the work in this thesis was performed using in-house reconstruction codes written in MATLAB. Most of these codes are now open source in the PtychoSTEM repository [226], and in addition, have been integrated into the py4DSTEM software package [227]. In this section, the workflow of PtychoSTEM, an overview of which is shown in Figure 4.5, will be discussed.

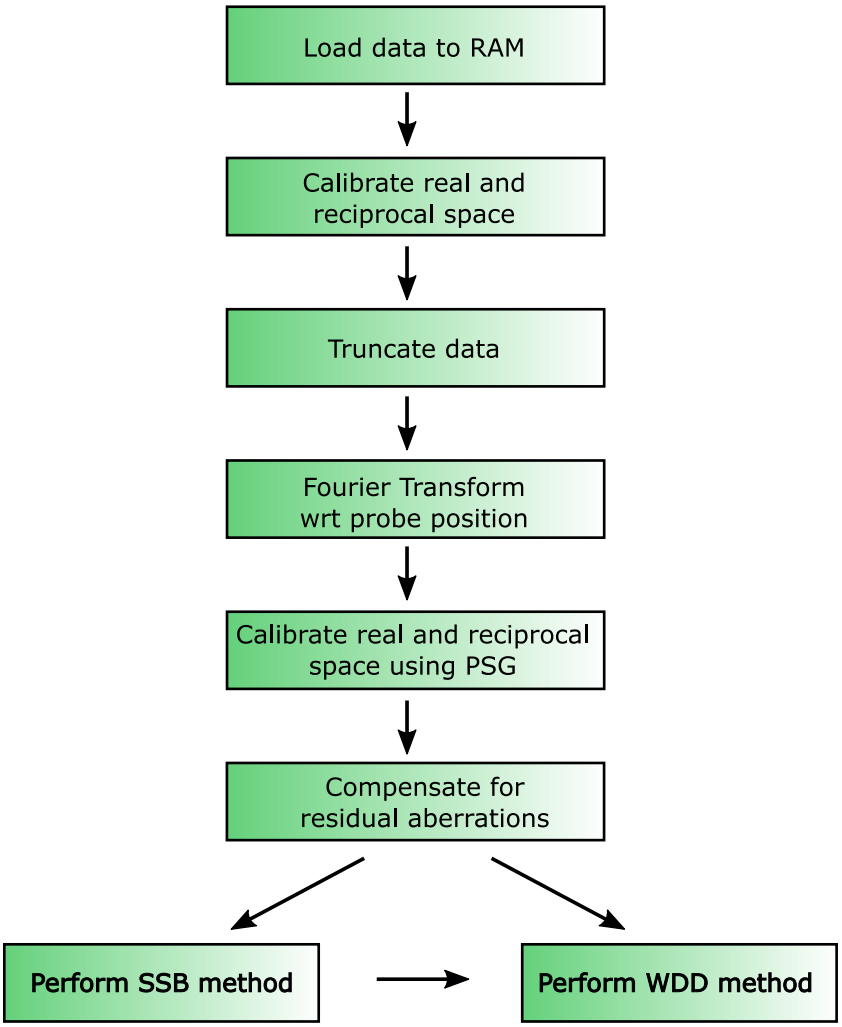

Figure 4.5: Workflow of ptychoSTEM code.

4.4.1 Loading parameters and data

The first step of the ptychographic processing workflow is to create a parameter file containing the input variables required to perform the reconstruction. Example parameters can be found in Table 4.3. The 'dataformat' parameter determines the file format which is to be loaded into MATLAB. Due to the size of 4D data sets (typically ~30 GB for 256×256 full-frame CBED patterns), the detector plane may be further binned or cropped before loading. For the case of data acquired on the

JEOL 4DCanvas with four-fold hardware binning (66×264 pixels), the data is further binned by a factor of four during post-processing to reduce the detector plane to 66×66 pixels. Once loaded and structured into a 4D array in MATLAB, the data is ready for processing. An example subsection of a 4D data set acquired from a monolayer graphene sample is shown in Figure 3.1(a). As previously discussed in Section 3.2, applying a synthetic BF detector to these noisy CBED patterns produces a low SNR image as shown in Figure 3.1(b). Conversely, performing ptychography on such data gives a high-SNR atomic-resolution phase reconstruction as shown in Figure 3.4.

Parameter	**Details**	**Typical values (units)**
voltage_kV	Accelerating voltage	80 – 200 (kV)
ObjApt_angle	Convergence semi-angle	5 – 30 (mrad)
dataformat	Data file format	'HDF5', 'TIF'
use_padding	Pad the edges of the 4D array	0 or 1
rot_angle	Rotation between sample and detector	$-\pi/2$ – $\pi/2(rad)$

Table 4.3: Example input parameters used in the PtychoSTEM reconstruction code.

4.4.2 Calibrating sample and detector planes

The probe step size, $\Delta\mathbf{R_p}$, wavelength of incident electrons, λ, and probe convergence semi-angle, α, can be used to calibrate the sample plane ('real-space') and detector plane ('reciprocal-space'). If the magnification of the microscope has been calibrated, the real-space plane of the 4D STEM data can be scaled to the probe step size. The reciprocal-space plane can be calibrated by noting that the radius of the BF disc should be equal to α/λ. For convenience, the reciprocal-space detector plane is expressed in units of angle (mrad) throughout this thesis, where $\alpha_f = |\mathbf{K_f}|\lambda$.

4.4.3 Virtual image reconstruction

Once both real-space and reciprocal-space have been calibrated, a variety of masks can be applied to the detector plane to generate synthetic images. For example, in the case of synthetic central BF imaging, a binary mask which is nonzero for $|\mathbf{K_f}| < 0.2\ \alpha$ is applied to each CBED frame. The masked signal is summed for each frame in the data set, forming a 2D synthetic BF image. The same principle of synthetic imaging can be applied to ABF, ADF and DPC imaging.

4.4.4 Data truncation

One of the novel capabilities of electron ptychography over other STEM imaging and reconstruction methods is in providing resolution beyond the information limit of the electron microscope, as already described in Refs. [19, 191, 225]. However, the information limit of modern aberration-corrected microscopes now exceeds 0.1 nm and as such, atomic-resolution ptychography is commonly performed using only the pixels within the bright-field disc [18, 97, 194, 197]. For the work in this thesis, the data was therefore truncated to include only the bright-field disc, reducing the RAM and computing time required for reconstruction.

4.4.5 Fourier transform of $|M(\mathbf{K_f}, \mathbf{R_p})|^2$

The Fourier transform of the truncated data is taken with respect to probe position $\mathbf{R_p}$ to obtain $G(\mathbf{K_f}, \mathbf{Q_p})$, as described in Section 3.3.1. Once obtained, $G(\mathbf{K_f}, \mathbf{Q_p})$ can be used for further calibration of real-space and reciprocal-space.

4.4.6 Further calibration using power spectra of $G(\mathbf{K_f}, \mathbf{Q_p})$

The power spectrum of $G(\mathbf{K_f}, \mathbf{Q_p})$ (PSG) serves as a useful tool to assess the 4D STEM data quality and accuracy of the input parameters *before* performing the

ptychographic reconstruction. The PSG can be obtained by plotting the sum of $|G(\mathbf{K_f}, \mathbf{Q_p})|^2$ over all $\mathbf{K_f}$ values as a function of spatial frequency $\mathbf{Q_p}$. An example PSG for a graphene data set is shown in Figure 3.2. By determining the local intensity maxima within the PSG, one can identify the values of $\mathbf{Q_p}$ at which $G(\mathbf{K_f}, \mathbf{Q_p})$ has a high SNR. Once identified, $G(\mathbf{K_f}, \mathbf{Q_p})$ of the strongest $\mathbf{Q_p}$ values, as shown in the periphery of Figure 3.2, can be analysed to check the calibration of real- and reciprocal-space. This process will be described below.

For SSB ptychography, a mask must be applied to $G(\mathbf{K_f}, \mathbf{Q_p})$ which, if the real- and reciprocal-space have been calibrated correctly, should mask all but the DO regions at each $\mathbf{Q_p}$ value. Assessment of this mask alignment can also be used to determine the accuracy of the input parameters. To demonstrate this, examples of aligned and offset masks and their effect on the resulting ptychographic phase reconstructions are shown in Figures 4.6 and 4.7, respectively. If the rotation angle assumed in the reconstruction does not match the true value θ_{rot}, the mask will be mis-tilted such that the phase of separate DO regions will be summed together prior to the final reconstruction step. In the case of a 90° mis-tilt, the $+\mathbf{Q_p}$ and $-\mathbf{Q_p}$ components interfere destructively such that no phase information is transferred to the image plane.

If the assumed probe spacing in the reconstruction is smaller than the true probe spacing $\Delta\mathbf{R_p}$, the overlapping circles that define the mask will be spaced too closely together, such that only part of the DO region will be used in the ptychographic phase reconstruction. If the assumed probe spacing is larger than $\Delta\mathbf{R_p}$, additional noise will contribute to the phase reconstruction. Once any inaccuracies have been diagnosed, the correct values for θ_{rot} and $\Delta\mathbf{R_p}$ can be input to the reconstruction and the real- and reciprocal-spaces can be re-calibrated. If the mask fits directly over the DO regions as highlighted in red in Figures 4.6 and 4.7, both real-space and

reciprocal-space are correctly calibrated. In addition to calibration testing, the phase of $G(\mathbf{K_f}, \mathbf{Q_p})$ can be used to determine residual lens aberrations present in the data. This procedure is described in the following section.

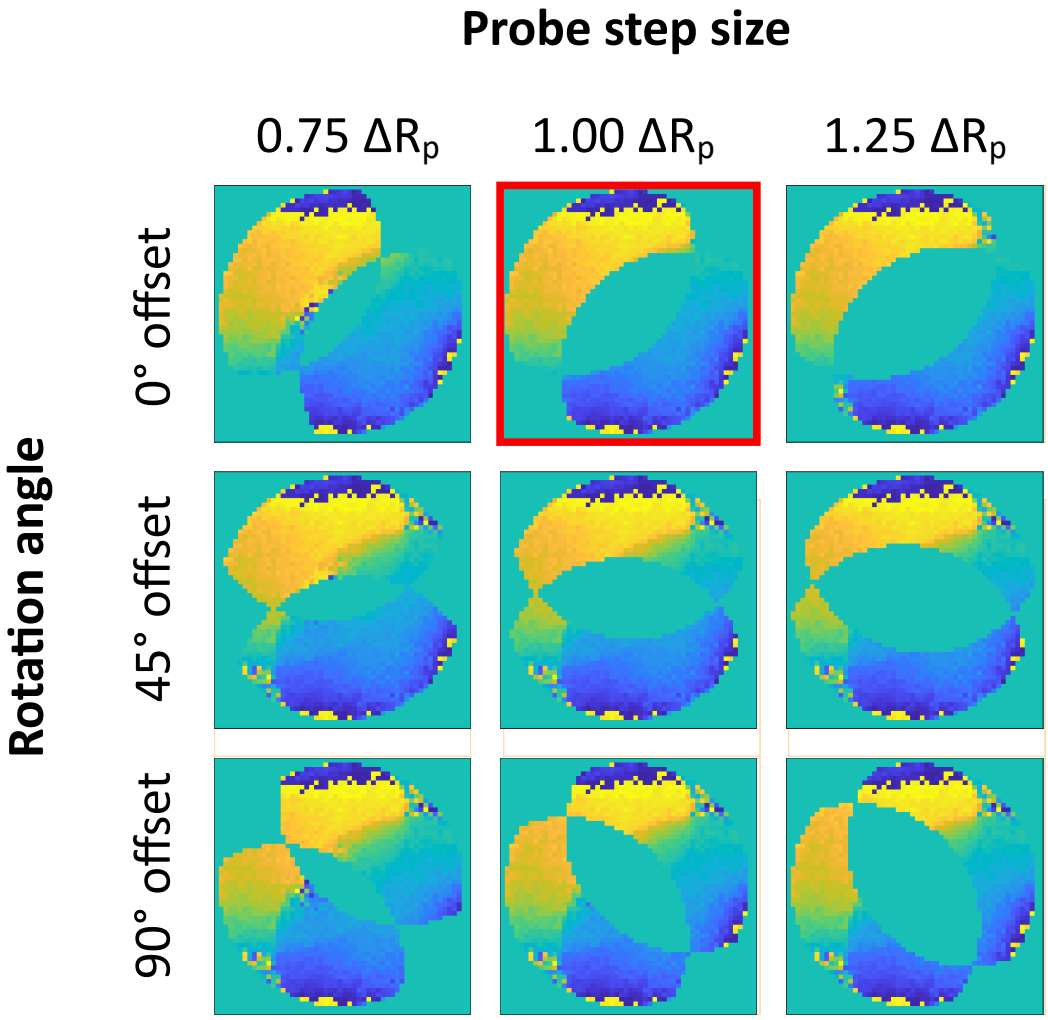

Figure 4.6: Masks applied to the phase of $G(\mathbf{K_f}, \mathbf{Q_p})$ for various values of input probe step size and rotation angle. The mask synthesised from the true values of probe step size, $\Delta\mathbf{R_p}$, and rotation angle, θ_{rot}, is highlighted in red.

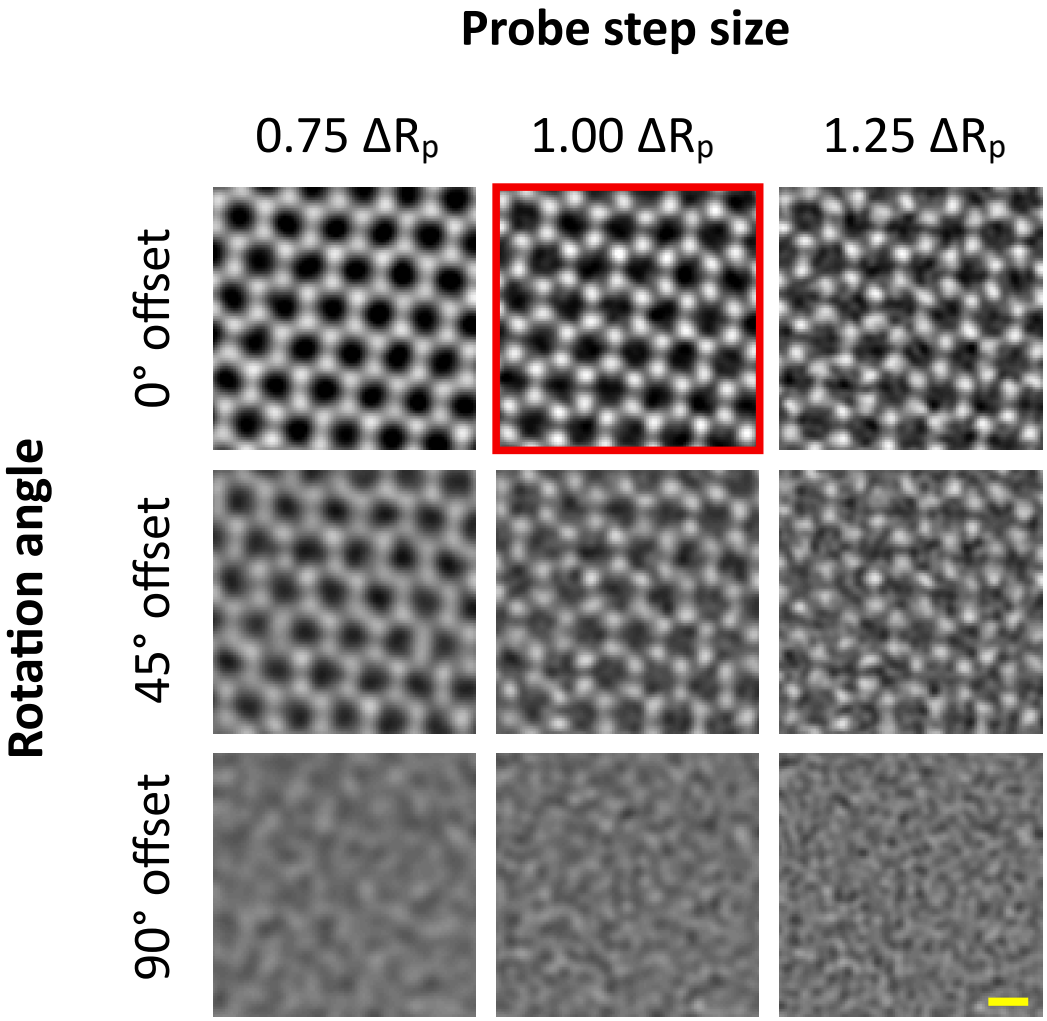

Figure 4.7: SSB phase reconstructions using the masks applied in Figure 4.6. The phase values have been scaled to the reconstruction which uses the correct parameters, highlighted in red. Scale bar: 0.2 nm.

4.4.7 Post-processing aberration correction

As discussed in Section 3.3.4 and by Yang *et al.* [18], under the WPOA, residual lens aberrations can be diagnosed and compensated as part of the SSB and WDD reconstruction processes. Firstly, calibration of real- and reciprocal-space is performed as discussed in Section 4.4.6. Secondly, SVD matrix inversion is performed as described in Appendix B in order to obtain $\chi(\mathbf{K_f})$ from $\angle G(\mathbf{K_f}, \mathbf{Q_p})$ (Section 3.3.4). For the experiments discussed in this thesis, an iterative aberration determination method was used which allowed convergence to a solution for $\chi(\mathbf{K_f})$ at low electron dose. Full details of the iterative procedure can be found in Appendix B.

4.4.8 Single side-band reconstruction

Assuming a WPO and zero aberrations, a mask is applied to $G(\mathbf{K_f}, \mathbf{Q_p})$ at each value of $\mathbf{Q_p}$, such that only the interference terms of Equation (3.17) are non-zero (see the red DO regions in Figure 4.6). Next, each DO region in $G(\mathbf{K_f}, \mathbf{Q_p})$ is multiplied by a synthetic aperture function using the aberration coefficients determined from SVD matrix inversion. One of the DO regions (side-bands) is summed at each value of $\mathbf{Q_p}$, before performing an inverse Fourier transform to reconstruct $\psi(\mathbf{R_p})$. The SSB phase reconstruction can then be plotted as shown in Figure 3.4.

4.4.9 Wigner distribution deconvolution reconstruction

The WDD method is applied as described in Section 3.3.3. For aberration correction, the probe function $P(\mathbf{r})$ must be synthesised using the aberrations determined from SVD matrix inversion. Following deconvolution and reconstruction, the specimen transmission function $\psi(\mathbf{R_p})$ will be free from the effects of lens aberrations.

4.5 Simulation of 4D STEM data

In order to test the validity of a ptychography experiment before performing it, it is useful to reconstruct simulated data under various imaging conditions. For this project, 4D STEM data sets were simulated using the multislice method in MULTEM electron microscopy simulation package [228]. The multislice method is a numerical method by which the propagation of an electron beam through a sample is approximated by a set of thin slices, each of which obey the WPOA, to calculate the wave at the exit surface [55]. There were two steps to the simulation workflow: 1) the simulation of structure factors for an input specimen structure file, and 2) the simulation of the imaging process for a focused-probe 4D STEM experiment. To model an experimental ptychographic reconstruction using a particular electron dose, Poisson noise was applied to each simulated CBED frame prior to reconstruction.

4.6 Multi-frame acquisition and data registration

In some circumstances, such as those presented in Section 8.1, a single 4D STEM data set is insufficient to obtain high-SNR phase reconstructions using electron ptychography. In this case, sequential 4D STEM frames can be acquired from a single region of the sample, from which a summed-average can be obtained to increase the SNR of the data. However, before summing the data series, the relative shifts induced by stage drift and scan distortions must be corrected for. This is performed by importing the data into Digital Micrograph and using the SmartAlign plugin to align the data sets [150]. The output of the SmartAlign procedure is a summed-average, or *multi-frame average*, of the data series. Further details of multi-frame acquisition and data registration are described in Section 8.1 and also in the existing literature [150].

4.7 Conclusions

In this chapter, the experimental and computational ptychographic techniques used during this research project were presented. The effects of several experimental settings were explored, including probe sampling and camera length. In addition, it was demonstrated that certain parameters could be tuned to optimise the quality of the ptychographic reconstruction. Now that the background literature, theory and methodology have been discussed in detail, the following chapters will present the new science and results that have been achieved during the course of this research project.

Chapter 5

Experimental contrast transfer in electron ptychography

The author is grateful to Dr Martin Humphry for providing the ePIE phase reconstructions used in this chapter.

In this chapter, the unique contrast transfer properties of electron ptychography are explored in order to define the optimum conditions for a ptychographic experiment. Firstly, the background equations which describe the PCTF of SSB ptychography are introduced, demonstrating the advantage of ptychographic PCTFs versus common phase-contrast HRTEM and STEM imaging techniques. Following this, experimental studies of contrast transfer are presented for both amorphous and crystalline materials to demonstrate the physical interpretation of contrast transfer for electron ptychography. Finally, the contrast transfer functions for SSB and ePIE methods are compared using simulations and experimental data.

5.1 Introduction

The application of TEM imaging to challenging materials is dependent on imaging modes which can provide high contrast at low electron dose. Over the last half-century, a plethora of imaging methods have been developed which provide images of beam-sensitive materials without damaging them. The most commonly used figure of merit for such imaging methods is the electron dose, defined as the number of electrons per unit area incident on the sample. For accurate sample interpretation, it is important that an electron dose is used that is sufficiently high to provide contrast in the image, but sufficiently low such that the sample does not damage during the imaging process. However, as discussed in Section 2.3, the contrast mechanisms for each imaging method varies.

In a recent review, Egerton highlighted that it is essential to image beam-sensitive materials using electron doses below a certain damage threshold, but it is also necessary to maximise the information obtained from a given experiment [51]. For a particular value of electron dose, some imaging methods provide greater image contrast than others, i.e. they have a higher *dose-efficiency*. The dose-efficiency is related to several factors, such as the amount of signal collected, the detector geometry and how the data is used to form an image. For example, FPP methods use signal from the entire BF disc, in contrast to BF and ADF imaging which use approximately 10% of electrons in the detector plane (see Section 2.3). However, although incoherent BF (IBF) imaging also uses the entire BF disc, it is less dose-efficient than BF or ADF imaging. This is because the entire signal collected from the BF disc is integrated which increases noise and averages over interference effects which provide valuable sample information.

One of the most common figures of merit for comparing the performance of differ-

ent HRTEM and STEM imaging techniques is the contrast transfer function (CTF). As discussed in Section 2.2.4, the CTF is a semi-quantitative measure of the amount of contrast transferred from the sample to the image, as a function of spatial frequency. For phase-contrast imaging techniques, the CTF is commonly referred to as the phase-contrast transfer function (PCTF). The weight with which each spatial frequency is transferred to the image is generally not a constant and each imaging method will possess its own characteristic CTF. The ideal CTF is one which transfers a broad range of spatial frequencies to the image plane, while maintaining a high SNR in the image.

In HRTEM, the PCTF is an oscillating function which decays until it reaches zero at the information limit (see Section 2.2.4 for further details). There are contrast reversals which complicate image interpretation, particularly at higher spatial frequencies where atomic-resolution information may reside. The contrast reversals are generally minimised by experimentally adjusting the aberration function prior to image acquisition [99], or by using an aberration-corrected instrument (Section 2.2.4) [111] . Furthermore, focal series and tilt series acquisition followed by exit-wave reconstruction can provide a PCTF free of contrast reversals such that atomic-resolution information can be easily interpreted [93, 114, 171]. However, sample information from low spatial frequencies are typically transferred to the image with poor contrast. This is due to the dependence of the PCTF on the sine of the wave aberration function (Section 2.2.4). The contrast transfer of low spatial frequencies can be improved by acquiring images using large defocus values. For example, to image biological structures containing spatial frequencies of 0.1 nm^{-1}, defocus values greater than 1μm are needed [229]. These images can be acquired as part of a focal series, after which reconstruction methods can be performed to obtain an exit-wave with a broad information transfer [115]. Alternatively, the transfer of low spatial frequen-

cies can be improved by inserting phase plates into the microscope column (Section 2.2.4) [90, 91, 116]. The application of phase plates removes the need to acquire images using large defocus values and has been applied to cryo-electron microscopy with great success [116, 117]. However, beam-induced charging of phase plates is known to cause experimental errors [118].

In recent studies, it has been demonstrated that the PCTF of electron ptychography enables higher dose-efficiency than many common HRTEM and STEM imaging techniques [197, 207]. For example, the PCTF inherent to conventional SSB and WDD ptychography is a broad function with zero contrast reversals, enabling dose-efficient imaging without the need for hardware phase plates or serial image acquisition. Furthermore, incoherent imaging and spectroscopic mapping can be performed simultaneously with electron ptychography, further increasing the level of information obtainable for a given electron dose. However, in order to perform ptychographic reconstruction of 4D STEM data with a high dose-efficiency, the experimental settings must be optimised. In this chapter, the PCTF of electron ptychography will be discussed and experimentally measured in order to maximise the dose-efficiency of future experiments.

5.2 The PCTF for SSB ptychography

In Section 2.2.4, the phase-contrast transfer function (PCTF) for HRTEM and BF STEM imaging, and its dependence on objective lens aberrations, was discussed. For SSB ptychography, the interference between overlapping diffraction discs (the DO regions) provides phase-contrast in the ptychographic reconstruction, even in the absence of aberrations. The quality of the ptychographic reconstruction is, however, dependent upon the size of the DO regions (Figure 3.3). The PCTF for SSB ptychography is typically defined by the area of the DO regions at each spatial frequency. This was firstly derived geometrically by Yang *et al.* [207], where, for an ideal lens system and a probe convergence semi-angle α, the PCTF can be written as:

$$PCTF(\omega) = \mathrm{Re}\left\{\frac{2}{\pi}\left[cos^{-1}\left(\frac{\omega}{2}\right) - cos^{-1}\left(\omega\right) + \omega\sqrt{1-\omega^2} - \frac{\omega}{2}\sqrt{1-\left(\frac{\omega}{2}\right)^2}\right]\right\} \quad (5.1)$$

where $\omega = Q_p/\alpha$, and $PCTF(\omega)$ is nonzero for $0 < \omega < 2$. For simplicity, the spatial frequency Q_p is expressed in units of angle (mrad) rather than reciprocal distance. From Equation (5.1), it can be shown that the maximum spatial frequency, beyond which zero contrast is transferred to the image, is set by 2α. Thus, the bandwidth of the contrast transfer, and the subsequent resolution obtainable, for an SSB reconstruction scales linearly with α. This means that the contrast transfer function can be tuned for a particular experiment by choosing a suitable value for α. This is achieved in practice by adjusting the diameter of the STEM objective aperture.

Alternatively, the PCTF can be defined as a function of shifted aperture functions [230]. Using the same notation as in Section 3.3.2, the PCTF can be written as:

$$PCTF(Q_p) = \frac{\sum_{\mathbf{K_f}} |\zeta(\mathbf{K_f}, \mathbf{Q_p})|}{2 \sum_{\mathbf{K_f}} |A(\mathbf{K_f})|} \tag{5.2}$$

where

$$\zeta(\mathbf{K_f}, \mathbf{Q_p}) = A^*(\mathbf{K_f})A(\mathbf{K_f} - \mathbf{Q_p}) - A(\mathbf{K_f})A^*(\mathbf{K_f} + \mathbf{Q_p}) \tag{5.3}$$

For aberration-free conditions, Equations (5.1) and (5.2) yield the same result[1]. Equation (5.2) can also incorporate the complex component of the shifted aperture functions if the aberrations have been accurately determined. It should be noted that, as is the case for HRTEM, the PCTF for ptychography is defined for the case of a weak-phase-object (WPO). For stronger phase-objects, the phase-contrast is no-longer linearly proportional to the projected potential, due to the non-negligible interference between diffracted beams. As a result, the WPOA breaks down and Equation (3.15) cannot be simplified further. In this case, transmission cross-coefficients or numerical methods need to be considered to determine the contrast transfer properties of an imaging method [105]. However, in this chapter, the WPOA is assumed throughout.

To aid the physical interpretation of Equations (5.1) and (5.2), the PCTF for SSB ptychography is plotted in Figure 5.1. The shape of $G(\mathbf{K_f}, \mathbf{Q_p})$ is illustrated for ω = 0.25, 0.75, 1.25 and 1.75 respectively, and the DO regions have been shaded in blue. It can be seen that, unlike in HRTEM or BF STEM imaging, the PCTF is free of contrast reversals, which simplifies data interpretation. However, there is a characteristic decay in the transfer at low and high spatial frequencies. This arises from the small DO regions at these spatial frequencies, as displayed in Figure 5.1. As a result, the PCTF for SSB ptychography is effectively a band-pass filter, which

[1] In contrast to some of the existing literature, a factor of 2 has been included in the denominator of Equations (5.1) and (5.2) on order to normalise the PCTF to the area of a single DO region.

strongly transfers a particular range of spatial frequencies to the image, while suppressing other spatial frequencies within the PCTF and rejecting spatial frequencies greater than 2α. This is particularly useful for imaging materials with a narrow range of spatial frequencies, for which the probe convergence semi-angle can be adjusted to maximise the contrast from important spatial frequencies in the sample. However, the band-pass PCTF limits the range of spatial frequencies that can be transferred in a single phase reconstruction. For example, consider a crystalline nanoparticle embedded in a biological structure By adjusting the convergence angle to maximise the contrast of the high spatial frequency nanoparticle information, the contrast of the biological structure will be reduced, and vice versa.

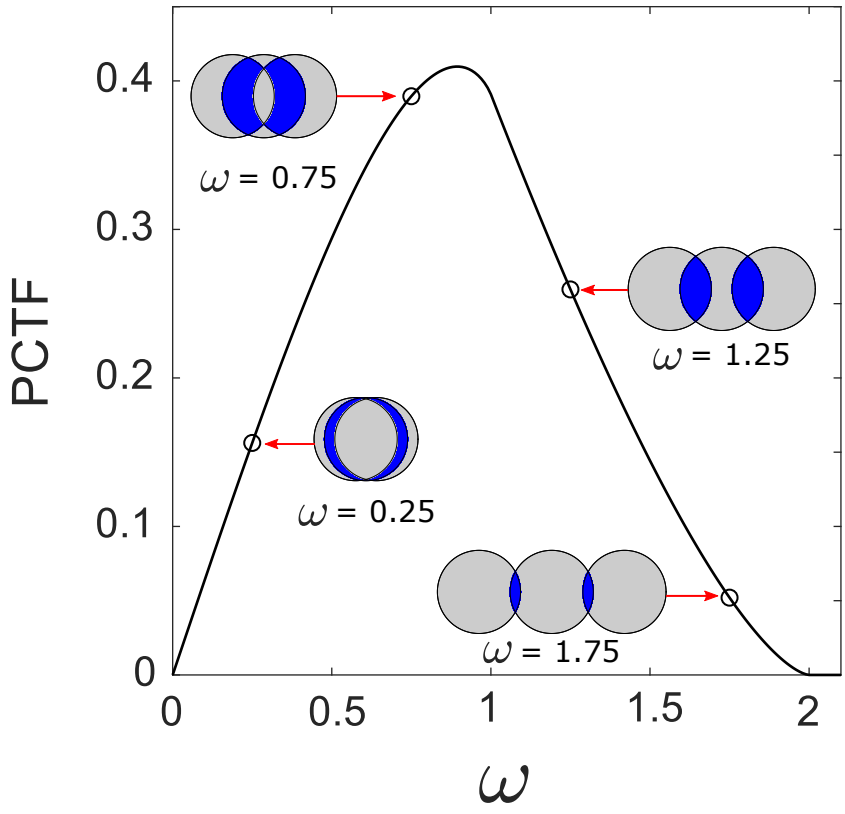

Figure 5.1: Phase contrast transfer function (PCTF) for SSB ptychography. The shape of $G(\mathbf{K_f}, \mathbf{Q_p})$ has been plotted for $\omega = 0.25$, 0.75, 1.25 and 1.75.

5.3 Experimental contrast transfer for an amorphous sample

In the previous section, both the theory and physical interpretation of the PCTF for SSB ptychography was introduced. It was also discussed how, by tuning the probe convergence semi-angle α, the PCTF for SSB ptychography can be optimised to transfer a particular range of spatial frequencies to the phase reconstruction. In this section, the practical implications of this will be examined by experimentally measuring the contrast transfer for SSB ptychography using phase reconstructions of an amorphous material. Amorphous specimens possess a continuous range of spatial frequencies throughout an aperture-limited diffraction space. As such, the strength with which each spatial frequency is transferred to the phase reconstruction should be directly proportional to the PCTF. For this experiment, the 4D STEM data was acquired from an amorphous carbon sample using an acceleration voltage of 80 kV. Data sets were obtained using two different STEM objective aperture diameters. The corresponding probe convergence semi-angles were 7.5 and 14.4 mrad, and the cumulative electron dose in each case was 1.6×10^7 e^- nm^{-2} and 3.3×10^7 e^- nm^{-2}, respectively.

Although commonly described as a technique for imaging crystalline materials [190, 191, 194], FPP methods are also applicable to non-crystalline materials. For ptychographic imaging of crystalline samples, each discrete (Bragg) reflection contributes a diffracted disc to the detector plane, and the information-rich DO regions in $G(\mathbf{K_f}, \mathbf{Q_p})$ are located at discrete $\mathbf{Q_p}$ values determined by the reciprocal-space locations of each reflection. For amorphous materials, the detector plane contains a continuous range of diffracted discs. As a result, atomic-resolution imaging is not the most effective technique for the structural determination of amorphous materials.

Two of the most common TEM methods used to analyse amorphous samples are radial distribution functions (RDFs) and fluctuation electron microscopy (FEM). RDFs are used to determine the distribution of atoms over large volumes of amorphous material using CTEM diffraction patterns or 4D STEM data sets [231]. In contrast, FEM is a hybrid real/reciprocal space technique used to probe the medium-range ordering in amorphous solids, which cannot be determined using RDFs, by calculating the variance of speckly dark-field CTEM or STEM images [232]. Alternatively, by applying ptychography to amorphous materials, the information-rich DO regions of $G(\mathbf{K_f}, \mathbf{Q_p})$ will be located across a continuous range of $\mathbf{Q_p}$ values. As a result, electron ptychography could be used to access specific $\mathbf{Q_p}$ values which are characteristic of the ordering in amorphous materials. Subsequently, these $\mathbf{Q_p}$ values could be used to reconstruct an exit-wave in order to identify the locations and structures of the ordered sample sub-regions. Example values of $G(\mathbf{K_f}, \mathbf{Q_p})$ for $|\mathbf{Q_p}| = 6$ mrad, as shown in Figure 5.2, clearly demonstrate the applicability of ptychography to amorphous materials, as first shown by Rodenburg and co-workers [189].

Following ptychographic reconstruction of the 4D STEM data, the Fourier transform of the reconstructed phase was calculated, the results of which are shown in Figure 5.3(a)–(b), before computing a radial average to determine the contrast transfer. This is the ptychographic equivalent to a Thon ring analysis in HRTEM [106]. Strictly, the resultant plot, $\gamma(Q_p)$, is the PCTF multiplied by the scattering factor at each spatial frequency, i.e.

$$\gamma(Q_p) = PCTF(Q_p) \times \mathrm{RA}\{FT\left[V_p(\mathbf{R_p})\right]\} \tag{5.4}$$

where RA denotes a radial average and $V_p(\mathbf{R_p})$ is the projected potential at each probe position. Figure 5.3 shows plots of (c) $\gamma(Q_p)$ and (d) $\gamma(\omega)$ for convergence semi-angles of 7.5 mrad (solid lines) and 14.4 mrad (dashed lines). To calculate the

true PCTF, the projected potentials of the amorphous carbon need to be simulated, and their Fourier transforms need to be divided from $\gamma(Q_p)$ to obtain $PCTF(Q_p)$. However, for the purposes of this study, $\gamma(Q_p)$ suffices to demonstrate the inherent decay at both low and high spatial frequencies. The dependence on choice of aperture on the transfer of Q_p values into the reconstruction is obvious, and the shape of $\gamma(\omega)$ is maintained, independent of the aperture diameter. This proof-of-principle experiment demonstrates that the aperture diameter, and hence the probe convergence semi-angle, can be tuned to optimise the experimental conditions for imaging a particular sample using SSB ptychography. In the next section, this strategy will be applied in order to optimise the ptychographic reconstructions for a crystalline sample.

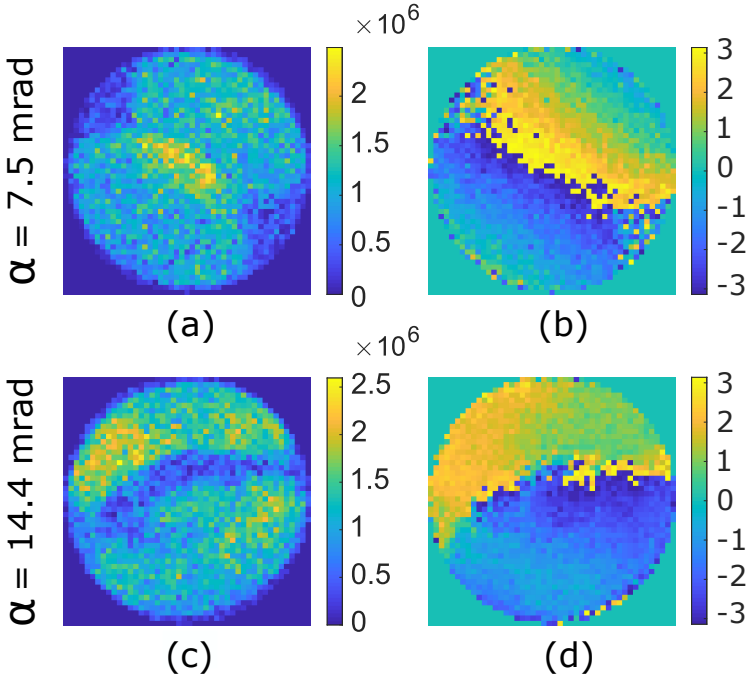

Figure 5.2: (a),(c) modulus (arb. units) and (b),(d) phase (radians) of $G(\mathbf{K_f}, \mathbf{Q_p})$ for data sets obtained from an amorphous carbon sample, plotted as a function of $\mathbf{K_f}$ at an example spatial frequency, $|\mathbf{Q_p}| = 6$ mrad. The probe convergence semi-angles used for this experiment are (a)–(b) 7.5 mrad and (c)–(d) 14.4 mrad.

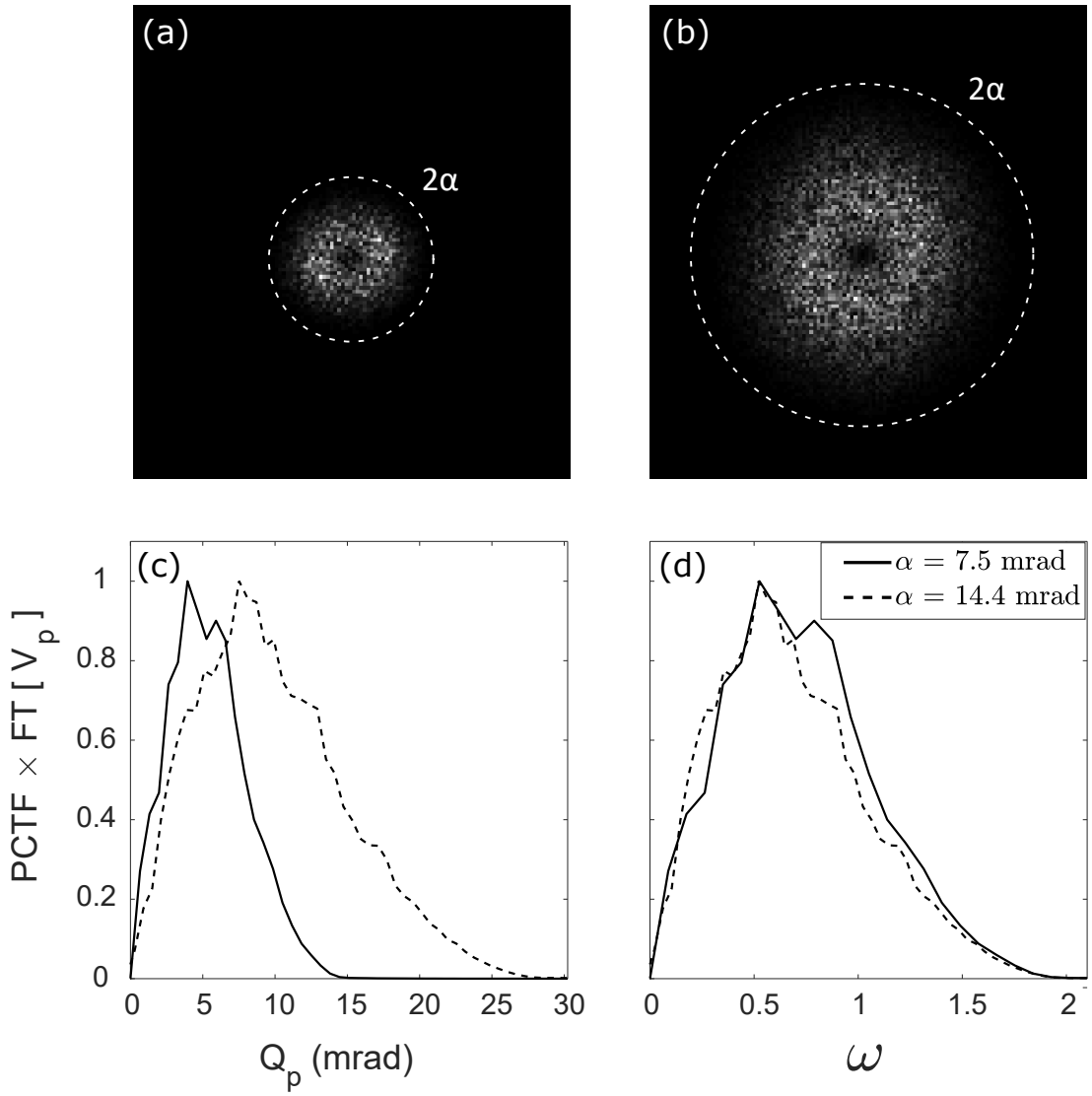

Figure 5.3: Power spectrum of the SSB phase reconstructions from amorphous carbon for (a) $\alpha = 7.5$ mrad and (b) $\alpha = 14.4$ mrad. The dashed circles correspond to the 2α-limit beyond which no spatial frequencies are transferred to the reconstructed phase. (c) – (d) Azimuthal average of (a) (solid lines) and (b) (dashed lines) with respect to (c) Q_p and (d) ω.

5.4 Experimental contrast transfer for a crystalline sample

In Section 5.3, it was demonstrated that the bandwidth of the PCTF for SSB ptychography scales with the probe convergence semi-angle α. This means that using a larger value of α will transfer a broader range of spatial frequencies $\mathbf{Q_p}$ to the ptychographic reconstruction, as demonstrated for an amorphous carbon sample in Figure 5.3. Furthermore, the PCTF determines the relative strength with which each $\mathbf{Q_p}$ value is transferred to the phase reconstruction, as described by Equations (5.1) and (5.2). Figure 5.3 shows that the $\mathbf{Q_p}$ values of the amorphous carbon near the centre of the PCTF are strongly transferred to the phase reconstruction, while lower and higher $\mathbf{Q_p}$ values are suppressed.

For crystalline samples, there exist a discrete set of Bragg reflections, located at a discrete set of spatial frequencies $\mathbf{Q_p}$, which contribute to the real-space image. Thus, for ptychographic reconstructions of these samples, it is essential to choose a probe-forming aperture which transfers $\mathbf{Q_p}$ values that correspond to the important length scales in the sample with maximum contrast. As an example, consider a sample containing reflections at discrete spatial frequencies, such as those in a graphene monolayer. If a similar 4D STEM convergence semi-angle series is acquired as for an amorphous carbon sample and the phase is reconstructed using electron ptychography, the effects of the PCTF can be visualised more clearly. The results of this experiment are shown in Figure 5.4.

The PCTF for each convergence semi-angle is shown in Figure 5.4(a). The right-hand side of Figure 5.4 shows the SSB phase reconstruction from monolayer graphene samples using α = (b) 31.5 mrad, (c) 22.5 mrad, (d) 14.4 mrad and (e) 7.5 mrad. The

microscope emission current was constant (11 μA), such that the electron doses in Figure 5.4(b) – (e) were 2.3 $\times$ 10^8 e$^-$ nm^{-2}, 1.2 $\times$ 10^8 e$^-$ nm^{-2}, 5.4 $\times$ 10^7 e$^-$ nm^{-2} and 2.5 $\times$ 10^7 e$^-$ nm^{-2}, respectively. For the case of the atomic-resolution phase reconstructions shown in Figure 5.4(b) – (c), the aberrations were corrected during the reconstruction process. The reciprocal-space locations of the reflections corresponding to the $\{1\bar{1}00\}$ (blue line) and $\{2\bar{1}\bar{1}0\}$ (red line) reflections are plotted in Figure 5.4(a). Transfer of the $\{1\bar{1}00\}$ reflections is required to visualise the hexagonal graphene rings, while transfer of both $\{1\bar{1}00\}$ and $\{2\bar{1}\bar{1}0\}$ reflections is required to resolve the spacing between individual carbon atoms. For $\alpha = 31.5$ mrad, single atoms are clearly resolved and the PCTF transfers both the $\{1\bar{1}00\}$ and $\{2\bar{1}\bar{1}0\}$ reflections. Decreasing the convergence angle to 22.5 mrad, atomic resolution is still achieved (both the $\{1\bar{1}00\}$ and $\{2\bar{1}\bar{1}0\}$ reflections are resolved), but the contrast is reduced due to the position of the $\{2\bar{1}\bar{1}0\}$ reflections with respect to the PCTF. The achievable resolution is decreased, and the noise at higher $\mathbf{Q_p}$ values decreases the contrast. At $\alpha = 14.4$ mrad, only the $\{1\bar{1}00\}$ reflections are resolved as the second ring lies outside of the aperture-limited PCTF, while data recorded with $\alpha = 7.5$ mrad resolves neither family of reflections.

Conversely, for the case of a crystalline sample containing important structural information at lower spatial frequencies, a smaller aperture would be required to resolve important sample features with high contrast. Take, as an example, a crystalline sample with an interatomic distance of 0.5 nm. For an acceleration voltage of 80 kV, this equates to a spatial frequency magnitude of $|\mathbf{Q_p}| = 9$ mrad, which would be resolved at highest contrast using a convergence semi-angle of $\alpha = 20$ mrad. For samples containing important structural information at lower $\mathbf{Q_p}$ values, such as amorphous materials or biological structures, the optimal convergence angle would be considerably smaller. In summary, to maximise information for a given electron dose, a probe-forming aperture must be chosen such that all the spatial frequencies

of interest in the sample are transferred strongly, which is equivalent to their DO regions in $G(\mathbf{K_f}, \mathbf{Q_p})$ being as large as possible. This criterion also applies to other phase detection techniques such as DPC, CoM and integrated CoM (iCoM).

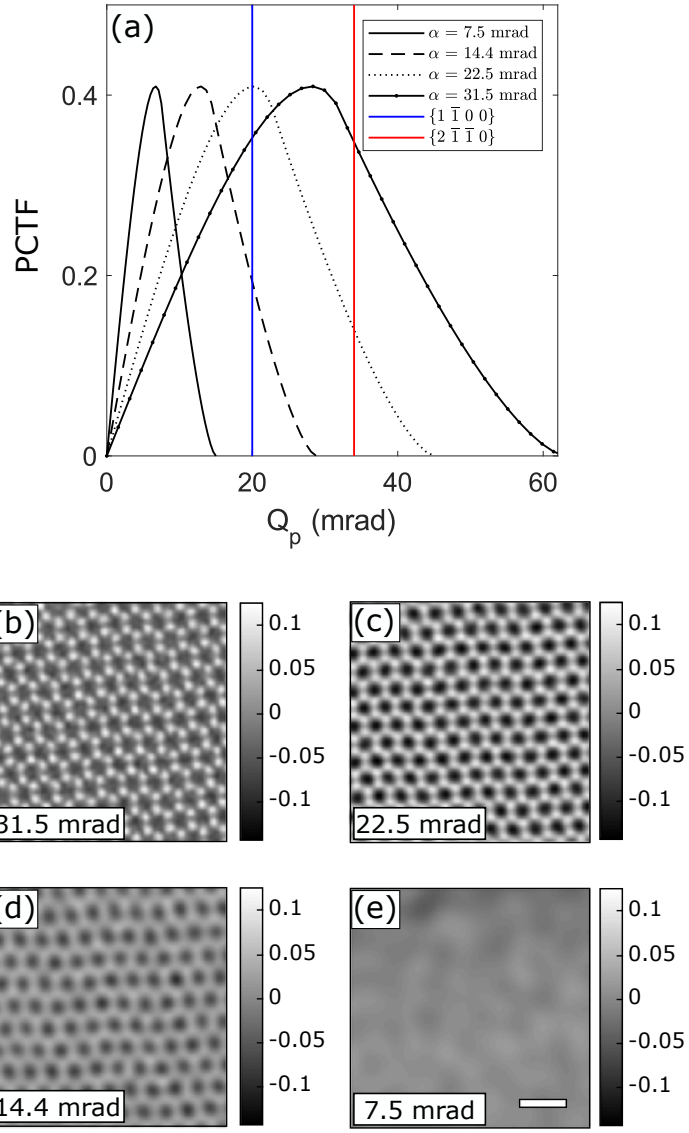

Figure 5.4: (a) PCTF for convergence semi-angles of 31.5 mrad, 22.5 mrad, 14.4 mrad, and 7.5 mrad. The red and blue vertical lines indicate reciprocal-space locations of the $\{1\bar{1}00\}$ and $\{2\bar{1}\bar{1}0\}$ families of reflections. Experimental phase reconstructions of graphene data for each of the convergence semi-angles in (a) are shown in (b)–(e). Scale bar: 0.5 nm. Greyscale: phase (radians).

5.5 Comparison of ptychographic PCTFs

In addition to choosing an optimum aperture for a given sample, there are still challenges in optimising ptychographic contrast. In SSB ptychography, the PCTF acts as an effective band-pass filter, suppressing both low and high spatial frequencies, as shown in Figure 5.5. This enables selection of the information transferred to the image plane, at the expense of lost information at other spatial frequencies. To compare the transfer properties of SSB ptychography to iterative methods, the PCTF of the ePIE method was calculated for boron, titanium and silver isolated atom simulations (V_{acc} = 200 kV, α = 22.48 mrad) using the simulation package, MULTEM [228]. By deconvolving the potential from the ptychographic phase for each atom, the PCTFs could be determined, as shown in Figure 5.5. There are a number of important differences between SSB and ePIE ptychography that are seen in this result. Firstly, ePIE uses data beyond the BF disc in order to obtain resolution beyond the 2α limit of SSB ptychography, and in some experiments the resolution has reached 5α [19, 204]. However, recent experiments have shown that the resolution limit approaches 2α as the strength of scattering is decreased or the noise level is increased [211]. Secondly, ePIE performs a forward calculation which aims to provide flat contrast transfer across all spatial frequencies in the sample. In practice, the decay of the transfer is determined by the noise of high spatial frequencies. In contrast to the SSB method, the ePIE method converges to a solution for $\psi(\mathbf{r})$ which transfers almost all spatial frequencies with equal weight, before decaying to zero at spatial frequencies beyond 2α.

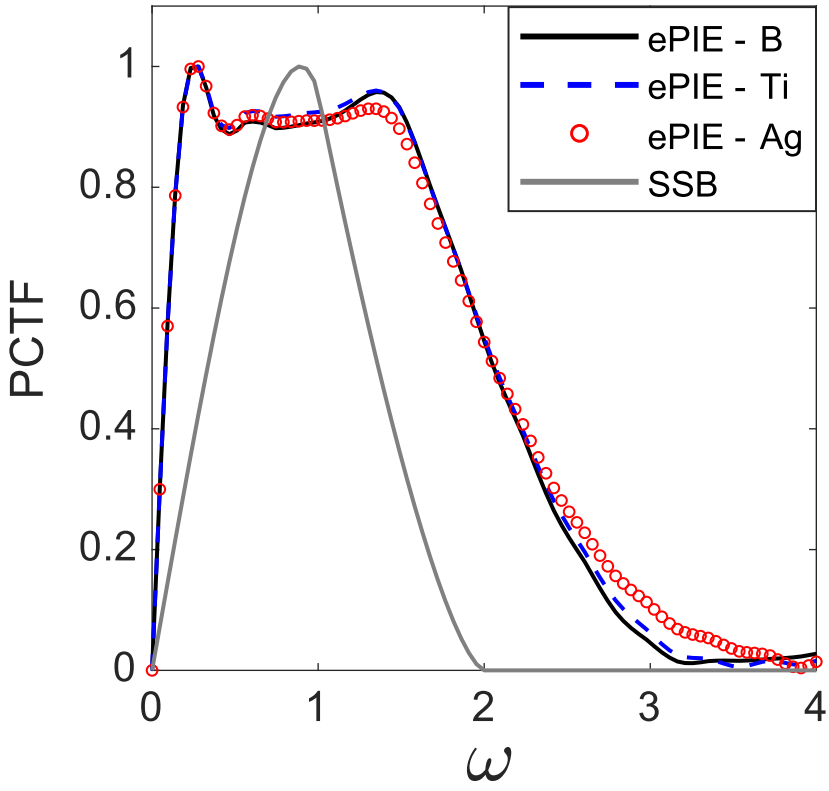

Figure 5.5: Plots of the normalised PCTF for the ePIE method, generated using isolated atom simulations. The theoretical PCTF for the SSB method is included for reference (grey line).

To illustrate the effects of the PCTFs of SSB and ePIE methods, consider an aberration-corrected SSB phase reconstruction of a functionalised carbon nanotube (FCNT) shown in Figure 5.6(a) (previously presented using the WDD method in [18]). The data was acquired using an acceleration voltage of 80 kV, a convergence semi-angle of 22 mrad and an electron dose of 2.7×10^6 e^- nm^{-2}. Although the phase reconstruction shows atomic resolution, another feature is noticeable: a dark fringe which outlines the FCNT. This fringe is most likely a direct result of the suppression of low and high spatial frequencies. To demonstrate this, Figure 5.6(b) shows the phase reconstruction of the same FCNT using the ePIE algorithm [14]. There is sufficient signal outside the BF disc for ePIE to reconstruct the FCNT at a resolution beyond the $\omega = 2$ limit of SSB ptychography. Furthermore, the broad transfer win-

dow of the ePIE method does not transfer edge artefacts to the image plane as for SSB ptychography, but a slowly-varying phase ramp in the vacuum is present across the entire field of view. This is possibly due to the form of the PCTF for ePIE at low spatial frequencies which amplifies low-frequency noise. In DPC and CoM studies, these artefacts are commonly attributed to shifts in the BF disc caused by the probe scan system. However, for atomic-resolution studies, the disc shifts are often negligible. To observe whether this is the case for the 4D STEM data obtained from the FCNT, the centre-of-mass (CoM) image was obtained, and is plotted in Figure 5.6(c). It is evident that the vacuum regions exhibit a homogeneous centre-of-mass, which suggests that the phase ramp is not caused by disc shifts, but is more likely due to the reconstruction process. A future investigation of the phase ramps present in ePIE reconstructions may be worthwhile, but will not be further discussed here. The phase ramp can be avoided by applying a band-pass filter, such as that intrinsic to SSB ptychography, to the Fourier transmission function $\Psi(\mathbf{Q_p})$. The result of applying this filter to the ePIE phase reconstruction, as shown in Figure 5.6(d), is very similar to the SSB phase as shown in Figure 5.6(a): no slowly-varying phase ramp, but a rapid phase dip around the FCNT walls.

It should be noted that band-pass filters are also applied to iDPC imaging. This is because the PCTF is inherently determined by the Fourier transform of the probe intensity, and as a result, low spatial frequencies are transferred to the image plane with high contrast [62]. A high-pass filter is often applied to the iDPC images in order to suppress the artefacts introduced by amplifying low spatial frequencies [146].

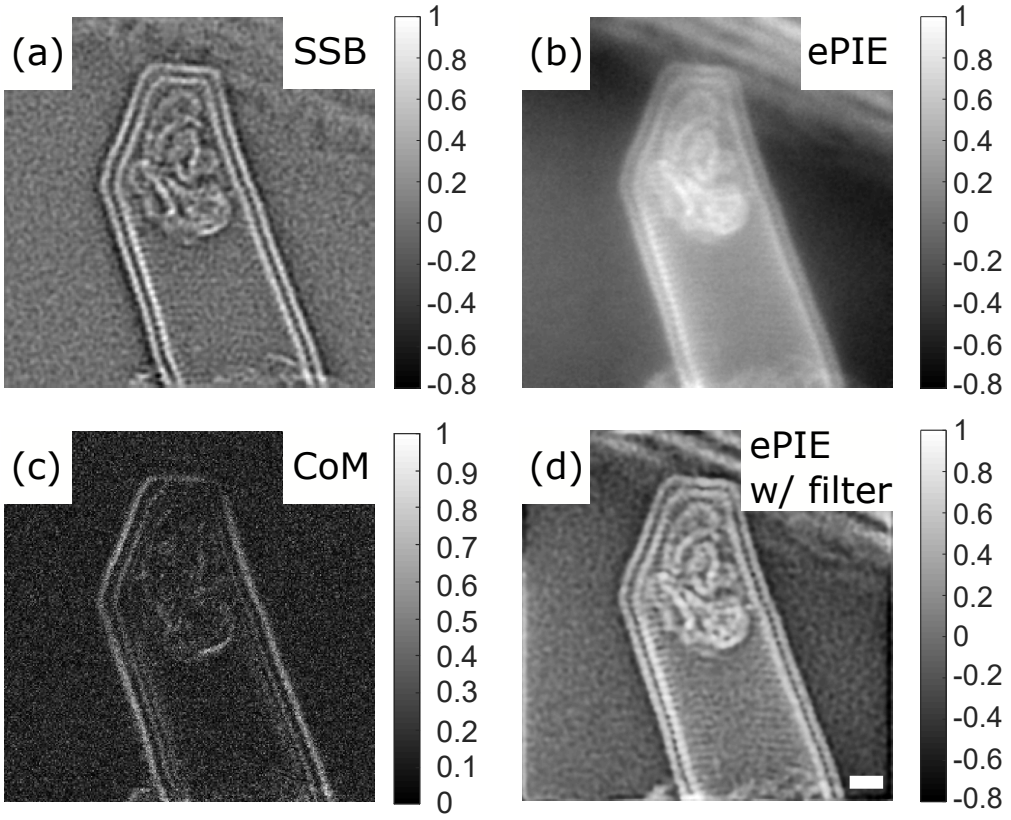

Figure 5.6: Aberration-corrected ptychographic phase reconstructions of a FCNT using (a) the SSB method and (b) the ePIE method. The centre-of-mass image, shown in (c), confirms that the low-frequency phase ramp present in (b) is not due to scan-induced disc shifts. The ramp can be removed from the phase reconstruction by applying an SSB band-pass filter, as shown in (d). Scale bar: 0.5 nm. The maximum value in each reconstruction has been normalised to 1 for consistency.

5.6 Conclusions

In this chapter, the contrast transfer for SSB ptychography has been described and experimentally verified. Although the contrast transfer in electron ptychography, as for any STEM imaging method, is strongly dependent on the electron dose, the relative contrast transfer also depends on the aperture function (aperture size and wave aberrations). Even at high electron doses, a poorly chosen aperture will provide a reconstruction with a high noise level. In contrast to SSB ptychography, the ePIE

method possesses a broader PCTF at high electron doses, extending beyond the information limit of STEM instruments. However, low spatial frequency artefacts will contribute to the ePIE phase reconstruction unless they are suppressed by filtering. In iDPC imaging, a high-pass filter is used to the same effect. With this in mind, a quantitative description of the noise in 4D STEM data would provide valuable insights into the optimal transfer function for SSB ptychography. This will form the focus of the next chapter.

Chapter 6

Optimisation of dose-efficiency for focused-probe ptychography

In this chapter, the contrast transfer theory of SSB ptychography is further developed in order to increase the dose-efficiency of the ptychographic method. Firstly, a model of the statistical noise present in ptychographic data is derived. Using this model, two target transfer functions are developed in order to boost the contrast transfer of low and high spatial frequencies in ptychographic reconstructions. Finally, the performance of SSB and WDD methods is compared for low-dose experimental data.

6.1 Introduction

In Chapter 5, the contrast transfer properties of SSB and ePIE methods were compared using 4D STEM data from a FCNT (Figure 5.6). Although both SSB and ePIE methods were performed using the same experimental data set, the output complex transmission functions were not identical. This difference is dependent on how much of the 4D STEM data set is used by each algorithm, and how each reconstruction algorithm is performed to produce a complex transmission function. For example, the SSB method only uses the BF disc in the reconstruction process, while the ePIE method also uses information from beyond the BF disc, which can lead to resolution improvement if this is needed. However, for very thin samples or at low electron doses, the super-resolution capabilities decrease and the ePIE resolution limit converges to the 2α limit for SSB ptychography [211]. Furthermore, each algorithm weights different sample features with different strengths in the reconstruction. This weighting function, known as the PCTF (see Chapter 5), is different for every imaging technique, including alternate methods of ptychography.

The contrast transfer properties of SSB and ePIE methods are significantly different at low and high spatial frequencies. The PCTF for SSB ptychography is effectively a band-pass filter dependent on the area of the DO regions in the Fourier overlap function $G(\mathbf{K_f}, \mathbf{Q_p})$. This results in strong contrast transfer for most spatial frequencies in this bandwidth, and weak contrast transfer for low and high spatial frequencies at each end of the pass-band. In contrast, the ePIE algorithm performs forward calculations which aim to provide unity transfer of all spatial frequencies to the image plane, and as such, possesses a broader PCTF than the SSB method. However, the intrinsic PCTF of each technique does not necessarily take into consideration the effects of noise amplification. For ePIE and iDPC imaging, the PCTF at low spatial frequencies is greater than that for SSB ptychography, but a Fourier filtering step must be used to

suppress the noise and artefacts introduced by these low spatial frequencies (Section 5.5 and [146]). Conversely, the PCTF inherent to SSB ptychography suppresses low and high spatial frequencies which may contain valuable sample information with a reasonably high SNR.

In general, the intrinsic PCTF for ptychography is, to an extent, a function of the algorithm used. The imaging process can be regarded as being performed *in silico* and is therefore algorithm dependent. As a result, it is reasonable to assume that one can choose an alternative, *target*, transfer function to optimise the ptychographic dose-efficiency. In order to choose a suitable target transfer function, one must first understand how noise is transferred to each spatial frequency $\mathbf{Q_p}$. In the following section, a model for the noise present in $G(\mathbf{K_f}, \mathbf{Q_p})$ will be derived to deduce the optimal target transfer function for SSB ptychography.

6.2 Formal description of noise in $G(\mathbf{K_f}, \mathbf{Q_p})$

One of the unique properties of SSB ptychography is its intrinsic suppression of noise. As it is known where the information from each spatial frequency is expressed in the detector plane, the SSB method suppresses noise by selecting only the DO regions in which the sample information may be located, and rejecting the contributions from the rest of the detector plane. In this section, a formal description of the statistical noise present in $G(\mathbf{K_f}, \mathbf{Q_p})$ is provided in order to quantitatively determine the form of this noise suppression process. In the following section, a suitable target transfer function is defined with respect to the derived noise model.

Consider a 4D STEM data set acquired from a WPO. As first introduced in Chap-

ter 3, the complex amplitude of the wave in the detector plane is $M(\mathbf{K_f}, \mathbf{R_p})$. The wave intensity, $|M(\mathbf{K_f}, \mathbf{R_p})|^2$, is recorded on a pixellated detector. It is assumed that the expected value of a pixel is weakly varying for a WPO and, as such, is assumed to be constant with respect to both scattering vector $\mathbf{K_f}$ and probe position vector $\mathbf{R_p}$. Subsequently, it can be assumed that the BF disc is constant. Furthermore, the contribution of electrons scattered outside the BF disc is ignored.

The expected value of electrons recorded by each pixel is defined as D. This can alternatively be defined as the electron dose per detector pixel. The deviation of a pixel measurement from the expected value D (i.e. the noise at each pixel) is defined as $X_M(\mathbf{K_f}, \mathbf{R_p})$. For the case of a perfect detector where only statistical noise is present in the acquired data[1], $X_M(\mathbf{K_f}, \mathbf{R_p})$ follows a Poisson distribution. As a result, the standard deviation of the noise, $\sigma(X_M(\mathbf{K_f}, \mathbf{R_p}))$, is equal to the square root of the electron dose at each pixel. Therefore, its variance is given by

$$\mathrm{Var}(X_M(\mathbf{K_f}, \mathbf{R_p})) = \sigma(X_M(\mathbf{K_f}, \mathbf{R_p}))^2 = D \tag{6.1}$$

Let us assume that the BF disc contains N_K pixels such that the expected value of electrons in the BF disc is $N_k D$. Each measurement is independent of any other measurement recorded at another $\mathbf{K_f}$ or $\mathbf{R_p}$ value, and hence the noise at each pixel is uncorrelated with respect to both $\mathbf{K_f}$ and $\mathbf{R_p}$. As such, the noise distribution is white noise and is equally distributed across all spatial frequencies $\mathbf{Q_p}$ and all real-space position vectors $\mathbf{r}$. Because the noise between separate detector pixels in the BF disc is uncorrelated, let us first consider the noise contribution of one single detector pixel denoted by a reciprocal-space vector $\mathbf{K_a}$. Let us subsequently define $X_M(\mathbf{R_p})$ as the statistical noise in the acquired 4D STEM data $|M(\mathbf{K_f}, \mathbf{R_p})|^2$ at $\mathbf{K_a}$, for each probe

[1]In practice, true counting detectors closely approximate the statistical noise determined from theory.

position $\mathbf{R_p}$. To calculate the noise of $G(\mathbf{K_f}, \mathbf{Q_p})$ at $\mathbf{K_a}$, a two-dimensional discrete Fourier transform of $X_M(\mathbf{R_p})$ is performed with respect to probe position $\mathbf{R_p}$:

$$X_G(Q_x, Q_y) = \sum_{1}^{N_x} \sum_{\mathbf{1}}^{N_y} X_M(R_x, R_y) \exp\left(i2\pi\left(\frac{Q_x\, R_x}{N_x} + \frac{Q_y\, R_y}{N_y}\right)\right) \tag{6.2}$$

where R_x, R_y and Q_x, Q_y are the x- and y-components of $\mathbf{R_p}$ and $\mathbf{Q_p}$ respectively, and N_x, N_y correspond to the total number of probe positions in the x- and y-scan directions. As the Fourier transform of the noise is complex, the variance of its real and imaginary components must be considered separately. The variance of the real component can be expressed as:

$$\mathrm{Var}\Big(\mathrm{Re}\big\{X_G(Q_x, Q_y)\big\}\Big) = E\left[\Big(\mathrm{Re}\big\{X_G(Q_x, Q_y)\big\}\Big)^2\right]$$

$$= \sum_{1}^{N_x} \sum_{\mathbf{1}}^{N_y} E\left[\left(\mathrm{Re}\left\{X_M(R_x, R_y) \exp\left(i2\pi\left(\frac{Q_x\, R_x}{N_x} + \frac{Q_y\, R_y}{N_y}\right)\right)\right\}\right)^2\right] \tag{6.3}$$

where E is the expected value operator. Using dummy variables to expand the square, and taking the Dirac delta function to reduce number of variables, one obtains

$$\mathrm{Var}\Big(\mathrm{Re}\big\{X_G(Q_x, Q_y)\big\}\Big) = \sum_{1}^{N_x} \sum_{\mathbf{1}}^{N_y} E\Big[\big(X_M(R_x, R_y)\big)^2\Big]\, cos^2\left(2\pi\left(\frac{Q_x\, R_x}{N_x} + \frac{Q_y\, R_y}{N_y}\right)\right) \tag{6.4}$$

which simplifies to

$$\mathrm{Var}\Big(\mathrm{Re}\big\{X_G(Q_x,Q_y)\big\}\Big) = \sigma^2\big(X_M(R_x,R_y)\big)\sum_{1}^{N_x}\sum_{\mathbf{1}}^{N_y}\cos^2\left(2\pi\left(\frac{Q_x\,R_x}{N_x}+\frac{Q_y\,R_y}{N_y}\right)\right) \tag{6.5}$$

Using the trigonometric identity $\cos^2(x) = \frac{1}{2}(1+\cos(2x))$, and evaluating the geometric series of both resultant terms:

$$\mathrm{Var}\Big(\mathrm{Re}\big\{X_G(Q_x,Q_y)\big\}\Big) = \frac{\sigma^2\big(X_M(R_x,R_y)\big)}{2}\,N_x\,N_y = \frac{D}{2}\,N_x\,N_y \tag{6.6}$$

i.e. the variance of the real component of $X_G(Q_x,Q_y)$ is directly proportional to the electron dose per pixel. Because the noise in each detector pixel is also uncorrelated to other detector pixels within the BF disc, their contributions can be added in order to determine the cumulative real component of the noise in $G(\mathbf{K_f},\mathbf{Q_p})$ for a particular imaging mode. For 4D STEM imaging modes such as CoM imaging, every value of $\mathbf{K_f}$ in $G(\mathbf{K_f},\mathbf{Q_p})$ is used in the image reconstruction process. However, for SSB ptychography, only the detector pixels within the DO regions are used to reconstruct the complex transmission function (see Figure 5.1). Thus, the cumulative real component of the noise in $G(\mathbf{K_f},\mathbf{Q_p})$ for SSB ptychography is given by

$$\mathrm{Var}\Big(\mathrm{Re}\big\{X_{G:SSB}(\mathbf{K_f},\mathbf{Q_p})\big\}\Big) = \frac{D}{2}\,N_x\,N_y\,N_{DO}(\mathbf{Q_p}) \tag{6.7}$$

where $N_{DO}(\mathbf{Q_p})$ is the number of detector pixels which cover the DO region at each spatial frequency $\mathbf{Q_p}$. The same analysis can be applied to the imaginary component

of the noise in $G(\mathbf{K_f}, \mathbf{Q_p})$ to obtain

$$\mathrm{Var}\Big(\mathrm{Im}\big\{X_{G:SSB}(\mathbf{K_f}, \mathbf{Q_p})\big\}\Big) = \frac{D}{2}\, N_x\, N_y\, N_{DO}(\mathbf{Q_p}) \tag{6.8}$$

The real and imaginary components are independent of each other and as a result, their variances can be added together. This yields the variance of the modulus of the noise in $G(\mathbf{K_f}, \mathbf{Q_p})$ for SSB ptychography:

$$\mathrm{Var}\Big(\big|X_{G:SSB}(\mathbf{K_f}, \mathbf{Q_p})\big|\Big) = D\, N_x\, N_y\, N_{DO}(\mathbf{Q_p}) \tag{6.9}$$

Finally, the standard deviation can be obtained by taking the square root of Equation (6.9), i.e.

$$\sigma\Big(\big|X_{G:SSB}(\mathbf{K_f}, \mathbf{Q_p})\big|\Big) = \sqrt{D\, N_x\, N_y\, N_{DO}(\mathbf{Q_p})}$$

$$= C\, \sqrt{N_{DO}(\mathbf{Q_p})} \tag{6.10}$$

where $C = \sqrt{D\, N_x\, N_y}$ is the total electron dose at a particular detector pixel summed over all probe positions in the data set. Therefore, the noise present in $G(\mathbf{K_f}, \mathbf{Q_p})$ can be described by a random walk – a modulus contribution which scales with $\sqrt{N_{DO}(\mathbf{Q_p})}$, and a random phase contribution.

Equation (6.10) demonstrates the inherent noise suppression in SSB ptychography. Techniques that use all pixels in the detector plane, such as CoM and iCoM imaging, possess a uniform (white) noise spectrum which includes contributions from each detector pixel. However, for SSB ptychography, the signal for a WPO is known to be located in the DO regions of $G(\mathbf{K_f}, \mathbf{Q_p})$ and as such, detector pixels which do not lie in these regions are rejected before performing the reconstruction (see Figure 5.1).

This results in an increased SNR by a factor of $\sqrt{(N_k/N_{DO}(\mathbf{Q_p}))}$ at each spatial frequency $\mathbf{Q_p}$ versus methods which use the entire BF disc. Furthermore, Equation (6.10) provides a method by which the PCTF can be normalised to the noise in SSB ptychography. This can be demonstrated by plotting $\sigma\Big(\big|X_{G:SSB}(\mathbf{K_f},\mathbf{Q_p})\big|\Big)$ as a function of ω, as shown in Figure 6.1. Alternatively, Figure 6.1 can be defined as a weighting function of the noise present in $G(\mathbf{K_f},\mathbf{Q_p})$. If this weighting function is incorporated into the PCTF of SSB ptychography, the SNR of the resulting ptychographic reconstructions can be maximised. In the next section, Equation (6.10) will be used in order to develop an optimal target transfer function for SSB ptychography.

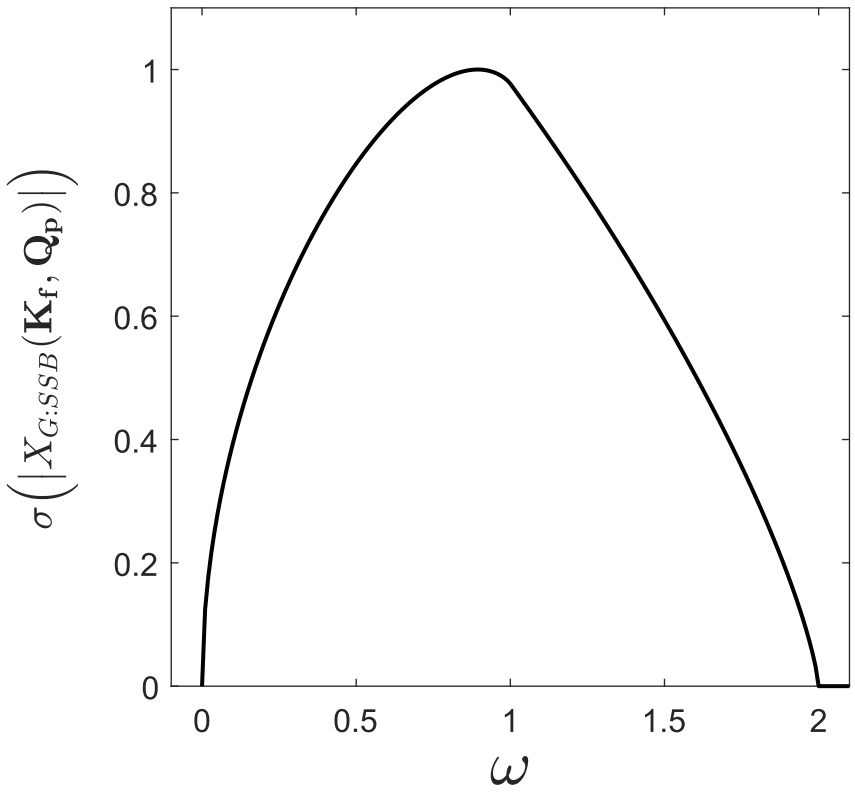

Figure 6.1: Plot of $\sigma\Big(\big|X_{G:SSB}(\mathbf{K_f},\mathbf{Q_p})\big|\Big)$ versus ω as derived in Equation (6.10). The maximum value of $\sigma\Big(\big|X_{G:SSB}(\mathbf{K_f},\mathbf{Q_p})\big|\Big)$ has been normalised to 1.

6.3 Target transfer functions

In Chapter 5, it was demonstrated that SSB ptychography only uses the signal present in the DO regions to reconstruct the specimen transmission function, while suppressing the noise which lies elsewhere in the detector plane. As a result, the PCTF of SSB ptychography is generally described as being proportional to the strength of the signal in $G(\mathbf{K_f}, \mathbf{Q_p})$ (i.e. the area of the DO regions), as expressed in Equation (5.1). However, this PCTF does not account for the SNR at each spatial frequency, and as such, the contrast of low and high spatial frequencies is inherently reduced in the reconstruction. In the previous section, a model of the noise distribution in $G(\mathbf{K_f}, \mathbf{Q_p})$ with respect to spatial frequency $\mathbf{Q_p}$ was derived in order to describe the noise suppression process of ptychography. It was shown that the noise at each $\mathbf{Q_p}$ value is directly proportional to the square root of the area of the DO region, suggesting that the optimal contrast at low and high spatial frequencies is greater than that provided by the intrinsic PCTF. In this section, two new target transfer functions are applied to electron ptychography reconstructions using experimental and simulated data, in order to amplify the signal of low and high spatial frequencies.

Three separate transfer functions were applied to ptychographic reconstructions: 1) the intrinsic PCTF (Figure 6.2(a)), 2) a flat transfer function (Figure 6.2(b)) and 3) a noise-normalised transfer function (Figure 6.2(c)). The target transfer functions displayed in Figure 6.2(b)–(c) can be synthesised by applying a weighting function to the Fourier transform of the ptychographic exit-wave in order to boost the contribution of low and high spatial frequencies to the image plane. The performance of these transfer functions were compared using ptychographic reconstructions calculated for 4D STEM data sets from a simulated carbon atom and experimental monolayer graphene. The same acceleration voltage (V_{acc} = 80 kV), convergence angle (α = 22.5 mrad) and probe sampling ($|\Delta\mathbf{R_p}|$ = 0.013 nm) conditions were used in

each case. The 4D matrix for the carbon atoms was simulated using the MULTEM code [228]. For each graphene data set, the residual aberrations were corrected using post-processing techniques. Isolated carbon atom simulations were reconstructed using an electron dose identical to the experiment, and are plotted as insets to the graphene reconstructions in Figure 6.2. The results for each transfer function are described below.

6.3.1 Intrinsic transfer function

In conventional SSB ptychography, the boundaries of the reconstructed phase of the carbon atoms have dips due to the band-pass nature of the PCTF (Figures 5.1 and 6.2). This manifests itself as a dark halo around the carbon atom simulation in Figure 6.2(d), and as a dip in the graphene hexagons in Figures 6.2(g) and (j). Furthermore, as previously shown in Figure 5.4, the atomic spacings of graphene (i.e. the $\{2\bar{1}\bar{1}0\}$ reflections) are poorly resolved using a probe convergence semi-angle of 22.5 mrad.

6.3.2 Flat transfer function

Applying a target transfer function to the carbon atom such that spatial frequencies up to $2\alpha/\lambda$ are transferred with equal weight, the phase reconstruction in Figure 6.2(e) is obtained. This transfer function is similar to that provided by the ePIE method, and is the equivalent to normalising the contrast transfer to the area of the DO region at each Q_p value. A Hann window roll-off function was applied at low and high values of Q_p to reduce artefacts. The implementation of this target transfer function removes the negative phase dip visible in Figure 6.2(d). For the case of graphene shown in Figure 6.2(h), applying a flat transfer function resolves the atomic spacings with

higher contrast. The flat transfer function enables a broader range of information transfer at high electron doses (i.e. $\sim 10^8$ e^- nm^{-2}). However, the frequency-boosting process results in high-frequency ringing which manifests itself as phase peaks at the centre of the graphene hexagons. These artefacts resemble individual atoms and may subsequently result in the inaccurate structural identification of materials. Furthermore, if a flat transfer function is applied to data at lower electron doses (i.e. $\sim 10^7$ e^- nm^{-2}) as shown in Figure 6.2(k), noise amplification from low and high spatial frequencies degrades the quality of the reconstruction.

6.3.3 Noise-normalised transfer function

An alternative approach to extending the contrast transfer window for SSB ptychography would be to synthesise a target transfer function which is normalised to the noise distribution, as previously discussed in Section 6.2 and by Seki *et al.* [233]. This is implemented in practice by using the square root of the intrinsic PCTF as the target transfer function, which is the equivalent of dividing the integrated Fourier signal by its square root (i.e. the shot noise) at each spatial frequency. This target transfer function has the advantage of mitigating the artefacts of the intrinsic SSB PCTF (i.e. the carbon atom reconstruction shown in Figure 6.2(f)), while keeping the noise at a constant level across all spatial frequencies. The application of this transfer function to the graphene reconstructions is shown in Figures 6.2(g) and (j), where the noise is suppressed while still resolving the the $\{2\bar{1}\bar{1}0\}$ reflections with high contrast.

In conclusion, by using a noise-normalised target transfer function, the contrast transfer is proportional to the SNR at each $\mathbf{Q_p}$ value, thereby increasing the information bandwidth and dose-efficiency of SSB ptychography while avoiding artefacts introduced by low spatial frequencies or amplified noise. A flat target transfer function can also be applied to increase the information bandwidth of SSB ptychography,

but only at high electron doses for which the noise is not amplified significantly. In the next section, the effects of noise amplification in WDD ptychography will be considered.

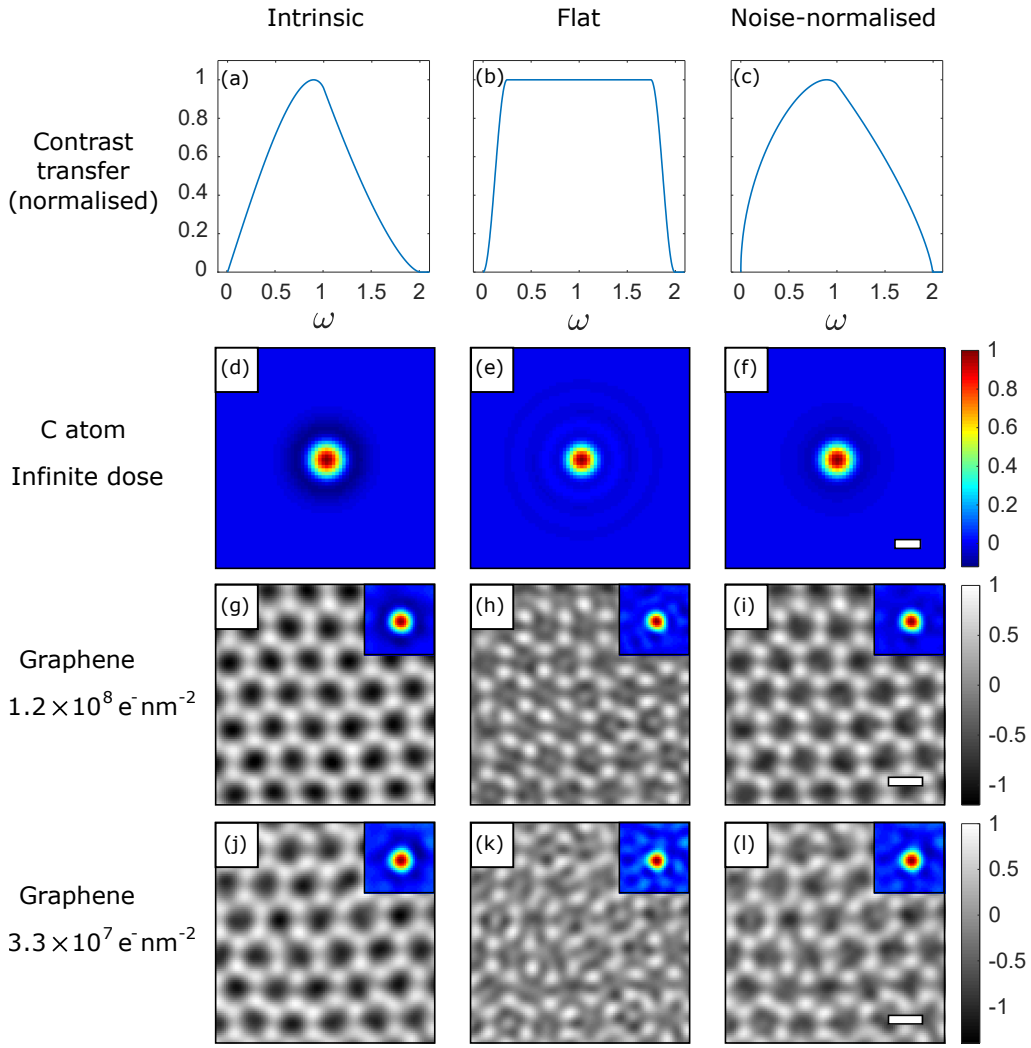

Figure 6.2: Comparison of transfer functions used in SSB ptychography. (a) Intrinsic, (b) flat and (c) noise-normalised contrast transfer functions. (d)–(l) SSB phase reconstructions using the transfer functions plotted in (a)–(c). The maximum phase in each reconstruction has been normalised to 1 for consistency. Colour bar: normalised phase. (d)–(f) Simulated carbon atom using infinite dose. Scale bar: 0.1 nm. (g)–(i) Experimental phase reconstructions of graphene (aberration-corrected) using a dose of 1.2×10^8 e^- nm^{-2}. Scale bar: 0.2 nm. (j)–(l) Experimental phase reconstructions of graphene (aberration-corrected) using a dose of 3.3×10^7 e^- nm^{-2}. Scale bar: 0.2 nm. Insets of (g)–(l): phase reconstructions of carbon atom simulations at the same dose used for the experimental graphene.

6.4 Further noise minimisation by avoiding a deconvolution step

As discussed in Sections 3.3.2 and 3.3.3, the two most common methods of non-iterative focused-probe ptychography are the SSB and WDD methods. Although both techniques effectively provide the same result for a weak-phase-object, there are subtle differences which should affect the choice of technique. The SSB method assumes a weak-phase-object as the sample, whereas for 'stronger' phase-objects, the WDD method is more applicable [13, 17, 18]. However, due to the nature of the Wiener deconvolution, one must exercise caution when applying the WDD method at low electron dose [13]. In particular, the order of ε_r (Section 3.3.3) affects how much signal and noise is suppressed in the reconstruction. To demonstrate this, Figure 6.3 shows a phase reconstruction of an aluminosilicate zeolite[2] (ZSM-5) at an electron dose of 2×10^4 e^- nm^{-2} using (a) the SSB method and (b)-(d) the WDD method for different values of ε_r. The wedge-like sample increases in thickness towards the left-background of each reconstruction. Nevertheless, the steady increase in phase values demonstrates the validity of the WPOA for this sample. Due to the arbitrary nature of the *in silico* reconstruction process, the absolute values of the phase in each reconstruction are also arbitrary and, as such, have been normalised in Figure 6.3. The SSB reconstruction, shown in Figure 6.3(a), avoids a deconvolution step and thus avoids noise amplification. In contrast, reconstructing the transmission function using the WDD method for small values of ε_r (0.01–0.1) as used in the the literature [18,194] can give rise to noise amplification, as seen in Figures 6.3(b) and (c) . Using $\varepsilon_r = 1$ as shown in Figure 6.3(d) effectively suppresses the noise, however, such a large filter parameter may also suppress useful sample information. Therefore, to improve robustness to noise for low-dose focused-probe electron ptychography, it is advisable

[2]The experimental method by which this data was acquired will be described in further detail in Chapter 7.

to use the SSB method where applicable.

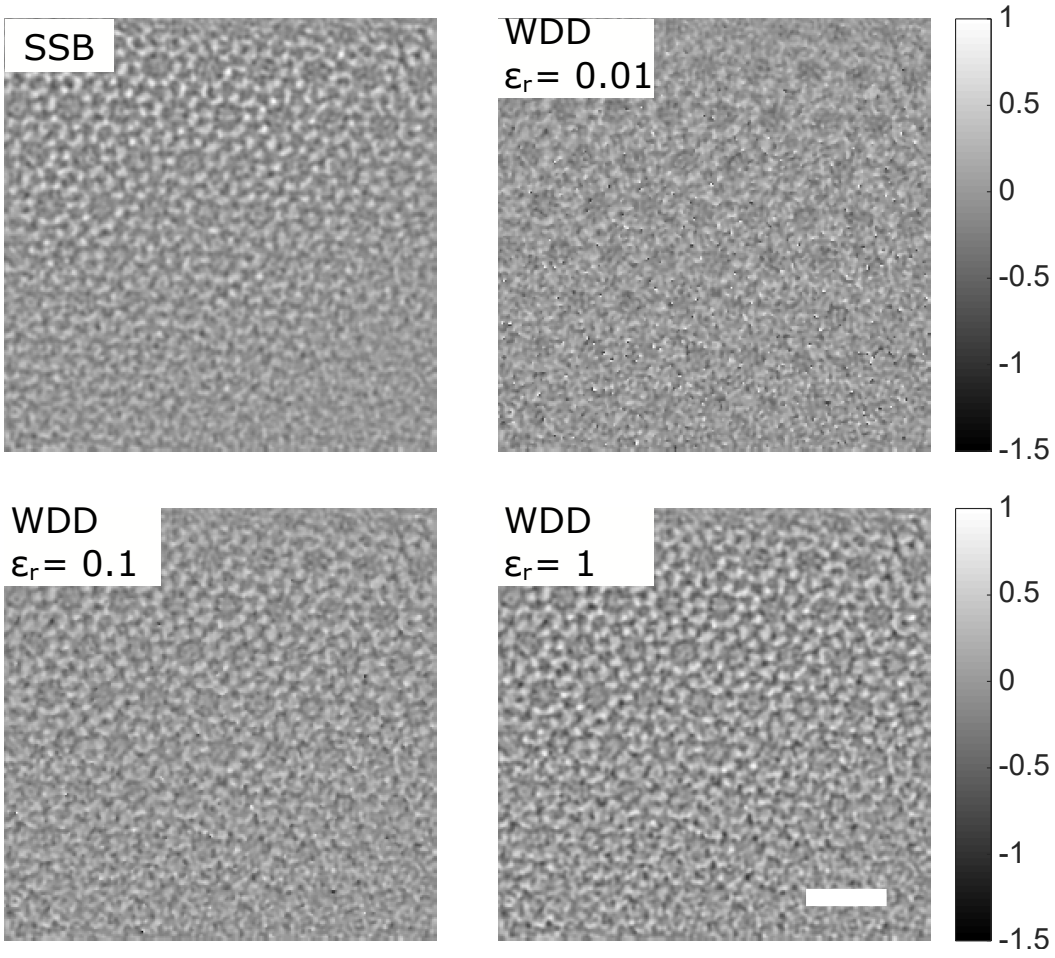

Figure 6.3: Comparison of phase reconstruction methods for ZSM-5 at an electron dose of 2×10^4 e^- nm^{-2}. (a) SSB phase reconstruction. (b)-(d) WDD phase reconstructions for ε_r =0.01, 0.1 and 1, respectively. Scale bar: 2 nm. The maximum phase in each reconstruction has been normalised to 1 for consistency.

6.5 Conclusions

In this chapter, a post-processing strategy was introduced to the ptychographic workflow in order to increase the dose-efficiency of the output reconstructions. If a suitable aperture is used but low spatial frequencies are not transferred, normalising the contrast transfer to the signal-to-noise ratio will increase the contrast. A model for the

noise present in $G(\mathbf{K_f}, \mathbf{Q_p})$ was derived to support this strategy. Subsequently, it was demonstrated that SSB ptychography suppresses the noise outside the double-overlap regions of the detector plane, unlike other common 4D STEM imaging methods such as CoM and iCoM. Furthermore, recent theoretical studies have shown that the noise-normalised transfer function of SSB ptychography is broader than those for CoM techniques [233]. Finally, it was shown that avoiding a deconvolution step in FPP is another method by which the effects of unwanted noise can be suppressed. By adopting the experimental and post-processing strategies presented in Chapters 5 and 6, the electron dose required for ptychographic imaging can be minimised. The subsequent increase in dose-efficiency will enable atomic-resolution, high-SNR phase reconstructions at lower electron doses, thus extending the capabilities of ptychography for imaging beam-sensitive materials. In the next chapter, a data acquisition strategy will be introduced in order to further extend the low-dose capabilities of FPP.

Chapter 7

Binary electron ptychography

The author is grateful to Dr Chen Huang for providing the ZSM-5 sample used in this chapter, and the experimental support team at ePSIC.

In Chapters 5 and 6, several strategies to optimise the dose-efficiency of ptychography were demonstrated. In this chapter, a solution to another major limitation of electron ptychography – the slow scan speeds at which data is recorded – will be proposed. In particular, the development and application of FPP using binary 4D STEM data sets will be discussed. Firstly, the challenge of imaging beam-sensitive materials in STEM will be outlined, before proposing binary data acquisition as a solution. Next, the application of ptychography using binary data acquired from a beam-sensitive material (ZSM-5) will be demonstrated. Finally, the limitations of this acquisition mode will be discussed. The work presented in this chapter has been partially reproduced from:

C. M. O'Leary *et al.*, 'Phase reconstruction using fast binary 4D STEM data', *Applied Physics Letters*, vol. 116, p. 124101, 2020,

with the permission of AIP Publishing.

7.1 Introduction

Although the combination of 1) focused-probe 4D STEM data acquisition using direct electron detectors (DEDs) and 2) phase reconstruction techniques such as ptychography can provide atomic-resolution imaging with great sensitivity, its application is limited by slow scanning speeds (∼1,000 fps). Despite recent detector advances (Section 2.4), 4D STEM phase-imaging experiments remain difficult to perform on beam-sensitive materials. Most modern low-noise integrating CMOS and electron counting detectors can record full-frame individual CBED patterns at $\sim 10^3$ fps, while more traditional non-pixellated (i.e. ADF and DPC) detectors can operate at speeds faster than 10^5 fps. The relatively slow speeds of DEDs make 4D STEM acquisitions more susceptible to scan distortions, sample drift and changes to lens aberrations and ultimately, set a minimum possible dose. For example, with a frame rate of 1,000 fps and a probe step size of 0.02 nm, a current of 0.5 pA would correspond to an electron dose of 7.7×10^6 e^- nm^{-2}.

Unfortunately, many important materials systems contain light elements and/or weak bonds which are easily damaged by the electron beam at such doses, i.e. organic and functional materials such as lithium-ion battery components (Section 2.6.4.3) [17], hybrid perovskites [3,234], metal-organic frameworks [235] and zeolites [236,237]. For the case of MFI-type zeolites, the above dose value is 1–2 orders of magnitude greater than the critical dose [236, 237]. A beam current of several femtoamperes (10^{-15} A) would be needed to image such materials without damaging them, for which it is not practically possible to navigate the sample and align the microscope.

Low-dose imaging (4.0×10^4 e^- nm^{-2}) has been previously demonstrated for electron ptychography on MoS_2, using a defocused probe that spreads the electron flux over a substantial illumination area, combined with an iterative ptychographic algorithm (ePIE) [199,204]. In this chapter, low-dose methods of focused-probe 4D STEM data acquisition, combined with FPP reconstruction techniques, will be addressed.

In the following subsections, a solution to the slow-scan limitation of DEDs will be presented by changing the counting depth of a MerlinEM system to 1-bit such that each detector pixel can only record either 0 or 1. This enables the detector frame rate to be increased to 12,500 fps. Phase reconstruction techniques will then be applied to 1-bit 4D STEM data recorded from a beam-sensitive material (ZSM-5) after which the limitations and opportunities of using this technique will be discussed.

7.2 Increase frame rates via 1-bit data acquisition

Fortunately, modern DEDs possess a variety of acquisition modes, several of which can operate at frame rates faster than 1,000 fps (see Table 2.1). Many CCD and integrated CMOS detectors enable hardware binning and windowing [7], increasing frame rates at the expense of pixel resolution and field of view, respectively. For the case of FPP techniques, the sampling requirements in the reciprocal-space detector plane are relaxed such that the quality of the reconstruction is negligibly affected by the binning process (Section 4.2.3) [207]. Furthermore, faster detector speeds have shown negligible effects on the quality of phase reconstructions at high electron doses. In a recent study, Huth *et al.* demonstrated the ptychographic reconstruction of monolayer graphene using the JEOL 4DCanvas with four-fold binning at two separate detector speeds: the commercial frame rate of 4,000 fps (2.3×10^8 e^- nm^{-2}), and an increased, prototype frame rate of 7,500 fps (1.2×10^8 e^- nm^{-2}) [222]. There was a negligible

difference in the quality of the two reconstructions, demonstrating that ptychography is robust at the lower electron doses imposed by increased detector speeds.

Other electron counting detectors allow the user to increase the detector speed at the expense of dynamic range, i.e. the range of intensity values that can be recorded at each detector pixel. For example, for a 6-bit counting mode, each detector pixel can record between 0 and 63 counts. However, as the bit-depth is decreased, the readout time of the on-chip counters decreases and consequently detector frame rates can be increased significantly (see Table 4.2). In the next section, an experimental method for 4D STEM data acquisition using a counter depth of 1-bit (i.e. which can record either 0 or 1) will be described.

7.3 Experimental methods

7.3.1 Detector settings

The 4D STEM data sets were obtained from an aluminosilicate zeolite sample (ZSM-5) using a Quantum Detectors MerlinEM system installed on a JEM ARM300CF (Section 4.1.2). As presented in Table 4.2, the system possesses a range of counting modes at 24-, 12-, 6- and 1-bit depths, which correspond to maximum frame rates of 600, 1,200, 2,200 and 12,500 fps respectively. In this chapter, each data set was acquired using 1-bit mode. The ZSM-5 sample thickness was approximately 5–10 nm, and as such, the effects of plural scattering and dynamical diffraction could be ignored.

7.3.1.1 Lower threshold voltage

Before acquiring the 4D STEM data, an appropriate lower threshold voltage (below which no count is recorded), V_{th}, was chosen for the MerlinEM system. The detector was operated in a continuous mode while V_{th} was changed, and the number of counts

recorded by the detector was observed. If the value of V_{th} is too low, each electron count is distributed into many pixels, possibly leading to saturation of the BF disc (i.e. every pixel would record a value of 1). However, if V_{th} is too high, electron events are not recorded. With this in mind, V_{th} was set at 50 kV such that each electron event in the data set was counted while reducing unwanted blurring. This effectively increases the modulation transfer function (MTF) of the detector. However, if the energy of any meaningful electron signal is below the threshold set by V_{th}, it is not counted by the detector. This would result in a decrease in the detector quantum efficiency (DQE) which would lead to phase reconstructions with a lower SNR [157]. A future, more comprehensive study of the effects of V_{th} on the MTF, the DQE and the subsequent quality of phase reconstructions may be worthwhile.

7.3.2 Choice of acceleration voltage

Despite the decreased detector quantum efficiency (DQE) of the MerlinEM system at high electron voltages [157], an acceleration voltage, V_{acc}, was chosen as 300 kV due to the electron-optical alignment of the microscope and the beam damage mechanisms of zeolites which have been shown to decrease at higher accelerating voltage [237, 238]. Initial trials of 1-bit 4D STEM experiments were performed at 80 kV using different materials, but changes to the electron-optical alignments that occurred at sub-picoampere beam currents provided insufficient reconstruction quality. This is not expected to be a problem for microscopes that are specifically designed to operate only at low acceleration voltages.

7.3.3 Pre-acquisition procedure

Prior to 4D data acquisition, ADF images were observed at lower magnification (1 Mx) on a conventional non-pixellated detector. The objective focus was adjusted to clearly show the reflections of the zeolite structure observed in a power spectrum calculated

in real time without damaging the sample. Once focused, the beam was blanked and the magnification was increased to 20 Mx, before recording the 4D STEM data on the MerlinEM system.

7.3.4 1-bit 4D STEM data acquisition

For this experiment, 256 × 256 CBED patterns, each consisting of 256 × 256 pixels, were recorded using 1-bit counting mode at 12,500 fps. To minimise the beam current at the sample, the probe convergence semi-angle was set to 7.6 mrad. This value was sufficient to resolve the ZSM-5 framework, while reducing noise at unwanted higher spatial frequencies. In other words, the Fourier space information required to resolve the zeolite structure was within the window allowed by the PCTF for SSB ptychography (Chapter 5). The probe step size at 20 Mx magnification was $|\mathbf{R_p}| = 0.04$ nm, which was safely within the $\lambda/4\alpha$ sampling limit of 0.06 nm.

7.3.5 Data processing

To reduce the computing RAM and disk memory required for data analysis, the detector plane was binned by a factor of four in both directions in post-processing, reducing the data to a 256 × 256 × 64 × 64 array. For this experiment, the diameter of the BF disc after binning was approximately 40 pixels and hence the detector plane was sufficiently sampled (see Section 4.2.3).

7.4 Results

7.4.1 1-bit CBED data

An example CBED pattern from a typical 4D data set is shown in Figure 7.1(a). Each frame has an average of 272 counts and the position-averaged CBED pattern is

displayed in Figure 7.1(b). The effective camera length was increased such that the diameter of the BF disc on the detector was 160 pixels. The 10 dead pixels in the BF disc shown in Figure 7.1(b) cover 0.05% of the BF disc area and have a negligible effect on the phase reconstructions. The incident beam current was lowered by decreasing the excitation voltage of the second anode, 'A2', and was measured using a Faraday cup. The beam current can also be measured by counting the electrons incident on the MerlinEM system. However, this requires careful calibration of the lower threshold voltage (see Section 7.3.2), and as such, this procedure was avoided. For this experiment, the beam current was measured as 0.3 pA, which corresponded to a cumulative electron dose of 1.0×10^5 e^- nm^{-2}. As shown in Figure 7.1(a), this beam current was sufficiently low such that each electron event was isolated within the CBED patterns.

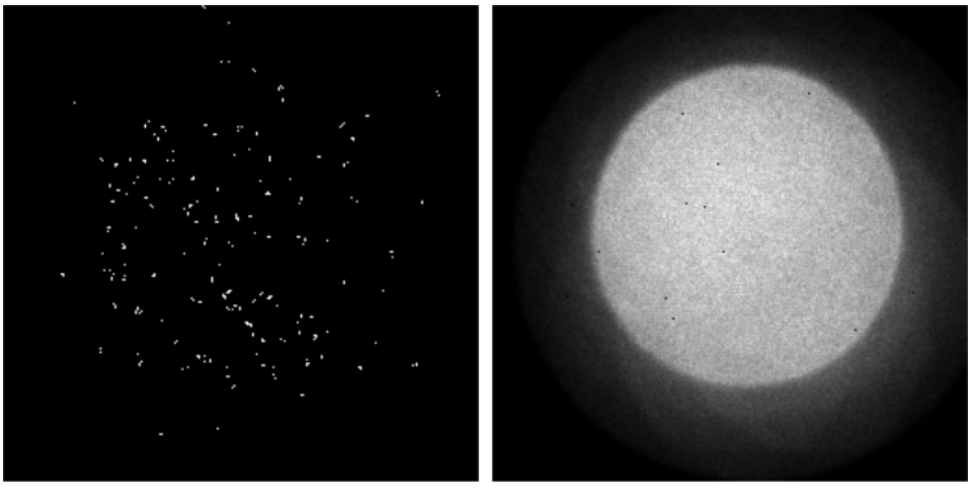

Figure 7.1: (a) Example CBED pattern and (b) position-averaged CBED pattern for ZSM-5 at an electron dose of 1.0×10^5 e^- nm^{-2}.

Recording 4D STEM data with a 1-bit counter depth is advantageous for several reasons. Firstly, for a frame rate of 1,000 fps, a 256×256 probe position scan would take over one minute to acquire. This is sufficiently long for specimen or low-order

aberration drift to have a detrimental effect on the acquired data. At 12,500 fps, a 256 × 256 probe position scan takes just over 10 seconds and drift rates are significantly reduced. In addition, faster frame rates enable data acquisition at higher, more optically favourable probe currents for a given electron dose. This is due to the increased accuracy of pre-acquisition aberration tuning at higher beam currents.

7.4.2 Fourier transform of $|M(\mathbf{K_f}, \mathbf{R_p})|^2$

After acquisition, the data was analysed as outlined in Section 4.4. As illustrated in Section 3.3.1, the first step of the FPP workflow is to perform a Fourier transform of the acquired data (i.e. $|M(\mathbf{K_f}, \mathbf{R_p})|^2$) to obtain $G(\mathbf{K_f}, \mathbf{Q_p})$. Figure 7.2 shows (a) the modulus and (b) phase of $G(\mathbf{K_f}, \mathbf{Q_p})$ for an example spatial frequency ($|\mathbf{Q_p}| =$ 4.9 mrad). Although each individual CBED pattern in the data set is sparse, the phase of $G(\mathbf{K_f}, \mathbf{Q_p})$ is still transferred with a high SNR. This demonstrates that the variation with respect to probe position of the statistical likelihood of electron arrival in a particular region of the detector is sufficient to enable phase detection. One advantage of SSB ptychography is that, because only the DO regions are used for the reconstruction process, much of the unwanted noise is rejected (Chapters 5 and 6).

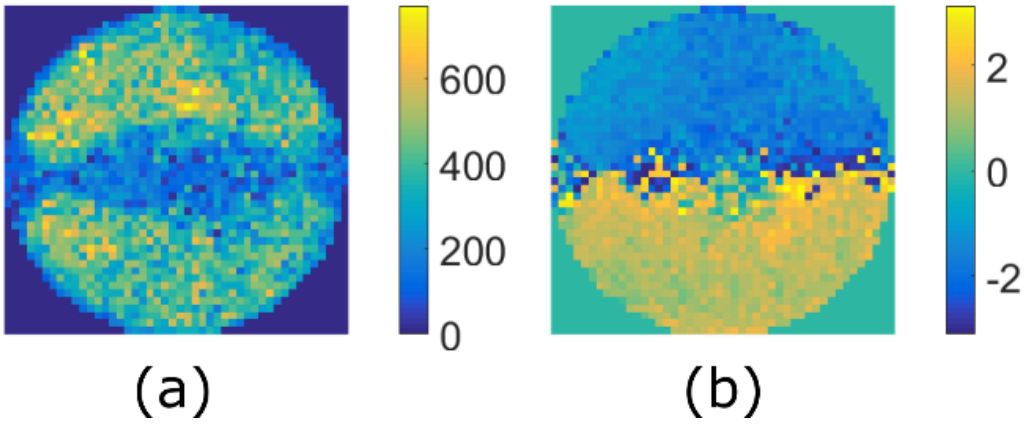

Figure 7.2: (a) Modulus (arb. units) and (b) phase (radians) of $G(\mathbf{K_f}, \mathbf{Q_p})$ for ZSM-5 at a spatial frequency magnitude of $|\mathbf{Q_p}| = 4.9$ mrad.

7.4.3 Phase reconstructions at 1.0×10^5 e^- nm^{-2}

After Fourier transform, the SSB ptychography method was performed on $G(\mathbf{K_f}, \mathbf{Q_p})$ (Sections 3.3.2 and 4.4.8) to provide phase reconstructions of the ZSM-5 sample. Due to the good alignment of the microscope and the small probe convergence semi-angle used for the experiment, aberration correction was not performed during the reconstruction process. To demonstrate the versatility of the data, another independent phase reconstruction method was also performed: integrated centre-of-mass (iCoM), i.e. iDPC using a pixellated detector [62].

The phase reconstructions produced from the binary 4D STEM experiment on ZSM-5 [010] are shown in Figure 7.3. The simultaneously obtained ADF image shown in Figure 7.3(a) reveals the zeolite structure, but with a poor SNR due to the low electron dose and light constituent atoms. The iCoM and SSB reconstructions are shown in Figures 7.3(b) and (c) respectively and both show atomically resolved contrast. A noise-normalised target transfer function was applied to the SSB phase reconstruction

to broaden the window of information transfer (Chapter 6). The power spectrum of the SSB phase reconstruction is shown in Figure 7.3(d), where the (10, 0, 0) reflection is resolved, corresponding to a spacing of 0.201 nm.

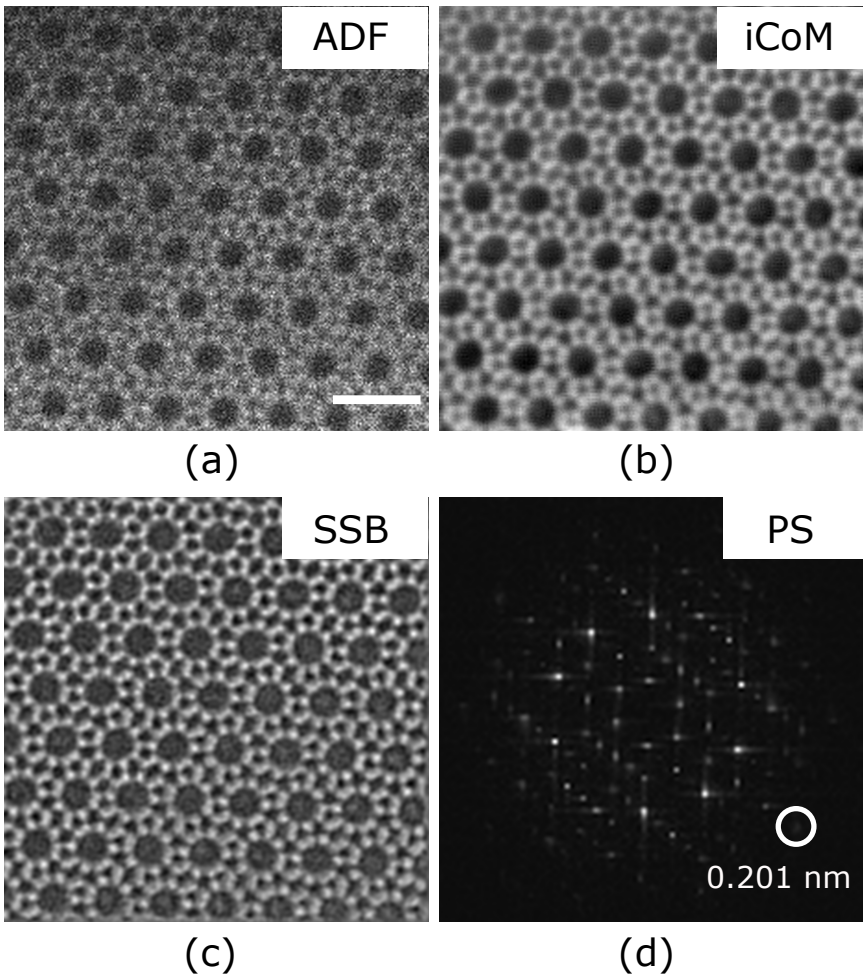

Figure 7.3: (a) ADF image, (b) iCoM reconstruction and (c) SSB reconstruction for ZSM-5 using an electron dose of 1.0 $\times$ 10^5 e^- nm^{-2}. Scale bar: 2 nm. The power spectrum (PS) of (c) is shown in (d). The (10, 0, 0) reflection, corresponding to a spacing of 0.201 nm, is marked with a white circle.

7.4.4 Phase reconstructions at 2.0 $\times$ 10^4 e^- nm^{-2}

To test the efficiency of phase imaging techniques at low dose using binary 4D STEM, the excitation voltage of the second anode was further lowered to obtain a beam current of 0.06 pA. A second data set was acquired, for which the cumulative electron

dose was 2.0 $\times$ 10^4 e^- nm^{-2}. An example CBED pattern for this data is shown in Figure 7.4(a). In this frame, there are a total of 19 detector counts, corresponding to 9 electron events. The iCoM and SSB reconstructions are shown in Figures 7.4(b) and (c) respectively. In this example the ZSM-5 region of interest is wedge-like, with a maximum thickness in the top left of the image. In the thicker region, the zeolite structure is resolved, but in the thinner region, there is insufficient scattering to provide significant sample information. The atomic columns are sharper in the SSB reconstruction, while the lower spatial frequencies are transferred more strongly in the iCoM image, as discussed in Chapters 5 and 6.

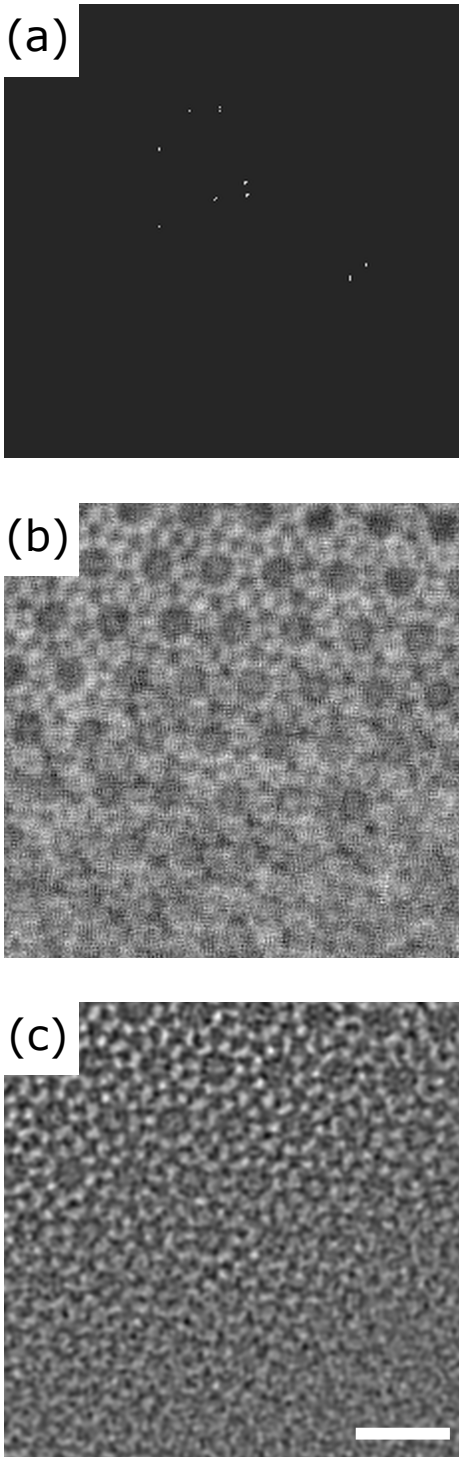

Figure 7.4: (a) Example CBED pattern, (b) iCoM reconstruction and (c) SSB reconstruction for ZSM-5 using a cumulative electron dose of 2.0 × 10^4 e^- nm^{-2}. The scale bar for the phase reconstructions is 2 nm.

7.5 Limitations

As discussed in the previous section, there is a lower limit for the electron dose below which there is not enough signal in the 4D STEM data to reconstruct the phase of the specimen transmission function. Although this is primarily due to the unavoidable statistical noise which obscures the signal at low electron doses, improvements to the sensitivity may be achieved through further optimisation of the lower threshold voltage V_{th}. However, conversely at high electron dose ($\sim 10^8$ e^- nm^{-2}), 1-bit counting mode using a frame rate of 12,500 fps would lead to saturation of the BF disc. In this case, every pixel in the BF disc (excluding dead pixels) would record a value of '1', and there would be no structure in the CBED patterns or the resulting phase reconstructions. The upper limit of the electron dose can be increased by changing the effective camera length of the detector such that the BF disc is distributed over a larger detector area. If the BF disc covers a large array of pixels, further detector binning (i.e. 8-fold or 16-fold) may be applied in order to decrease the time required to perform the reconstruction. With state-of-the-art DEDs reaching speeds of 87,000 fps, future low-dose 4D STEM experiments may not require any change in probe current between sample screening and acquisition [159]. This will be essential for imaging light-element or beam-sensitive nanomaterials, for which large probe convergence semi-angles and minimal high-order aberrations are necessary.

7.6 Conclusions

In this chapter, the application of binary 4D STEM data to post-processing phase reconstruction techniques was demonstrated. The 1-bit counting mode on a MerlinEM system can record 10 times faster than 12-bit counting mode, which is within one order of magnitude of typical ADF imaging speeds. Importantly, the results demonstrate that DEDs do not need a high dynamic range to provide high-quality phase

reconstructions and that faster detectors should enable high-throughput, low-dose 4D STEM phase imaging in the near-future. Furthermore, multi-frame acquisition combined with image registration techniques is increasingly used to improve the SNR of STEM images and faster scanning will allow this approach to also be used with pixellated detectors [150, 239]. The application of ptychography using multi-frame data acquisition will be discussed in Chapter 8.

Chapter 8

Applications

In this chapter, a number of applications of the ptychographic technique will be demonstrated, each of which overcome barriers that are often faced when imaging with conventional STEM modes such as ADF, ABF and DPC imaging. The applications have been divided into three separate sections: 1) fusion of ptychography with existing acquisition methods, 2) discussion of the imaging capabilities of ptychography, and 3) application of ptychography to a challenging material: uranium dioxide.

8.1 Multi-frame 4D STEM and ptychography

The author is grateful to Dr Lewys Jones, who performed non-rigid registration on the multi-frame data sets presented in this section. Dr Gerardo Martinez (GM) performed the data acquisition and ptychographic analysis for the preliminary hBN study. I acquired the graphene data presented in this section and performed the subsequent ptychographic analysis. I also performed the data acquisition for the hBN study with GM.

8.1.1 Motivation

Electron ptychography is highly sensitive to changes in the phase of the exit-wave and, subsequently, the projected atomic potential of the sample under illumination (see Equation (3.16)). Not only can ptychography determine the projected atomic potential of light elements such as boron and carbon, but it can also detect the redistribution of charge due to bonding effects in a thin sample.

The influence of bonding on the charge distribution of materials has historically been determined using two experimental methods: 1) X-ray diffraction and 2) CBED using HRTEM instruments. In both cases, the charge redistribution due to bonding in a sample is determined by calculating the differences between experimental and model structure factors of Bragg reflections [21]. Once the structure factor differences have been determined, the difference in the charge density can be expressed as a deformation density map [240]. In X-ray diffraction studies, high-order structure factors can be accurately determined, but extinction effects due to dynamical diffraction prevent the accurate determination of low-order structure factors which are most sensitive to the valence electrons [241]. Fortunately, by utilising the effects of strong dynamical diffraction in TEM, the low-order structure factors can be de-

termined from CBED techniques [242, 243]. In order to accurately determine a wide range of structure factors for a particular sample, both X-ray diffraction and CBED techniques should be performed. However, for thin samples (i.e. <10 nm), these techniques are not effective because dynamical diffraction does not occur.

In recent years, 4D STEM experiments have enabled atomic-scale charge density measurements of thin samples which obey the POA (Section 2.2.4). For example, CoM experiments have been performed using 4D STEM in order to determine the charge redistribution due to bonding in perovskite structures [165]. Due to its enhanced CTF properties versus CoM techniques [207, 233], electron ptychography has been proposed as an alternative technique for the measurement of bonding effects in thin samples. These measurements can provide valuable insights for electronic structure theory calculations. In particular, the experimental measurement of interatomic bonding can be used as a benchmark for density functional algorithms (DFA) which solve for the ground state of many-body systems [24]. Furthermore, the DFAs which most closely match the experimental measurements calculated by ptychography can be used as a basis for microscope simulation packages, most of which currently assume an independent atom model where interatomic bonding is neglected. However, in order to precisely detect the charge redistribution due to bonding in a thin sample, the SNR must be improved by increasing the acquisition time of the 4D STEM data.

As previously discussed in Chapters 2 and 7, the relatively slow frame rates of DEDs ($\sim 10^3$ fps) versus conventional single channel integrating detectors (10^5–10^6 fps) renders 4D STEM acquisition particularly vulnerable to the effects of scan distortions and stage drift. In Chapters 4 and 7, it was discussed how these issues can be partly overcome by acquiring data as quickly as possible, either by applying hardware binning in the detector plane [222], or by lowering the dynamic range of the

detector [244]. However, even for dwell times in the order of 10^{-5} s, these experimental instabilities may still affect the interpretation of ptychographic reconstructions. Furthermore, for the case of detectors whose dynamic range or radiation hardness is too low for acquisition using long exposures, the SNRs of 4D STEM data acquired at speeds of 1,000 fps is somewhat limited. This limitation is particularly disadvantageous to charge redistribution studies which require high lateral precision of atomic columns and high SNRs for the detection of interatomic bonding.

8.1.2 Multi-frame acquisition and registration

One of the most common methods used to compensate for stage drift and scan distortions in STEM is to record multiple consecutive frames of the same region of interest, before applying image registration techniques to align each frame in the series. In fact, multi-frame acquisition is commonly implemented across microscopy [150, 239], medical imaging [245, 246] and photography [247], and can be used to visualise dynamic processes [248, 249] or to obtain a summed-average of a data series for improved SNRs [250–252]. Applying a multi-frame acquisition scheme to 4D STEM data would enable high-SNR ptychographic reconstructions of summed-average data sets which are free from the effects of scan distortions, stage drifts and mechanical and electronic instabilities. This would subsequently increase the precision of the ptychographic phase which is crucial for measuring the effects of bonding in materials.

There are several ways by which artefacts can arise in serial STEM image acquisition. For example, lens current fluctuations and stage drift may manifest as a translation or rotation in sequential frames. In this case, each image can be related to any other image in the series by a *rigid transformation*, i.e. the images are offset by constant vectors, but the distances between the points in each image are preserved.

To compensate for these artefacts, rigid registration (RR) techniques can be used to calculate the offset vectors and subsequently align the image series. RR techniques have been applied with great success to fields such as ultrasound and magnetic resonance imaging [253] and cryo-STEM [254]. However, there also exist artefacts for which RR techniques cannot be used to align an image series. These include scaling offsets due to thermal expansion or lens instabilities, and more commonly, shearing due to stage drift during the STEM scan. In this case, parallelism and the ratios of distances between points are preserved, but the overall distances and angles are not. These global distortions of images can be described by *affine transformations*, and must be corrected for using more advanced registration techniques. For example, the RevSTEM package can perform both rigid and affine registration methods on multi-frame STEM data [239]. By precessing the scan rotation during a STEM image series, the drift vectors can be determined and corrected for using post-processing techniques. However, rigid and affine transformations do not account for all of the geometric distortions that can occur during STEM image acquisition.

There are several instrumental instabilities which give rise to *non-rigid transformations* between consecutive STEM images. These include scan distortions due to fluctuations in the microscope power or water supply, or mechanical vibrations from the surrounding environment, to name a few. In this case, more complex registration methods must be performed in order to correct for these instabilities. Non-rigid registration (NRR) techniques include transformations which can account for the distortions within a data set by moving each pixel by a differing amount. In this way, non-rigid techniques can compensate for both the global and local geometric distortions within a data set. For example, in addition to rigid and affine transformations, the SmartAlign package for STEM and scanning probe data [150] incorporates gradient descent methods, whereby the difference between the gradients of consecutive

images is used to calculate a displacement field between them [255]. The displacement field can subsequently be used to align each data set in the multi-frame series. Multi-frame acquisition and NRR techniques have been frequently applied to STEM imaging modes such as ADF and iDPC imaging [150, 256], as well as spectrum imaging [257–259]. However, to date, the application of these techniques to 4D STEM data has been limited.

8.1.3 Preliminary results and limitations

Multi-frame 4D STEM acquisition has previously been used to increase the SNR of experimental hexagonal boron nitride (hBN) data in order to compare the performance of electronic structure calculations. In this study, two separate algorithms were used to simulate 4D STEM data for a hBN monolayer: the independent atom model (IAM) and density functional theory (DFT). The calculation of structure factors was performed using the CASTEP software package [260], and an in-house code was used to simulate the 4D STEM data (V_{acc} = 80 kV, α = 31 mrad) [261]. The resulting WDD phase reconstructions from the simulated data sets are shown in Figures 8.1(a) and (c), respectively. In addition, the profiles from the blue lines in the phase reconstructions are shown in Figures 8.1(b) and (d)[1]. The atomic species of each phase peak alternates along the line profiles, i.e. N, B, N, B, etc. Unlike the IAM calculation, the DFT calculation accounts for the redistribution of electrons from the boron to the nitrogen atoms. This results in the screening of the potentials of the nitrogen nuclei, leading to a smaller WDD phase difference between the boron and nitrogen atoms than predicted by the IAM.

[1]Strictly, the projected potential of both atomic species should be compared quantitatively by measuring the phase contribution of each atom [24]. This will be discussed in further detail in the following sections. However, for this section, a line profile suffices to demonstrate the potential distribution in hBN.

In order to compare the accuracy of these calculations, sixteen 4D STEM data sets were acquired from a hBN monolayer (V_{acc} = 80 kV, α = 31 mrad) using the JEOL 4DCanvas installed on the ARM200F at the DCCEM. The frame rate used was 4,000 fps, and the cumulative dose for the entire series was 1.24×10^9 e^- nm^{-2}. The summed-average of this series was obtained using the SmartAlign image registration software on the simultaneously acquired ADF images. The determined drift and distortion corrections were then applied to the 4D STEM data series, before performing the WDD reconstruction on the summed-average data set. It should be noted that, if the signal from the ADF image series is poor (i.e. at low electron doses), the ptychographic reconstructions from each data set can be used as the input images to the registration procedure. Figures 8.1(e) and (f) show the aberration-corrected phase reconstruction and an example line profile obtained from the summed-average of the series. Upon observation, there is no noticeable difference in phase between the boron and nitrogen atoms, which suggests that the screening of the nitrogen nuclei has been detected. Further studies have shown that, if the aberrations are sufficiently corrected for using post-processing techniques, the experimental phase distributions of the boron and nitrogen atoms closely match that of DFT calculations [24].

Unfortunately, the multi-frame acquisition and registration method used in the hBN study was limited by the difficulty of acquiring consecutive 4D STEM data sets using the prototype acquisition software. A short time interval was required for the camera software to stabilise between consecutive frames which subsequently lengthened the multi-frame acquisition time. This led to an increase in stage drift and experimental defocus variations during the series which manifest as fluctuations in the ratio of adjacent boron and nitrogen atoms, as shown in Figures 8.1(e) and (f). Throughout my DPhil studies, I worked with the engineers at PNDetector to improve the stability of the camera software, and worked with Dr Lewys Jones to optimise the

image registration technique. In the following section, the application of multi-frame data acquisition and NRR techniques to 4D STEM are further developed from the initial results shown in [24], and the improvement in the precision of ptychographic phase reconstructions is evaluated.

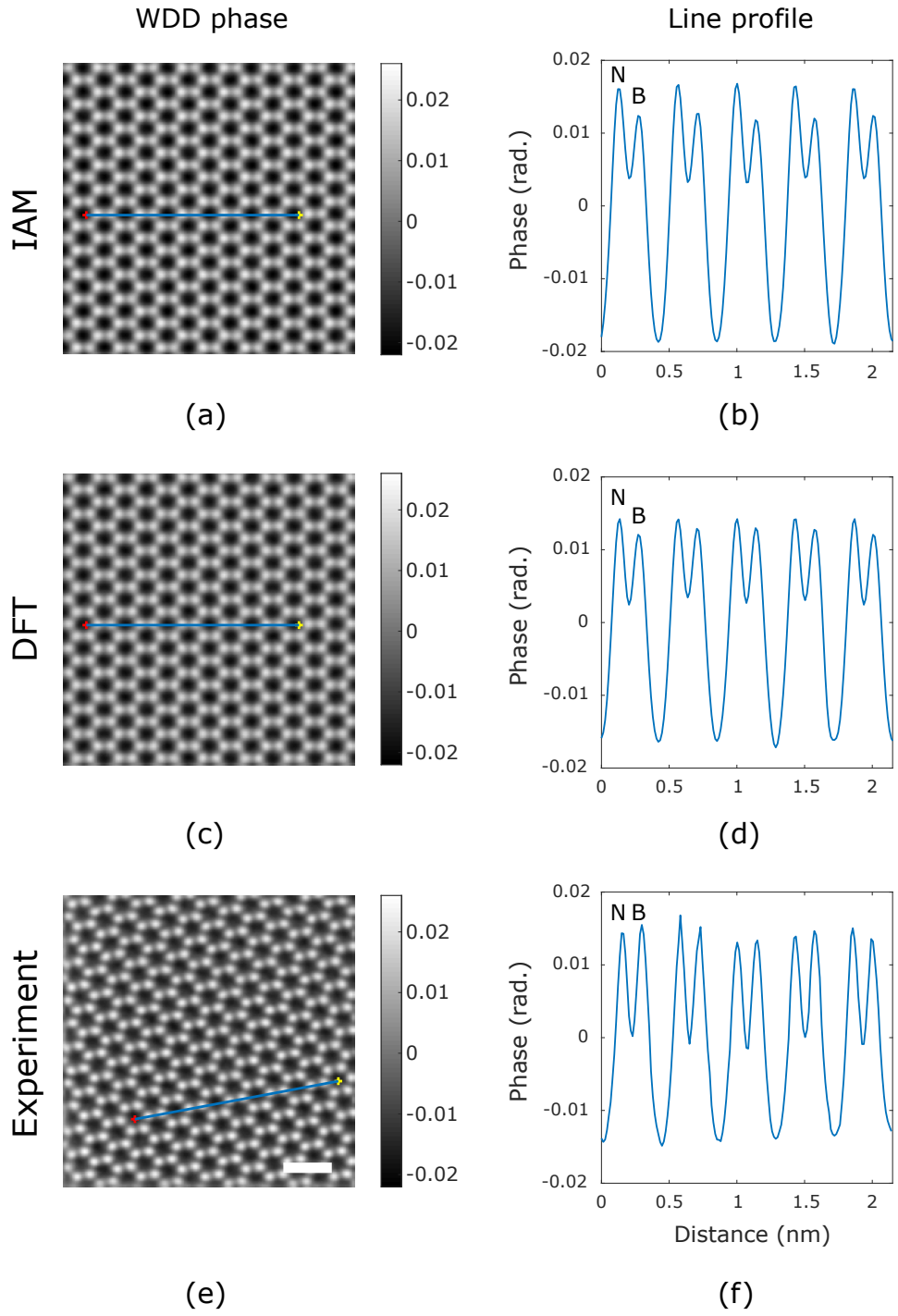

Figure 8.1: WDD phase reconstructions from a hBN monolayer obtained using (a) independent atom model (IAM) simulations, (c) DFT simulations via CASTEP, and (e) experimental data. For sub-figures (a) and (c), propagation of the electron wave to the detector plane was performed using an in-house microscope simulation package [261]. Scale bar: 0.5 nm. Greyscale: phase (radians). The profiles of the blue lines plotted in (a), (c) and (e) are shown in (b), (d) and (f), respectively. The profiles were averaged over a line width of 0.08 nm in the reconstructions. The author is grateful to Dr Laura Clark for providing the code to perform the phase profile analysis.

8.1.4 Procedure

The workflow for the 4D STEM multi-frame acquisition and NRR procedure is shown in Figure 8.2. A total of twenty-one 4D STEM data sets were obtained from a graphene monolayer sample using the ARM200CF and JEOL 4DCanvas at the DC-CEM (V_{acc}= 80 kV, α = 31.5 mrad). Each data set was obtained by acquiring CBED patterns from a scan of 256×256 probe positions. Four-fold detector-binning was applied to increase the acquisition speed to 4,000 fps, resulting in a 256×256×264×66 array for each raw data set. The electron dose for each 4D data set was 5.7×10^7 e^- nm^{-2}, such that the total dose for the multi-frame data was 1.2×10^9 e^- nm^{-2}. For each 4D data set, an image was obtained simultaneously using an ADF detector, an example of which is shown in Figure 8.3(a).

Once acquired, the detector plane of each data set was binned by a factor of four in the orthogonal direction, resulting in a 256×256×66×66 array. Next, the data sets were reshaped from an array of CBED patterns, each recorded at a specific probe position $\mathbf{R_p}$, to an array of 'tilted' STEM images, each corresponding to a single detector pixel at $\mathbf{K_f}$. Both the ADF image series and the reshaped 4D STEM data were imported into Digital Micrograph, after which the SmartAlign plugin was used to perform NRR on the ADF image series. The summed-average of the ADF image series after registration is shown in Figure 8.3(b). The correction vectors determined from this procedure were subsequently applied to all images in the 4D STEM data. It should be noted that it is not necessary to acquire a separate image simultaneously using a different detector: the image registration step may be performed using synthetic images generated from the 4D STEM data. The output of the SmartAlign procedure included individual scan-corrected and registered 4D data sets for imaging dynamic processes, and a multi-frame average (MFA). The registered MFA 4D STEM data set was imported back into MATLAB and re-shaped into an array of CBED pat-

terns such that SSB ptychography could be performed as outlined in Chapter 4.

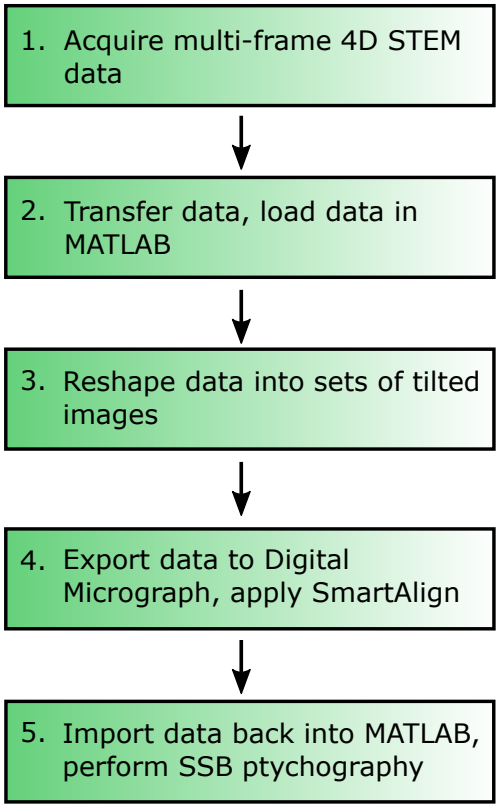

Figure 8.2: Workflow of electron ptychography using multi-frame 4D STEM data.

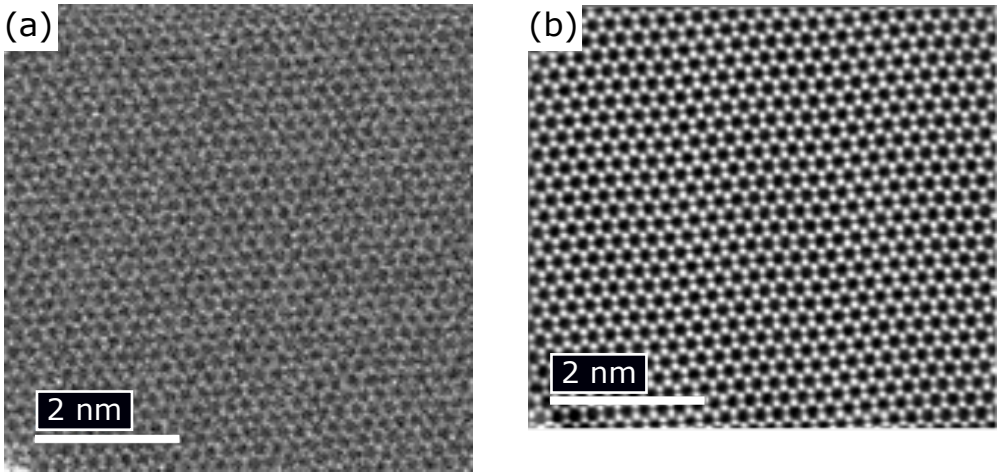

Figure 8.3: (a) Single-frame ADF image from a graphene monolayer series of 21 images. (b) MFA ADF image obtained using non-rigid registration techniques.

8.1.5 Results and discussion

Figure 8.4 shows a comparison of the aberration-corrected SSB phase reconstructions from a single frame (Figure 8.4(a)) and a multi-frame average (MFA) after NRR (Figure 8.4(c)). The increased SNR of the MFA results in a phase reconstruction with higher atomically-resolved contrast and less variation in the phase values at each carbon atom. In addition, the increased SNR of $G(\mathbf{K_f}, \mathbf{Q_p})$, examples of which are shown in the insets to Figures 8.4(a) and (c), allows for a more accurate determination of aberrations via SVD matrix inversion.

To evaluate the performance of ptychography using registered data, the contribution of each carbon atom in the graphene monolayer to the SSB reconstruction was obtained by calculating scattering cross-sections (SCS). This technique is widely used in ADF imaging and spectroscopic mapping, and possesses high sensitivity to atomic species [33, 262, 263]. In ptychography, an SCS can be obtained by calculating the value of squared-phase (in rad^2) for each atom, and normalising to the area (in nm^2) encompassed by the atom in the phase reconstruction. The resulting quantity is known as the integrated squared-phase cross-section (ISPCS), and has units of rad^2 nm^2. The reason for choosing the squared-phase as the metric for cross-section analysis is to compensate for the negative phase dips in the ptychographic reconstruction, as described in Chapters 5 and 6. If an SCS is obtained by integrating the phase over a specific atom and its surrounding vacuum, the negative contribution from the vacuum cancels out the positive contribution from the atomic potential. This results in an SCS value that is close to zero. To combat this issue, the phase reconstruction is squared before the integration step such that both the atoms and the surrounding vacuum regions produce positive peaks. This strategy provides robust measurements for the contribution of each atom to the reconstruction.

In this study, the ISPCS was determined for both a single frame and the MFA. The ISPCS values were calculated using the Absolute Integrator software package [264]. Firstly, a window of fixed area was created around each atom. Subsequently, the squared-phase enclosed in each window was integrated, before multiplying by the area of the window to obtain the ISPCS. The distribution of ISPCS values could then be plotted as a histogram. The ISPCS histogram for the phase reconstructions in Figures 8.4(a) and (c) are shown in Figures 8.4(b) and (d), respectively. A normal distribution was fitted to the histograms, and the mean and standard deviation were calculated in each case. Comparison of the two data sets shows that the mean ISPCS for a single frame and the MFA are similar (3.0×10^{-3} rad^2 nm^2 versus 2.7×10^{-3} rad^2 nm^2). The slight difference between these values is still under investigation, but it is likely a result of the inaccurate calculation of residual aberrations using a single frame. Furthermore, the standard deviation of the ISPCS for the single frame and MFA are 7.6×10^{-4} rad^2 nm^2 and 2.3×10^{-4} rad^2 nm^2, respectively. This demonstrates that the application of multi-frame acquisition and NRR increased the ISPCS precision by almost a factor of three versus single frame acquisition. This is lower than the expected factor of improvement in SNR ($\sqrt{21}$), and is most likely due to the limited speeds of 4D STEM acquisition. Nevertheless, this improvement will prove particularly useful for detecting the interatomic bonding in nanomaterials such as hBN which is often obscured by statistical noise in single frame acquisitions [24, 142, 165]. Furthermore, the combination of ultrafast DEDs for 4D STEM applications [159] and NRR techniques should enable ptychographic studies of atom dynamics in the near future.

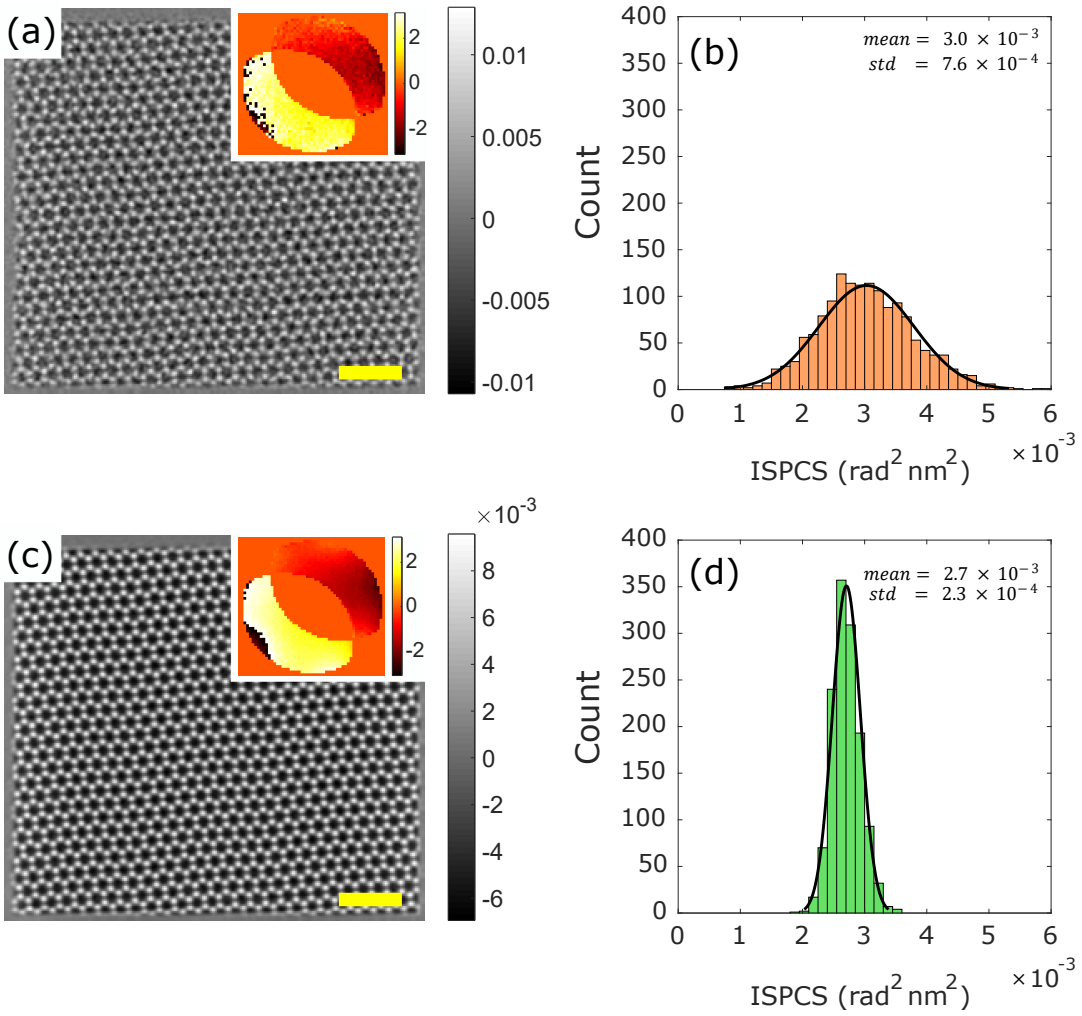

Figure 8.4: (a) Electron ptychography performed on multi-frame data acquired from a graphene monolayer. (a) SSB phase reconstruction of a single frame. Scale bar: 1 nm. Greyscale: phase (radians). (b) Integrated squared-phase cross-section (ISPCS) for the reconstruction shown in (a). (c) SSB phase reconstruction using the summed-average of the NRR data as the input 4D STEM data. Scale bar: 1 nm. Greyscale: phase (radians). (d) ISPCS for the reconstruction shown in (c). The insets to (a) and (c) display values of the phase of $G(\mathbf{K_f}, \mathbf{Q_p})$ for Q_p =21 mrad. Colour bar: phase (radians).

8.2 Depth sectioning of defects at the single-atom level

The author is grateful to 1) Dr Gerardo Martinez for contributing to the data acquisition, 2) Dr Rebecca Nicholls for performing the DFT relaxation calculations discussed in this section, and 3) the experimental support team at ePSIC.

8.2.1 Introduction

The capabilities of modern HRTEM and STEM instruments have enabled routine atomic-resolution imaging in two real-space dimensions[2]. However, the application of STEM techniques to three real-space dimensions has been a challenge. Single particle cryo-electron microscopy has proven to be extremely successful for biological structure determination at near-atomic resolution [265, 266]. However, this technique performs averaging over many individual particles to increase the SNR, which requires the assumption that all structures are identical. Another candidate technique for three-dimensional TEM imaging is atomic electron tomography (AET). This involves the acquisition of an image series from a sample using a wide range of tilt orientations, combined with computational techniques to reconstruct the sample in three dimensions. This technique is not dependent on particle averaging for increased SNR, and has enabled the characterisation of both ordered and disordered materials systems (for a review, see [267]). Unfortunately, the high dose required for atomic-resolution tomographic reconstruction renders AET impractical for beam-sensitive materials.

An alternative method of imaging in three dimensions using electron microscopy is by performing ADF optical sectioning. This technique utilises the depth of focus

[2]The term 'real-space dimensions' has been used throughout this section to avoid confusion with the four-dimensions of 4D STEM (two real-space dimensions and two reciprocal-space dimensions).

(i.e. the depth range for which the image is in focus) of STEM calculated by:

$$\Delta z = \frac{1.77\lambda}{\alpha^2} \tag{8.1}$$

where Δz is the full width at half maximum (FWHM) of the probe intensity distribution in the z-direction, λ is the electron wavelength and α is the probe convergence semi-angle [33, 268]. If Δz is smaller than the sample thickness, which often is the case for an aberration-corrected STEM probe using a large convergence semi-angle α, regions within the range of Δz are transferred with high contrast to the image plane while sample information at other depths is effectively rejected [33, 269]. Atomic-resolution ADF optical sectioning has been used to locate the depth of single atoms inside semiconductor devices [270], and to characterise screw dislocations in GaN [271]. Experimentally, ADF optical sectioning is performed by acquiring a series of ADF images at sequential values of defocus, using a large convergence semi-angle and high acceleration voltage such that Δz is only a few nanometres. For reference, if $\alpha = 30$ mrad and an acceleration voltage of 300 kV ($\lambda = 1.97$ nm) is used, $\Delta z = 3.9$ nm. However, because ADF imaging is not a dose-efficient technique and provides poor contrast of light atoms, ADF optical sectioning is primarily applicable to heavy-element, beam resilient samples.

Optical sectioning with a STEM instrument can also be performed using electron ptychography. The unique advantage of ptychographic optical sectioning is that it can be performed *using a single data set* – it is not necessary to acquire an experimental image series. The ptychographic phase can be reconstructed at different depths of the sample using post-processing techniques. This can be explained by considering $G(\mathbf{K_f}, \mathbf{Q_p})$ at a specific spatial frequency $\mathbf{Q_p}$. If the region of a sample is out of focus such that there is a phase ramp across $\mathbf{Q_p}$, the sum of the phase across the DO

region is diminished and the spatial frequency is transferred with little or no contrast to the phase reconstruction. Conversely, in-plane sample regions are transferred with high contrast to the image plane. Optical sectioning can be performed using SSB ptychography by synthesising aperture functions with an additional defocus term and adjusting $G(\mathbf{K_f}, \mathbf{Q_p})$ accordingly, or via WDD ptychography by deconvolving $H(\mathbf{r}, \mathbf{Q_p})$ using defocused probe functions. In recent years, ptychography has been used to perform optical sectioning of carbon nanotubes using both WDD and ePIE methods [18, 205], but ptychographic optical sectioning at smaller length scales has not yet been reported. Here, initial results will be presented for SSB ptychographic optical sectioning of a graphene defect which has not previously been observed.

8.2.2 Experimental method and results

A 4D STEM data set containing 256×256 probe positions was obtained from a graphene monolayer using the JEM ARM300F and MerlinEM system at ePSIC (V_{acc} = 80 kV, α = 31 mrad) at a frame rate of 1,000 fps[3]. The cumulative dose for the data set was 7.7×10^7 e$^-$ nm^{-2}. Following data acquisition, the SSB reconstruction algorithm was performed as described in Chapters 3 and 4. The residual aberrations were determined using SVD matrix inversion (Appendix B) and corrected prior to reconstruction, and noise normalisation was applied to increase the phase contrast from low and high spatial frequencies (Chapter 6). The aberration-corrected SSB phase reconstruction is shown in Figure 8.5. Following reconstruction, an unknown graphene defect was observed, highlighted with a yellow square in Figure 8.5(a) and magnified in Figure 8.5(b). The 6-7-6 ring defect contains one atom, 'Atom X' (marked by

[3]It should be noted that, because this data was initially obtained as part of an experiment which had different objectives, the choice of sample and experimental settings was not ideal for optical sectioning of single atoms. For example, a higher acceleration voltage would have decreased λ and subsequently decreased Δz. Furthermore, the knock-on damage of monolayer graphene is particularly damaging at higher electron voltages. Nevertheless, optical sectioning was performed in order to understand an unexpected atomic defect in the data.

the orange arrow in Figure 8.5(b)), with relatively diminished phase-contrast when compared with its neighbouring atoms.

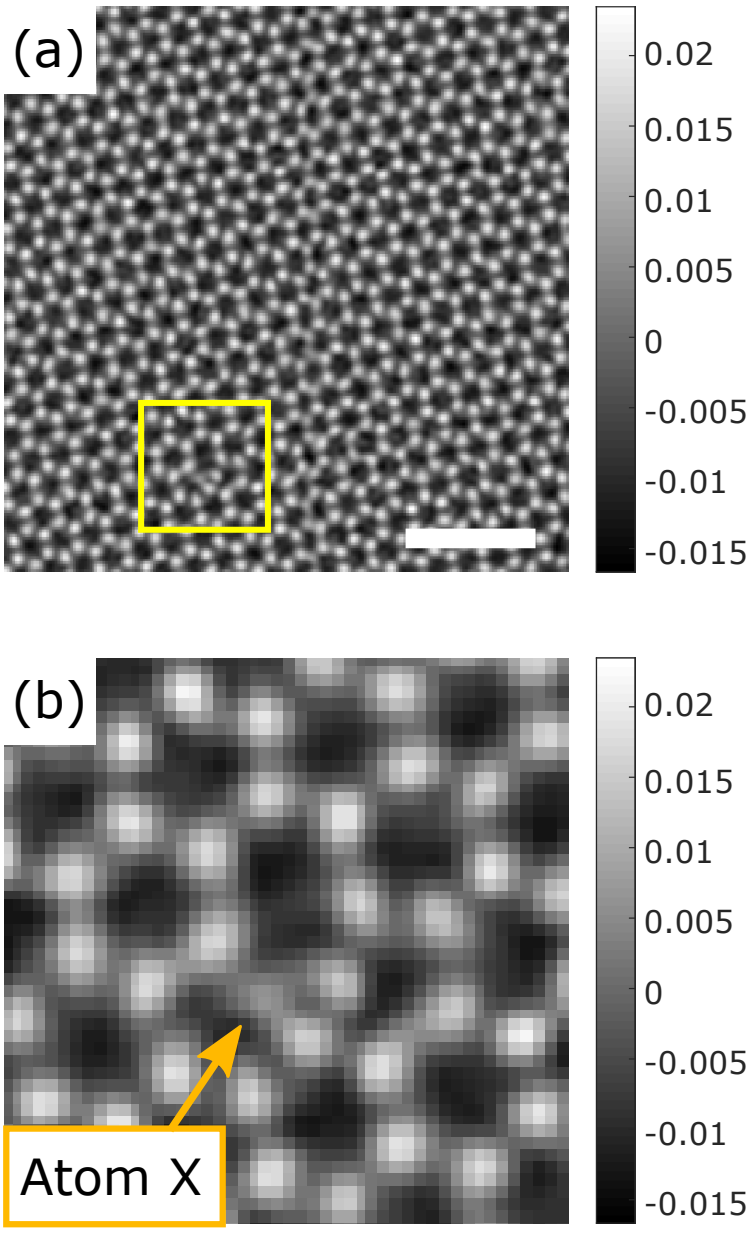

Figure 8.5: (a) Noise-normalised SSB reconstruction of monolayer graphene containing a 6-7-6 ring defect, marked by a yellow square, which has not previously been observed. Scale bar: 1 nm. The 1 nm × 1 nm region enclosed in the yellow square is shown in (b). An atom with diminished contrast was observed ('Atom X'), the location of which is identified by the orange arrow. Greyscale: phase (radians).

The atomic species or depth location of Atom X cannot be directly determined from the reconstruction shown in Figure 8.5. In an attempt to determine its location along the z-direction, SSB optical sectioning was performed. Using the same method as for correcting aberrations (Section 4.4.8), a defocus term $C_{1,0}$ was applied to the aberration function in order to reconstruct the phase information from a specific depth within the sample. This was performed for 0.1 nm steps in a defocus range of 20 nm centred about the point of experimental (pre-correction) focus. Following ptychographic optical sectioning, the ISPCS values (see Section 8.1.5) were determined for each carbon atom in the monolayer, at each defocus step. The ISPCS values for Atom X and its two nearest-neighbours were plotted as a function of depth, as shown in Figure 8.6(a), in order to determine the depth at which the ISPCS is a maximum and hence the relative depth location of each atom. The value of zero defocus was shifted to the $C_{1,0}$ value determined in the initial aberration correction step (-0.15 nm). The atoms plotted in Figure 8.6(a) are labelled in the phase reconstruction shown in Figure 8.6(b). The maximum ISPCS of Atom X (blue) was calculated to be 0.1 nm above its two nearest neighbours (black and red). This experimental result is currently being compared to DFT relaxation calculations in order to characterise the atomic species of Atom X and determine the bond lengths between the three atoms in the defect system. Preliminary results suggest that Atom X is a carbon atom which is bonded to either one or two hydrogen atoms. This would explain the diminished contrast of Atom X in the SSB phase reconstruction, as the hydrogen atoms would transfer their electrons to Atom X and hence screen its nuclear potential.

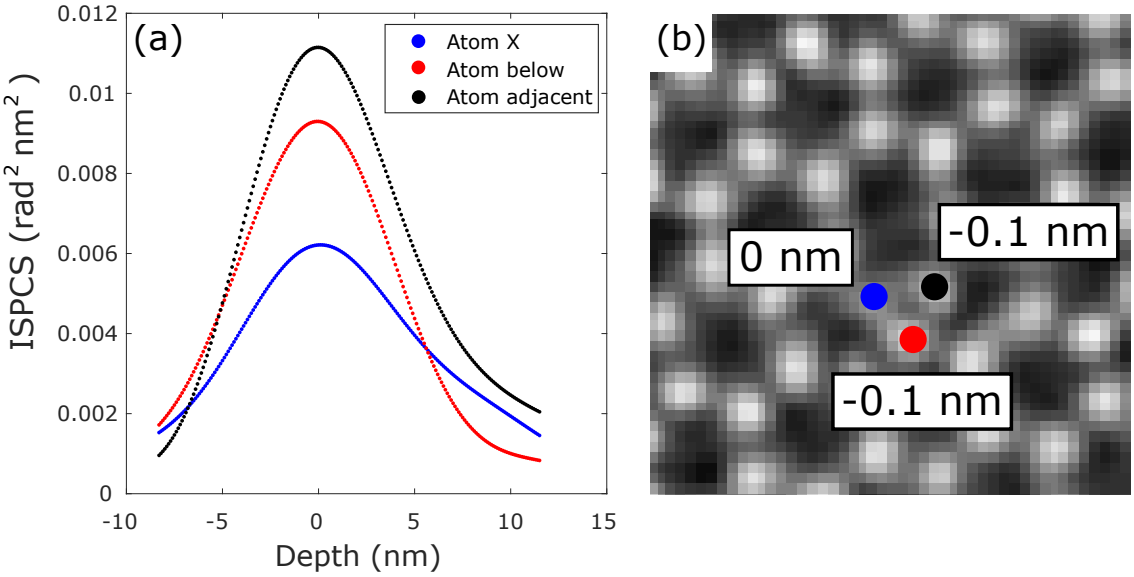

Figure 8.6: (a) ISPCS vs depth for the three atoms in the graphene defect system. The x-y positions and calculated depth locations of the atoms plotted in (a) are labelled in the SSB phase image shown in (b).

Although the relative depths of the defect atoms were within the order of magnitude expected, a number of experimental issues were encountered. Firstly, the experimental conditions were not optimised for atomic-scale optical sectioning. For example, $\Delta z = 8$ nm for this experiment. The use of a higher acceleration voltage and a larger probe convergence semi-angle in a future experiment would decrease Δz by a factor of 2–3 and subsequently increase the accuracy of ptychographic depth sectioning. An improved depth sectioning experiment could be performed in order to determine the amplitude of ripples in transition metal dichalcogenides such as molybdenum disulfide (MoS_2) and tungsten diselenide (WSe_2). Secondly, the accurate determination of residual aberrations is crucial for determining the correct depths of atoms in a material. In the experiments shown in Section 8.2.2, a lateral shift in the position of the atomic columns was observed with varying levels of defocus. This subsequently affects the ISPCS values recorded at each Voronoi cell for each depth in the series. To compensate for this, the aberration correction procedure described in Appendix B should be further developed to account for aberrations up to

5^{th} order. Alternatively, an inverse multislice procedure could be performed using the ePIE method, but this would need to be equally robust to residual aberrations. Once the post-processing procedures have been further developed, this experimental data should be revisited in order to characterise the graphene defect more rigorously and subsequently provide valuable insights into the electronic and structural properties of graphene.

8.3 Simultaneous light- and heavy-element imaging of Uranium dioxide

The author is grateful to Dr Ed Darnbrough (ED) and Dr Ian Griffiths (IG) for their contributions to the work presented in this section. ED prepared the sample and assisted with data acquisition. IG aligned the microscope and acquired some of the ptychographic data during the experimental session. I acquired some of the ptychographic data during the experimental session and performed the ptychographic analysis.

8.3.1 Motivation

The ability to image light elements in a heavy-element matrix using FPP has provided atomic-scale structural characterisation of energy materials, such as boron-doped catalyst nanoparticles [20] and lithium manganese oxide cathodes [17]. In this section, the application of ptychography to another energy material, uranium dioxide, will be described.

Uranium dioxide (UO_2) is a ceramic commonly used for nuclear fuel pellets in light water reactors (LWRs) [272, 273]. However, high-energy fission particles can degrade UO_2 over time. Atomic vacancies and interstitials can accumulate to form nano-voids and dislocation loops respectively [274, 275], which reduce thermal conductivity and cause swelling of the pellets. A reduction in thermal conductivity not only decreases the efficiency of the fuel pellets, but also leads to temperature gradients across the fuel rod which can prove hazardous in the case of insufficient cooling, e.g. the Fukushima Daiichi disaster [276]. Furthermore, insufficient containment of swollen UO_2 fuel pellets can cause contamination of the coolant liquid [277]. As a result, it is often necessary to replace UO_2 fuel pellets: a major operational cost of LWRs [275].

The study of irradiated UO_2 can give insights into the optimal turnover rate of nuclear fuel rods required to operate LWRs both safely and efficiently. Although dislocation loops and nano-voids have been imaged in irradiated UO_2 at the nanoscale using in-situ CTEM [275, 278], the atomic processes that give rise to these features [274] have not yet been experimentally visualised. In the following subsections, initial results of the application of atomic-resolution electron ptychography to a UO_2 sample will be presented.

8.3.2 Method

A 4D STEM data set was obtained for a FIB lamella of UO_2 in the [100] direction, using the JEOL 4DCanvas installed on the ARM200CF at the DCCEM (V_{acc}= 200 kV, $\alpha = 22.5$ mrad). The data was acquired at 4,000 fps using four-fold detector-binning as described in Section 8.1.4. An example CBED pattern from the 4D STEM data set is shown in Figure 8.7(a). In contrast to the graphene CBED patterns displayed in Figure 3.1, a significant proportion of the electrons are scattered to angles greater than the radius of the BF disc. An ADF image was obtained simultaneously with the 4D STEM data acquisition using a separate ADF detector. The cumulative dose was estimated to be 8.3×10^7 e^- nm^{-2}.

The imaging of oxygen atomic columns in the presence of uranium atomic columns is practically impossible using ADF STEM. This is partly due to electron channelling: the deep potential of the uranium columns attracts electrons that are incident over oxygen columns, creating a large background which masks the signal of the oxygen [279]. Furthermore, assuming a typical HAADF imaging geometry where contrast is proportional to $Z^{1.7}$ [60], the U:O image intensity ratio would be 63.56:1, providing little or no contrast at the positions of the oxygen columns. The ADF image obtained

for UO_2 parallel to 4D data acquisition is shown in Figure 8.7(b). The ADF inner collection angle was 50.39±1.29 mrad ($\sim 2\alpha$), such that a MAADF image is obtained (Section 2.3.3). Although acquired using a scanning speed (electron dose) twenty times longer (larger) than for standard ADF imaging speeds, the MAADF image still provides negligible contrast at the oxygen columns.

8.3.3 Results

Ptychographic reconstruction was performed on the 4D STEM data from the UO_2 sample using the WDD method (even single uranium atoms are not WPOs, so the SSB method was not applied). Reconstruction of the specimen transmission function *without* correction of residual aberrations gives the phase shown in Figure 8.7(c). The effects of residual aberrations can be seen by inspecting the phase of $G(\mathbf{K_f}, \mathbf{Q_p})$ at specific spatial frequencies, an example of which is shown in the inset to Figure 8.7(c). Although this phase reconstruction provides finer structural details than the MAADF image shown in Figure 8.7(b), the residual aberrations prevent identification of the oxygen atomic columns. Applying post-processing aberration correction using SVD matrix inversion (Appendix B) yields the phase reconstruction shown in Figure 8.7(d). The example plot of $G(\mathbf{K_f}, \mathbf{Q_p})$ shows a more homogeneous phase surface following correction of the residual aberrations. As a result, both the uranium columns and the oxygen columns are now visible in the phase reconstruction. Furthermore, the ptychographic reconstruction enables the visualisation of oxygen vacancies in UO_2, two of which are marked with orange arrows in Figure 8.7(e), and with green circles in Figure 8.7(f). This is the first experiment to have demonstrated the visualisation of oxygen vacancies in UO_2. However, improved experiments and post-processing methods are needed in order to provide quantitative analysis of the oxygen vacancies. For example, the carbon contamination present on the sample and in the surrounding vacuum complicate the interpretation of phase measurements from atomic columns.

Furthermore, the number of vacancies in the direction of the electron beam could not be deduced from the analysis shown in this section. Future ptychographic reconstructions of vacancies in UO_2 should be compared to reconstructions from simulated data sets, in order to determine the number of vacancies present in each atomic column.

The application of ptychography to UO_2 has demonstrated two advantages of the technique versus conventional STEM imaging modalities. Firstly, atomically resolved contrast of light-element columns in the presence of heavy-element columns is readily achievable. Secondly, the correction of residual aberrations in post-processing allows for higher throughput atomic-resolution microscopy. Electron ptychography studies of UO_2 have the potential to bridge the 'knowledge gap' between 1) the theoretical calculations of single-atom defects and vacancies [274], and 2) the experimental studies of dislocations and voids which, before now, have only been observed on the nanoscale [275]. Furthermore, ptychographic reconstructions performed over larger fields of view (i.e. >100 nm) would provide a statistical representation of the number of vacancies in the oxygen lattice, from which the decrease in thermal conductivity could be deduced [280]. This analysis could be applied to a series of UO_2 samples which have been exposed to differing levels of fission products in order to track the thermal conductivity and estimate the optimal lifetime of UO_2 fuel pellets.

8.4 Discussion

The applications of electron ptychography presented in this chapter have demonstrated the versatility of the technique. The combination of high phase sensitivity and robustness to dynamical effects versus other exit-wave reconstruction methods enables atomic-resolution imaging of both light and heavy elements. To further increase the phase sensitivity, ptychography can be performed in combination with multi-frame

acquisition and data registration methods. Furthermore, three-dimensional profiles of thin samples can be extracted from a single data set – there is no need to acquire a data series using multiple sample tilts. It is anticipated that further novel capabilities of ptychography will be discovered in future work, and it is hoped that these capabilities will be used for the characterisation of many challenging materials.

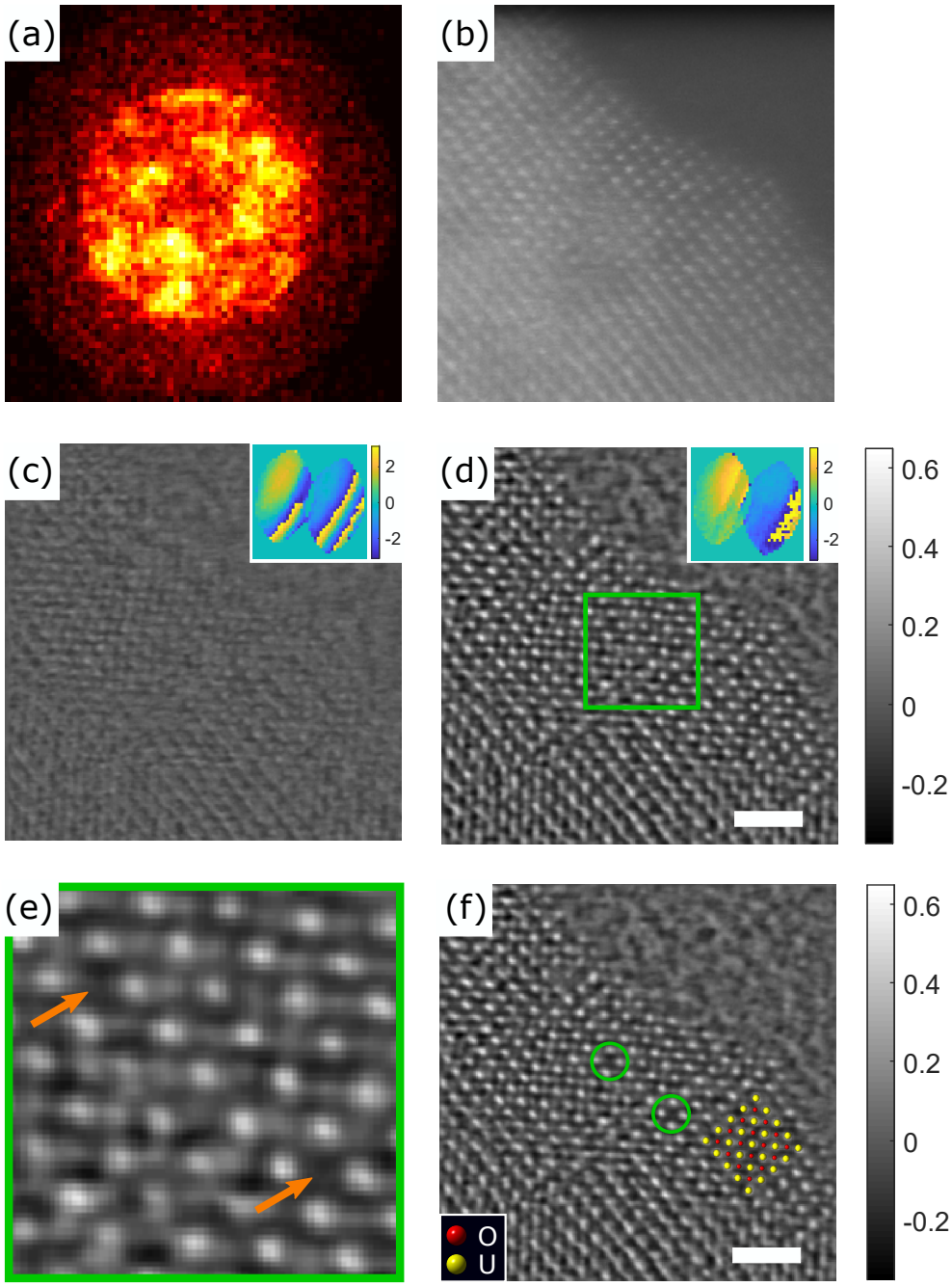

Figure 8.7: (a) Example CBED pattern, (b) ADF image (c) raw WDD reconstruction and (d) aberration-corrected WDD reconstruction for UO_2[100]. The insets to (c) and (d) display example values of the phase of $G(\mathbf{K_f}, \mathbf{Q_p})$ for Q_p =21 mrad. Colour bars for inset figures: phase (radians). The green square in (d) is magnified in (e), where the orange arrows point to the locations of two vacancies. Sub-figure (f) displays the same reconstruction as shown in (d), but includes an overlay of the crystal structure and the locations of the vacancies shown in (e) (marked with green circles). Scale bar: 2 nm. Greyscale for (c)–(f): phase (radians).

Chapter 9

Conclusions

The combination of direct electron detectors (DEDs) and electron ptychography has enabled atomic-resolution, high-sensitivity, robust phase reconstructions for a variety of challenging materials. However, several experimental and analytical limitations remain, namely the relatively slow detector speeds for scanning applications, and the limited bandwidth of the phase-contrast transfer function (PCTF). The new science presented in this thesis demonstrates how these limitations can be somewhat overcome via careful consideration of detector settings, experimental configurations and statistical noise.

In Chapter 5, the contrast transfer properties of focused-probe ptychography were examined to demonstrate the importance of choosing suitable experimental parameters for optimising dose-efficiency. It was experimentally demonstrated that, unlike for HRTEM imaging, there are no contrast reversals in the PCTF of SSB ptychography. As a result, the interpretation of high-resolution information is straightforward, and does not require serial image acquisition such as in HRTEM. Furthermore, by choosing an optimal probe convergence semi-angle, the electron dose needed to produce high SNR ptychographic reconstructions is minimised.

In Chapter 6, a model for the statistical noise present in $G(\mathbf{K_f}, \mathbf{Q_p})$ was developed in order to understand the noise suppression process of SSB ptychography. Using this model, the PCTF for SSB ptychography was adjusted to boost the signal of low and high spatial frequencies in the ptychographic reconstruction, while avoiding noise amplification. This strategy further reduces the electron dose needed to obtain phase reconstructions with a reasonable SNR.

In Chapter 7, the limitation of slow scan speeds in STEM using DEDs was relaxed by acquiring data using a 1-bit counting mode. This strategy enabled a MerlinEM DED to achieve maximum detector speeds of 12,500 fps, and subsequently reduced the minimum practical usable dose of a ptychographic experiment. Atomic-resolution phase reconstructions were obtained from a zeolite sample (ZSM-5) using 1-bit data at electron doses as low as 2.0×10^4 e^- nm^{-2}, demonstrating the application of ptychography to beam-sensitive materials at the atomic scale. Low-dose electron ptychography is particularly important for imaging energy materials whose properties often change when exposed to a high electron flux. By reducing the electron flux incident on the sample, energy materials can be imaged without damage or transformation.

It is anticipated that the new science presented in Chapters 5–7 will lead to an increase in usage and throughput of electron ptychography techniques throughout the microscopy community. The lower dose capabilities resulting from the developments presented in this thesis will enable a larger range of beam-sensitive materials to be imaged using electron ptychography.

In Chapter 8, electron ptychography was used to overcome a number of limitations of conventional STEM imaging techniques. Firstly, it was demonstrated how

multi-frame data acquisition can increase the precision of atomic-resolution phase reconstructions and compensate for the effects of scan distortions. For a very thin sample, the phase is directly proportional to the projected potential. Therefore, the potential distribution within a nanomaterial can be accurately determined. This capability is particularly useful for comparing the performance of density functional approximations which aim to computationally calculate the charge distribution of atoms in a materials system [24]. Furthermore, the correction of scan distortions increases the positional accuracy of atomic columns. Combining scan correction with high sensitivity ptychographic phase reconstruction should enable routine atomic-resolution, high-precision strain mapping of light-element crystalline samples.

Secondly, initial results of ptychographic depth sectioning at the atomic scale were presented for a previously unknown graphene defect. Three-dimensional TEM is typically performed by acquiring multiple data sets at various sample tilt orientations followed by computational reconstruction (e.g. cryo-electron microscopy and atomic electron ptychography), or by acquiring a series of ADF images at a range of experimental defocus levels (ADF optical sectioning). In contrast, ptychographic optical sectioning can be performed using a single data set. By applying a range of defocus values to the wave aberration function via post-processing techniques, the complex transmission function could be calculated for a series of depths within a graphene monolayer sample. The ability to image a material in three dimensions using a single ptychographic data set simplifies the experimental method, reduces the electron dose and increases the throughput of three-dimensional electron microscopy. Further development of the technique is required to increase the precision of the depth sectioning process.

Finally, electron ptychography was applied to uranium dioxide (UO_2): a material commonly used as nuclear fuel pellets for light water reactors (LWRs). The UO_2 pellets degrade over time due to high-energy fission particles which create vacancies, dislocations and nano-voids in the material. In order to visualise degradation of the oxygen lattice in UO_2, the oxygen columns must be imaged with sufficient contrast. For conventional STEM imaging techniques, the oxygen signal is masked by the deep potential of the uranium atomic columns, such that the contrast of the oxygen columns is negligible. The application of WDD ptychography to an UO_2 sample enabled the visualisation of oxygen columns in the presence of the significantly heavier uranium columns. Furthermore, vacancies in the oxygen lattice were visualised in UO_2 for the first time. Atomic vacancies in UO_2 can accumulate to create nano-voids in the material which subsequently decrease the thermal conductivity of the fuel pellets. Further application of ptychography to degraded UO_2 samples could provide a statistical representation of the percentage of vacancies in the nuclear fuel pellets used in LWRs, and subsequently estimate the optimal lifetime of UO_2 fuel pellets.

9.1 Future work

Light- and heavy-element imaging of beam-sensitive energy materials

There is a plethora of materials science problems that would benefit from the application of electron ptychography, particularly in studies of materials whose constituent elements possess a wide range of atomic numbers. Light-heavy element materials are common in battery science and catalysis, for which ptychography has provided atomic-resolution structural information [17, 20]. However, some energy materials are much more sensitive to the electron beam, including zeolites [236, 237] and hybrid organic-inorganic perovskites [3, 4]. The implementation of 1-bit data acquisition and

noise normalisation should decrease the dose requirements of ptychography such that some of these beam-sensitive materials can be imaged without damage.

Simultaneous ptychography, incoherent imaging and spectroscopy

The acquisition of 4D STEM data can be performed simultaneously with incoherent imaging and EDX spectroscopy to provide comprehensive characterisation of a materials system. However, EDX spectroscopy requires large electron doses and heavy-element samples to provide signal above the detector noise level. The dose-efficiency of EELS detection is significantly larger than that for EDX detection and as such, spectroscopy of light elements is more readily achievable. Unfortunately, the simultaneous acquisition of EELS spectra and 4D STEM data is not possible because the associated detectors are both located on the optic axis of the microscope column. The development of annular pixellated detectors would allow for simultaneous ADF, EDX, EELS and 4D STEM data acquisition, and a recent proof-of-concept study has demonstrated that atomic-resolution ptychographic reconstruction can be performed using data from such a hypothetical detector [281]. The practical implementation of this acquisition strategy would enable the structural and compositional characterisation of both light and heavy atomic columns in a material.

Organic materials

Organic materials such as polymers and biological structures are extremely sensitive to the electron beam. In this case, additional techniques may be implemented into ptychographic algorithms to avoid electron-induced damage to the material. For example, cryogenic sample grid preparation [211] and non-convex Bayesian optimisation [16] have been combined with ptychography to enable high contrast phase reconstructions of biological structures at low dose. Compressed sensing is another dose-reduction technique, which involves the application of algorithms to reconstruct

signals from underdetermined systems. For example, in the case of STEM imaging, compressed sensing can be applied to reconstruct an image of a 2D region of interest using a sub-sampled probe scan array. Compressed sensing has already been applied to STEM data which has been acquired using a sub-sampled randomised scan [282]. Furthermore, compressed sensing techniques have enabled atomic-resolution ptychographic reconstruction of a perovskite using 1% of the data acquired from an experimental 4D STEM scan [283]. However, in order to decrease the experimental electron dose incident on a material, 4D STEM data should be acquired using a sub-sampled randomised scan in future experiments.

Ultra-fast data acquisition and ptychography

The robustness of ptychography to stage drift and scan distortions is expected to improve with the development of faster detectors. State-of-the-art, ultra-fast pixellated detectors, such as the '4D Camera' at Lawrence Berkeley National Laboratory, can acquire 4D STEM data at speeds of up to 87,000 fps [159]. This allows ptychographic data sets to be obtained with dwell times as fast as the conventional non-pixellated STEM detectors used in BF and ADF acquisition. Ultra-fast data acquisition may further be combined with non-rigid registration techniques [150, 239] in order to visualise dynamic processes [249] of light-elements and beam-sensitive materials, such as defect evolution in graphene and degradation of lithium cathode materials.

Ptychographic atomic electron tomography

In Chapter 8, it was demonstrated that three-dimensional information can be obtained using relatively low electron dose by performing ptychographic depth sectioning on a single 4D STEM data set. However, the precision of this technique is inferior to that of atomic electron tomography (AET), which typically involves ADF STEM acquisition at multiple sample tilt orientations and thus uses a much higher elec-

tron dose than ptychography. The combination of electron ptychography and AET may enable atomic-resolution 3D reconstructions using much fewer projections than typically needed for AET. In addition, the phase-sensitivity of electron ptychography should significantly improve the contrast of light-element columns and beam-sensitive materials in tomographic reconstructions. Ptychographic tomography would be particularly valuable for characterising the three-dimensional structure of materials for efficient and renewable energy applications, such as lithium cathode materials, zeolite catalysts and solar cell perovskites. The insights gained from such studies will hopefully contribute to alleviating, or even solving, the global energy/entropy crisis.

Appendix A

Glossary of terms

(A)BF	(annular) bright-field
(A)DF	(annular) dark-field
CBED	convergent beam electron diffraction
CDI	coherent diffraction imaging
(C)FEG	(cold) field-emission gun
CTEM	conventional transmission electron microscopy
DED	direct electron detector
DO	double overlap
DPP	defocused-probe ptychography
EDXS	energy-dispersive X-ray spectroscopy
EELS	electron energy-loss spectroscopy
ePIE	extended ptychographical iterative engine

FCNT	functionalised carbon nanotube
FEM	fluctuation electron microscopy
FPP	focused-probe ptychography
HRTEM	high-resolution transmission electron microscopy
(i)CoM	(integrated) centre-of-mass
(i)DPC	(integrated) differential phase-contrast
ISPCS	integrated squared-phase cross-section
(M)APS	(monolithic) active pixel sensor
MFA	multi-frame average
PAD	pixel array detector
(P)CTF	(phase-) contrast transfer function
RDF	radial distribution function
SA(E)D	selected-area (electron) diffraction
SNR	signal-to-noise ratio
SSB	single side-band
STEM	scanning transmission electron microscopy
TEM	transmission electron microscopy
TO	triple overlap
WDD	Wigner distribution deconvolution
(W)PO(A)	(weak-)phase-object (approximation)

Appendix B

Post-processing aberration correction

In this section, the theory and methodology for the post-processing aberration correction procedure used in FPP will be described. Firstly, the technique of singular value decomposition (SVD) matrix inversion will be briefly explained. Subsequently, the procedure for preparing a set of linear equations from Equation (3.25) will be demonstrated. Finally, the aberration correction procedure performed throughout this thesis will be outlined.

B.1 SVD matrix inversion

The singular value decomposition (SVD) is the decomposition of any rectangular matrix, in this case Y, into two unitary matrices and one diagonal rectangular matrix

$$Y = U\Xi V^T \tag{B.1}$$

where U and V are the unitary matrices and Ξ is the diagonal matrix of singular values[1]. The superscript T denotes the transpose. The matrices U and V can be determined by calculating the eigenvectors YY^T and Y^TY respectively, while the eigenvalues allow for the solution of Ξ. The singular values in Ξ are typically arranged in descending order, such that the matrix Y can be closely approximated by using only the first few singular values on the right-hand side of Equation (B.1). Applications of SVD include image compression [284], facial recognition [285] and de-noising of spectroscopic signals [286]. Furthermore, SVD can be used obtain the pseudoinverse of ill-conditioned matrices that are not invertible. Substituting Equation (B.1) into $Y\mathbf{x} = \mathbf{b}$:

$$U\,\Xi\,V^T\,\mathbf{x} = \mathbf{b} \tag{B.2}$$

Multiplying both sides by $V\Xi^{-1}U^T$:

$$V\,\Xi^{-1}\,U^T\,U\,\Xi\,V^T\,\mathbf{x} = V\,\Xi^{-1}\,U^T\,\mathbf{b}$$

$$V\,\Xi^{-1}\,\Xi\,V^T\,\mathbf{x} = V\,\Xi^{-1}\,U^T\,\mathbf{b}$$

$$V\,V^T\,\mathbf{x} = V\,\Xi^{-1}\,U^T\,\mathbf{b}$$

$$\mathbf{x} = V\,\Xi^{-1}\,U^T\,\mathbf{b} \tag{B.3}$$

[1]For clarity, the symbol Ξ has been used instead of the conventional notation Σ.

where $V\,\Xi^{-1}\,U^T$ is the pseudoinverse of the matrix Y. Thus, if $\mathbf{b}$ and Y are both known and $Y\mathbf{x} = \mathbf{b}$ is an overdetermined system, one can solve for $\mathbf{x}$.

B.2 Preparing the linear equations

As previously shown in Equation (3.25) of the main text, under the WPOA, the phase of $G(\mathbf{K_f}, \mathbf{Q_p})$ for the $-\mathbf{Q_p}$ side-band can be expressed as

$$\angle G_{-\mathbf{Q_p}}(\mathbf{K_f}, \mathbf{Q_p}) = \chi(\mathbf{K_f}) - \chi(\mathbf{K_f} + \mathbf{Q_p}) - \angle\Psi'(-\mathbf{Q_p}) \tag{B.4}$$

The term $\Psi'(-\mathbf{Q_p})$ is the scattered component of the Fourier transmission function, while $\chi(\mathbf{K_f})$ is the aberration function with respect to detector pixel $\mathbf{K_f}$. In general, for a Cartesian reciprocal-space coordinate system (u, v), the aberration function can be defined up to third order as

$$\chi(u, v) = \sum_{\rho=1}^{12} a_\rho(u, v)\ S_\rho \tag{B.5}$$

where the aberration coefficients have been re-defined as S_ρ for convenience, and $a_\rho(u, v)$ is the *scattering vector function* [215]. For reference, Table B.1 contains a list of S_ρ and $a_\rho(u, v)$ terms up to third order. It should be noted that Equation (B.5) can be extended infinitely, however, only aberrations up to third order were considered in this thesis.

S_ρ	**Krivanek**	$a_\rho(u,v)$	**Name**
S_1	$C_{1,0}$	$\frac{1}{2}(u^2+v^2)$	Defocus
S_2	$C_{1,2a}$	$\frac{1}{2}(u^2-v^2)$	Two-fold astigmatism 0°
S_3	$C_{1,2b}$	uv	Two-fold astigmatism 45°
S_4	$C_{2,1a}$	$\frac{1}{3}u(u^2+v^2)$	Axial coma 0°
S_5	$C_{2,1b}$	$\frac{1}{3}v(u^2+v^2)$	Axial coma 90°
S_6	$C_{2,3a}$	$\frac{1}{3}u(u^2-3v^2)$	Three-fold astigmatism 0°
S_7	$C_{2,3b}$	$\frac{1}{3}v(3u^2-v^2)$	Three-fold astigmatism 30°
S_8	$C_{3,0}$	$\frac{1}{4}(u^2+v^2)^2$	Spherical aberration
S_9	$C_{3,2a}$	$\frac{1}{4}(u^4-v^4)$	Star aberration 0°
S_{10}	$C_{3,2b}$	$\frac{1}{2}uv(u^2-v^2)$	Star aberration 45°
S_{11}	$C_{3,4a}$	$\frac{1}{4}(u^4-6u^2v^2+v^2)$	Four-fold astigmatism 0°
S_{12}	$C_{3,4b}$	u^3v-uv^3	Four-fold astigmatism 22.5°

Table B.1: Aberration coefficients, S_ρ, up to third order, and their associated scattering vector functions, $a_\rho(u,v)$, for HRTEM and STEM imaging. Adapted from Refs. [18], [102] and [215].

Now that the aberration function has been re-defined, Equation (B.4) can be expressed as a set of linear equations described by $Y\mathbf{x} = \mathbf{b}$. For convenience, only the solution for the $-\mathbf{Q_p}$ side-band is given here, but an equivalent expression for the $+\mathbf{Q_p}$ side-band can be similarly determined. Equation (B.4) can be expressed as

$$Y = \left[W_\chi(\mathbf{K_f}, \mathbf{Q_p})_{(M\times 12)} \;\middle|\; \Lambda(\mathbf{Q_p})_{(M\times(N-12))} \right]_{M\times N} \tag{B.6}$$

$$\mathbf{x} = \left[S_{\rho\,(12\times 1)} \;\middle|\; \angle\Psi'(-\mathbf{Q_p})_{((N-12)\times 1)} \right]_{N\times 1} \tag{B.7}$$

$$\mathbf{b} = \left[\angle G(\mathbf{K_f}, \mathbf{Q_p}) \right]_{M\times 1} \tag{B.8}$$

where the vertical bar represents the column-wise augmentation of two matrices. The matrix

$$W_\chi(\mathbf{K_f}, \mathbf{Q_p}) = a_\rho(K_u, K_v) - a_\rho(K_u + Q_u, K_v + Q_v) \tag{B.9}$$

is a function of the scattering vector (K_u, K_v) and spatial frequency (Q_u, Q_v). For the i-th spatial frequency, $\mathbf{Q_{pi}}$, present in the matrix $\mathbf{b}$, the elements of the matrix $\Lambda(\mathbf{Q_p})$ are defined as

$$\Lambda(\mathbf{Q_p}) = 1, \;\text{ if }\; \mathbf{Q_p} = \mathbf{Q_{pi}}$$

$$\Lambda(\mathbf{Q_p}) = 0, \;\text{ elsewhere.} \tag{B.10}$$

Each M-th row of Y and $\mathbf{b}$ corresponds to a measurement acquired at a specific $(\mathbf{K_f}, \mathbf{Q_p})$ coordinate, and both matrices can be appended row-wise to incorporate all $G_{-\mathbf{Q_p}}(\mathbf{K_f}, \mathbf{Q_p})$ measurements within each DO region. The significance of $W_\chi(\mathbf{K_f}, \mathbf{Q_p})$ is that, similar to $G(\mathbf{K_f}, \mathbf{Q_p})$, it is hugely over-determined: there exist $K_u \times K_v \times Q_u \times Q_v$ values. This is orders of magnitude greater than the number of unknown aberration coefficients to third order (12), and allows for the solution of $\mathbf{x}$ via matrix inversion.

B.3 Aberration correction procedure

The procedure for the post-processing aberration correction performed in this thesis is as follows:

1. Prepare $Y\mathbf{x} = \mathbf{b}$ as described in Section B.2.

2. For $j = 1$, set $\mathbf{x_{j-1}} = \mathbf{x_0}$ and set all aberration coefficients inside $\mathbf{x_0}$ to zero. Set $\mathbf{b_{j-1}} = \mathbf{b_0}$.

3. Compute $\Delta\mathbf{x_j}$ from $Y \cdot \Delta\mathbf{x_j} = \mathbf{b_{j-1}}$ using SVD matrix inversion.

4. Calculate $\mathbf{x_j} = \mathbf{x_{j-1}} + \beta\Delta\mathbf{x_j}$, where β is an update parameter. This was set to 0.5 for the work shown in this thesis.

5. Determine $A(\mathbf{K_f})A^*(\mathbf{K_f} + \mathbf{Q_p})$ using the aberration coefficients in $\mathbf{x_j}$.

6. To compensate for the aberration values determined by SVD matrix inversion, multiply $G_{-\mathbf{Q_p}}(\mathbf{K_f}, \mathbf{Q_p})$ by the complex conjugate of the aberrated aperture functions determined in step 5. The phase of the resulting product is the updated phase of the DO region, $\angle G_{-\mathbf{Q_p}:cmp}(\mathbf{K_f}, \mathbf{Q_p})$. A phase-unwrapping procedure is performed to compensate for values of $\angle G_{-\mathbf{Q_p}:cmp}(\mathbf{K_f}, \mathbf{Q_p})$ greater than 2π.

7. Set the iteration number to $j = j + 1$ and prepare $\mathbf{b_j}$ from $\angle G_{-\mathbf{Q_p}:cmp}(\mathbf{K_f}, \mathbf{Q_p})$ calculated in step 6.

8. Repeat steps 3–7 until $\mathbf{x_j}$ has converged below a selected threshold.

A note on the iterative procedure

It should be noted that the aberration correction procedure need not be iterative: steps 1–5 can be performed to calculate aberrations up to third order if there is sufficient signal in the chosen values of $G(\mathbf{K_f}, \mathbf{Q_p})$. However, for data sets acquired using a low electron dose, an iterative procedure is implemented to reduce the errors introduced by phase unwrapping. This involves the iterative correction of low-order aberrations until convergence, after which higher-order aberrations can be incorporated in subsequent iterations.

A note on the input values of b

Only the values of $G(\mathbf{K_f}, \mathbf{Q_p})$ with a large modulus need to be chosen to enable the accurate determination of aberrations, e.g. the reciprocal-space locations of the reflections for a crystalline sample. To improve the accuracy of the determination of asymmetric aberrations, it is advised to choose $G(\mathbf{K_f}, \mathbf{Q_p})$ values from a wide range of spatial frequencies.

Bibliography

[1] K. Jeong-Min, C. Yoon-Seok, J. Hye Jun, L. Nam-Joo, K. Mi Seon, W. Sang Hee, P. Sehee, K. Jee Woong, K. Heui Man, and H. Myung-Guk, "Identification of Coronavirus Isolated from a Patient in Korea with COVID-19," *Osong Public Health and Research Perspectives*, vol. 11, no. 1, pp. 3–7, 2020.

[2] A. C. Walls, Y.-J. Park, M. A. Tortorici, A. Wall, A. T. McGuire, and D. Veesler, "Structure, Function, and Antigenicity of the SARS-CoV-2 Spike Glycoprotein," *Cell*, vol. 181, no. 2, pp. 281–292, 2020.

[3] M. U. Rothmann, W. Li, J. Etheridge, and Y.-B. Cheng, "Microstructural Characterisations of Perovskite Solar Cells – From Grains to Interfaces: Techniques, Features, and Challenges," *Advanced Energy Materials*, vol. 7, no. 23, p. 1700912, 2017.

[4] T. A. Doherty, A. J. Winchester, S. Macpherson, D. N. Johnstone, V. Pareek, E. M. Tennyson, S. Kosar, F. U. Kosasih, M. Anaya, M. Abdi-Jalebi, *et al.*, "Performance-limiting nanoscale trap clusters at grain junctions in halide perovskites," *Nature*, vol. 580, no. 7803, pp. 360–366, 2020.

[5] R. Grosso, E. N. Muccillo, D. N. Muche, G. S. Jawaharram, C. M. Barr, A. M. Monterrosa, R. H. Castro, K. Hattar, and S. J. Dillon, "In Situ Transmission

Electron Microscopy for Ultrahigh Temperature Mechanical Testing of ZrO2," *Nano Letters*, vol. 20, no. 2, pp. 1041–1046, 2020.

[6] Z. Liu, T. Hashimoto, I.-L. Tsai, G. Thompson, P. Skeldon, and H. Liu, "Scanning transmission electron microscopy technique for morphology analysis of anodic oxide film formed on titanium," *Vacuum*, vol. 115, pp. 19–22, 2015.

[7] H. Ryll, M. Simson, R. Hartmann, P. Holl, M. Huth, S. Ihle, Y. Kondo, P. Kotula, A. Liebel, K. Müller-Caspary, *et al.*, "A pnCCD-based, fast direct single electron imaging camera for TEM and STEM," *Journal of Instrumentation*, vol. 11, no. 04, pp. P04006–P04006, 2016.

[8] R. Clough and A. Kirkland, "Chapter One - Direct Digital Electron Detectors," vol. 198 of *Advances in Imaging and Electron Physics*, pp. 1–42, Elsevier, 2016.

[9] "DE-16 Camera System - blistering speed & stunning sensitivity." http://www.directelectron.com/wp-content/uploads/2019/12/DE-16-Product-Booklet.pdf, 2019. Accessed: 1st February, 2020.

[10] "MerlinEM." https://quantumdetectors.com/n/products/merlinem/, 2020. Accessed: 10th April, 2020.

[11] "Electron Microscope Pixel Array Detector (EMPAD) - high dynamic range direct electron detector for 4D STEM application." https://assets.thermofisher.com/TFS-Assets/MSD/Datasheets/EMPAD-Datasheet.pdf, 2018. Accessed: 1st February, 2020.

[12] "Beugung im inhomogenen Primärstrahlwellenfeld. I. Prinzip einer Phasenmessung von Elektronenbeugungsinterferenzen," *Acta Crystallographica Section A*, vol. 25, no. 4, pp. 495–501, 1969.

[13] J. M. Rodenburg and R. H. T. Bates, "The theory of super-resolution electron microscopy via Wigner-distribution deconvolution," *Philosophical Transactions of the Royal Society A: Mathematical, Physical and Engineering Sciences*, vol. 339, no. 1655, pp. 521–553, 1992.

[14] A. M. Maiden and J. M. Rodenburg, "An improved ptychographical phase retrieval algorithm for diffractive imaging," *Ultramicroscopy*, vol. 109, no. 10, pp. 1256–1262, 2009.

[15] P. Wang, F. Zhang, S. Gao, M. Zhang, and A. I. Kirkland, "Electron Ptychographic Diffractive Imaging of Boron Atoms in LaB_6 Crystals," *Scientific Reports*, vol. 7, no. 1, p. 2857, 2017.

[16] P. M. Pelz, W. X. Qiu, R. Bücker, G. Kassier, and R. D. Miller, "Low-dose cryo electron ptychography via non-convex Bayesian optimization," *Scientific Reports*, vol. 7, no. 1, pp. 1–13, 2017.

[17] J. G. Lozano, G. T. Martinez, L. Jin, P. D. Nellist, and P. G. Bruce, "Low-Dose Aberration-Free Imaging of Li-Rich Cathode Materials at Various States of Charge Using Electron Ptychography," *Nano Letters*, vol. 18, no. 11, pp. 6850–6855, 2018.

[18] H. Yang, R. Rutte, L. Jones, M. Simson, R. Sagawa, H. Ryll, M. Huth, T. J. Pennycook, M. L. H. Green, H. Soltau, *et al.*, "Simultaneous atomic-resolution electron ptychography and Z-contrast imaging of light and heavy elements in complex nanostructures," *Nature Communications*, vol. 7, p. 12532, 2016.

[19] Y. Jiang, Z. Chen, Y. Han, P. Deb, H. Gao, S. Xie, P. Purohit, M. W. Tate, J. Park, S. M. Gruner, *et al.*, "Electron ptychography of 2D materials to deep sub-ångström resolution," *Nature*, vol. 559, pp. 343–349, 2018.

[20] T. Chen, I. Ellis, T. J. N. Hooper, E. Liberti, L. Ye, B. T. W. Lo, C. O'Leary, A. A. Sheader, G. T. Martinez, L. Jones, *et al.*, "Interstitial Boron Atoms in the Palladium Lattice of an Industrial Type of Nanocatalyst: Properties and Structural Modifications," *Journal of the American Chemical Society*, vol. 141, no. 50, pp. 19616–19624, 2019.

[21] J. M. Zuo and J. C. H. Spence, *Advanced Transmission Electron Microscopy : Imaging and Diffraction in Nanoscience*. New York: Springer, 2016.

[22] D. Shindo and T. Oikawa, *Analytical Electron Microscopy for Materials Science*. Springer Science & Business Media, 2013.

[23] J. Hong, Z. Hu, M. Probert, K. Li, D. Lv, X. Yang, L. Gu, N. Mao, Q. Feng, L. Xie, *et al.*, "Exploring atomic defects in molybdenum disulphide monolayers," *Nature Communications*, vol. 6, no. 1, p. 6293, 2015.

[24] G. T. Martinez, T. C. Naginey, L. Jones, C. M. O'Leary, T. J. Pennycook, R. J. Nicholls, J. R. Yates, and P. D. Nellist, "Direct Imaging of Charge Redistribution due to Bonding at Atomic Resolution via Electron Ptychography," arXiv:1907.12974v1 [cond-mat.mtrl-sci], 2019.

[25] L. Jones, K. E. MacArthur, V. T. Fauske, A. T. J. Van Helvoort, and P. D. Nellist, "Rapid Estimation of Catalyst Nanoparticle Morphology and Atomic-Coordination by High-Resolution Z-Contrast Electron Microscopy," *Nano Letters*, vol. 14, no. 11, pp. 6336–6341, 2014.

[26] T. R. D. Costa, A. Ignatiou, and E. V. Orlova, *Structural Analysis of Protein Complexes by Cryo Electron Microscopy*. New York, NY: Springer New York, 2017.

[27] K. K. Lee and L. Gui, "Dissecting Virus Infectious Cycles by Cryo-Electron Microscopy," *PLOS Pathogens*, vol. 12, no. 6, pp. 1–8, 2016.

[28] D. B. Williams and C. B. Carter, *Transmission Electron Microscopy: A Textbook for Materials Science*, vol. V1–V4. Springer, 1996.

[29] P. Hirsch, D. Cockayne, J. Spence, and M. Whelan, "50 Years of TEM of dislocations: Past, present and future," *Philosophical Magazine*, vol. 86, no. 29–31, pp. 4519–4528, 2006.

[30] M. De Graef, *Introduction to Conventional Transmission Electron Microscopy*. Cambridge: Cambridge University Press, 2003.

[31] M. Tanaka, "Convergent-Beam Electron Diffraction," in *Electron Crystallography*, pp. 77–113, Dordrecht: Springer Netherlands, 1997.

[32] M. von Ardenne, "Das Elektronen-Rastermikroskop - Theoretische Grundlagen," *Zeitschrift für Physik*, vol. 109, no. 9–10, pp. 553–572, 1938.

[33] P. D. Nellist, "Scanning Transmission Electron Microscopy," in *Springer Handbook of Microscopy*, pp. 49–99, Springer International Publishing, 2019.

[34] V. Ronchi, "Forty Years of History of a Grating Interferometer," *Applied Optics*, vol. 3, no. 4, pp. 437–451, 1964.

[35] P. D. Nellist, "Principles of STEM imaging," in *Scanning Transmission Electron Microscopy: Imaging and Analysis*, pp. 91–115, Springer Science & Business Media, 2011.

[36] C. Ophus, "Four-Dimensional Scanning Transmission Electron Microscopy (4D-STEM): From Scanning Nanodiffraction to Ptychography and Beyond," *Microscopy and Microanalysis*, vol. 25, no. 3, pp. 563–582, 2019.

[37] J. M. Cowley, "Image contrast in a transmission scanning electron microscope," *Applied Physics Letters*, vol. 15, no. 2, pp. 58–59, 1969.

[38] H. Rose, "Phase-contrast in scanning-transmission electron-microscopy," *Optik*, vol. 39, no. 4, pp. 416–436, 1974.

[39] C. Humphreys, "Fundamental concepts of STEM imaging," *Ultramicroscopy*, vol. 7, no. 1, pp. 7–12, 1981.

[40] E. Liberti, G. Martinez, C. O'Leary, P. Nellist, and A. Kirkland, "Phase Retrieval Quantitative Comparison Between Tilt-series Imaging in TEM and Position-resolved Coherent Diffractive Imaging in STEM," *Microscopy and Microanalysis*, vol. 23, no. S1, pp. 470–471, 2017.

[41] F. F. Krause and A. Rosenauer, "Reciprocity relations in transmission electron microscopy: A rigorous derivation," *Micron*, vol. 92, pp. 1–5, 2017.

[42] A. Varambhia, L. Jones, A. De Backer, V. Fauske, S. Van Aert, D. Ozkaya, S. Lozano-Perez, and P. Nellist, "Experiment design for quantitative dark field imaging and spectroscopy of catalyst nanoparticles using Scanning Transmission Electron Microscopy (STEM)," in *European Microscopy Congress 2016: Proceedings*, pp. 537–538, 2016.

[43] G. Botton and S. Prabhudev, "Analytical Electron Microscopy," in *Springer Handbook of Microscopy*, pp. 345–453, Springer International Publishing, 2019.

[44] S. Lu, Y. Zheng, and S. Bai, "A HRTEM/EDX approach to identification of the source of dust particles on urban tree leaves," *Atmospheric Environment*, vol. 42, no. 26, pp. 6431–6441, 2008.

[45] H. Ibach and D. L. Mills, *Electron Energy Loss Spectroscopy and Surface Vibrations*. Academic Press, 1982.

[46] R. Egerton, *Electron Energy-Loss Spectroscopy in the Electron Microscope*. Springer, 2011.

[47] J. Gázquez, G. Sánchez-Santolino, N. Biškup, M. A. Roldán, M. Cabero, S. J. Pennycook, and M. Varela, "Applications of STEM-EELS to complex oxides," *Materials Science in Semiconductor Processing*, vol. 65, pp. 49–63, 2017.

[48] A. M. Varambhia, *Quantitative structural and compositional studies of catalyst nanoparticles using imaging and spectroscopy in STEM.* DPhil Thesis, University of Oxford, 2018.

[49] R. D. Leapman, "Application of EELS and EFTEM to the life sciences enabled by the contributions of Ondrej Krivanek," *Ultramicroscopy*, vol. 180, pp. 180–187, 2017.

[50] F. Hofer, W. Grogger, P. Warbichler, and I. Papst, "Quantitative Energy-Filtering Transmission Electron Microscopy (EFTEM)," *Microchimica Acta*, vol. 132, no. 2–4, pp. 273–288, 2000.

[51] R. Egerton, "Radiation damage to organic and inorganic specimens in the TEM," *Micron*, vol. 119, pp. 72–87, 2019.

[52] S. D. Findlay, R. Huang, R. Ishikawa, N. Shibata, and Y. Ikuhara, "Direct visualization of lithium via annular bright field scanning transmission electron microscopy: a review," *Microscopy*, vol. 66, no. 1, pp. 3–14, 2016.

[53] P. A. Crozier, "Vibrational and valence aloof beam EELS: A potential tool for nondestructive characterization of nanoparticle surfaces," *Ultramicroscopy*, vol. 180, pp. 104–114, 2017.

[54] A. Varambhia, L. Jones, A. London, D. Ozkaya, P. D. Nellist, and S. Lozano-Perez, "Determining EDS and EELS partial cross-sections from multiple calibration standards to accurately quantify bi-metallic nanoparticles using STEM," *Micron*, vol. 113, pp. 69–82, 2018.

[55] E. J. Kirkland, *Advanced Computing in Electron Microscopy*. Springer Science & Business Media, 2010.

[56] Y. Liao, "Practical Electron Microscopy and Database." www.globalsino.com/EM/, 2018. Accessed: 11th April, 2020.

[57] J. Barthel, M. Cattaneo, B. G. Mendis, S. D. Findlay, and L. J. Allen, "Angular dependence of fast-electron scattering from materials," *Phys. Rev. B*, vol. 101, p. 184109, 2020.

[58] J. C. Spence, *High-Resolution Electron Microscopy*. OUP Oxford, 2013.

[59] D. L. Misell, G. W. Stroke, and M. Halioua, "Coherent and incoherent imaging in the scanning transmission electron microscope," *Journal of Physics D: Applied Physics*, vol. 7, no. 10, pp. L113–L117, 1974.

[60] A. V. Crewe, J. Wall, and J. Langmore, "Visibility of Single Atoms," *Science (New York, N.Y.)*, vol. 168, no. 3937, pp. 1338–1340, 1970.

[61] N. Shibata, S. D. Findlay, Y. Kohno, H. Sawada, Y. Kondo, and Y. Ikuhara, "Differential phase-contrast microscopy at atomic resolution," *Nature Physics*, vol. 8, no. 8, pp. 611–615, 2012.

[62] I. Lazić, E. G. Bosch, and S. Lazar, "Phase contrast STEM for thin samples: Integrated differential phase contrast," *Ultramicroscopy*, vol. 160, pp. 265–280, 2016.

[63] K. Cowtan, "Phase problem in X-ray crystallography, and its solution," *Encyclopedia of Life Sciences*, 2001.

[64] J. Miao, R. L. Sandberg, and C. Song, "Coherent X-Ray Diffraction Imaging," *IEEE Journal of Selected Topics in Quantum Electronics*, vol. 18, no. 1, pp. 399–410, 2012.

[65] J. Rodenburg, "Ptychography and Related Diffractive Imaging Methods," vol. 150 of *Advances in Imaging and Electron Physics*, pp. 87–184, Elsevier, 2008.

[66] J. M. Rodenburg, "The phase problem, microdiffraction and wavelength-limited resolution - a discussion," *Ultramicroscopy*, vol. 27, no. 4, pp. 413–422, 1989.

[67] H. A. Hauptman, "The Phase Problem of X-ray Crystallography: Overview," in *Electron Crystallography*, pp. 131–138, Dordrecht: Springer Netherlands, 1997.

[68] A. L. Patterson, "A Fourier Series Method for the Determination of the Components of Interatomic Distances in Crystals," *Physical Review*, vol. 46, pp. 372–376, 1934.

[69] H. Hauptman, "The Direct Methods of X-ray Crystallography," *Science*, vol. 233, no. 4760, pp. 178–183, 1986.

[70] D. Green, V. M. Ingram, and M. F. Perutz, "The structure of haemoglobin-IV. Sign determination by the isomorphous replacement method," *Proceedings of the Royal Society of London. Series A. Mathematical and Physical Sciences*, vol. 225, no. 1162, pp. 287–307, 1954.

[71] W. A. Hendrickson, "Analysis of protein structure from diffraction measurement at multiple wavelengths," *Transactions of the American Crystallographic Association*, vol. 21, pp. 11–21, 1985.

[72] J. Drenth, "The molecular replacement method. A collection of papers on the use of non-crystallographic symmetry," *Acta Crystallographica Section A: Crystal Physics, Diffraction, Theoretical and General Crystallography*, vol. 30, no. 2, pp. 304–304, 1974.

[73] K. Ayyer, O. M. Yefanov, D. Oberthür, S. Roy-Chowdhury, L. Galli, V. Mariani, S. Basu, J. Coe, C. E. Conrad, R. Fromme, *et al.*, "Macromolecular diffractive imaging using imperfect crystals," *Nature*, vol. 530, no. 7589, pp. 202–206, 2016.

[74] R. W. Gerchberg and W. O. Saxton, "A Practical Algorithm for Determination of Phase from Image and Diffraction Plane Pictures," *Optik*, vol. 35, no. 2, pp. 237–246, 1972.

[75] J. R. Fienup, "Phase retrieval algorithms: a comparison," *Applied Optics*, vol. 21, no. 15, pp. 2758–2769, 1982.

[76] D. Sayre, "Some implications of a theorem due to Shannon," *Acta Crystallographica*, vol. 5, no. 6, pp. 843–843, 1952.

[77] J. Miao, P. Charalambous, J. Kirz, and D. Sayre, "Extending the methodology of X-ray crystallography to allow imaging of micrometre-sized non-crystalline specimens," *Nature*, vol. 400, no. 6742, pp. 342–344, 1999.

[78] J. Miao, D. Sayre, and H. N. Chapman, "Phase retrieval from the magnitude of the Fourier transforms of nonperiodic objects," *Journal of the Optical Society of America A*, vol. 15, no. 6, pp. 1662–1669, 1998.

[79] J. R. Fienup, "Reconstruction of an object from the modulus of its Fourier transform," *Optics Letters*, vol. 3, no. 1, pp. 27–29, 1978.

[80] D. Sayre, H. Chapman, and J. Miao, "On the Extendibility of X-ray Crystallography to Noncrystals," *Acta Crystallographica Section A: Foundations of Crystallography*, vol. 54, no. 2, pp. 232–239, 1998.

[81] J. Gulden, O. Yefanov, A. Mancuso, V. Abramova, J. Hilhorst, D. Byelov, I. Snigireva, A. Snigirev, A. Petukhov, and I. Vartanyants, "Coherent X-ray

imaging of defects in colloidal crystals," *Physical Review B*, vol. 81, no. 22, p. 224105, 2010.

[82] H. Jiang, D. Ramunno-Johnson, C. Song, B. Amirbekian, Y. Kohmura, Y. Nishino, Y. Takahashi, T. Ishikawa, and J. Miao, "Nanoscale Imaging of Mineral Crystals Inside Biological Composite Materials Using X-ray Diffraction Microscopy," *Physical Review Letters*, vol. 100, no. 3, p. 038103, 2008.

[83] J. M. Zuo, I. Vartanyants, M. Gao, R. Zhang, and L. A. Nagahara, "Atomic Resolution Imaging of a Carbon Nanotube from Diffraction Intensities," *Science*, vol. 300, no. 5624, pp. 1419–1421, 2003.

[84] J. Spence, U. Weierstall, and M. Howells, "Phase recovery and lensless imaging by iterative methods in optical, X-ray and electron diffraction," *Philosophical Transactions of the Royal Society of London. Series A: Mathematical, Physical and Engineering Sciences*, vol. 360, no. 1794, pp. 875–895, 2002.

[85] J. Miao, T. Ohsuna, O. Terasaki, K. O. Hodgson, and M. A. O'Keefe, "Atomic Resolution Three-Dimensional Electron Diffraction Microscopy," *Physical Review Letters*, vol. 89, no. 15, p. 155502, 2002.

[86] H. N. Chapman, A. Barty, M. J. Bogan, S. Boutet, M. Frank, S. P. Hau-Riege, S. Marchesini, B. W. Woods, S. Bajt, W. H. Benner, *et al.*, "Femtosecond diffractive imaging with a soft-X-ray free-electron laser," *Nature Physics*, vol. 2, no. 12, pp. 839–843, 2006.

[87] A. Barty, S. Boutet, M. J. Bogan, S. Hau-Riege, S. Marchesini, K. Sokolowski-Tinten, N. Stojanovic, H. Ehrke, A. Cavalleri, S. Düsterer, *et al.*, "Ultrafast single-shot diffraction imaging of nanoscale dynamics," *Nature Photonics*, vol. 2, no. 7, pp. 415–419, 2008.

[88] J. M. Rodenburg and H. M. L. Faulkner, "A phase retrieval algorithm for shifting illumination," *Applied Physics Letters*, vol. 85, no. 20, pp. 4795–4797, 2004.

[89] G. Zheng, R. Horstmeyer, and C. Yang, "Wide-field, high-resolution Fourier ptychographic microscopy," *Nature Photonics*, vol. 7, no. 9, pp. 739–745, 2013.

[90] F. Zernike, "Phase contrast, a new method for the microscopic observation of transparent objects," *Physica*, vol. 9, no. 10, pp. 974–986, 1942.

[91] R. Danev and K. Nagayama, "Transmission electron microscopy with Zernike phase plate," *Ultramicroscopy*, vol. 88, no. 4, pp. 243–252, 2001.

[92] A. I. Kirkland and R. R. Meyer, ""Indirect" High-Resolution Transmission Electron Microscopy: Aberration Measurement and Wavefunction Reconstruction," *Microscopy and Microanalysis*, vol. 10, no. 4, pp. 401–413, 2004.

[93] S. J. Haigh, H. Sawada, and A. I. Kirkland, "Atomic Structure Imaging beyond Conventional Resolution Limits in the Transmission Electron Microscope," *Physical Review Letters*, vol. 103, no. 12, pp. 16–19, 2009.

[94] C. Ophus and T. Ewalds, "Guidelines for quantitative reconstruction of complex exit waves in HRTEM," *Ultramicroscopy*, vol. 113, pp. 88–95, 2012.

[95] D. Gabor, W. E. Kock, and G. W. Stroke, "Holography," *Science (New York, N.Y.)*, vol. 173, no. 3991, pp. 11–23, 1971.

[96] H. Lichte, "Electron holography approaching atomic resolution," *Ultramicroscopy*, vol. 20, no. 3, pp. 293–304, 1986.

[97] T. J. Pennycook, A. R. Lupini, H. Yang, M. F. Murfitt, L. Jones, and P. D. Nellist, "Efficient phase contrast imaging in STEM using a pixelated detector.

Part 1: Experimental demonstration at atomic resolution," *Ultramicroscopy*, vol. 151, pp. 160–167, 2015.

[98] J. C. H. Spence, "Diffractive Imaging of Single Particles," in *Springer Handbook of Microscopy*, pp. 1009–1936, Springer International Publishing, 2019.

[99] O. Scherzer, "The Theoretical Resolution Limit of the Electron Microscope," *Journal of Applied Physics*, vol. 20, no. 1, pp. 20–29, 1949.

[100] S. J. Haigh and A. I. Kirkland, "Aberration-Corrected Imaging in CTEM," in *Aberration-Corrected Analytical Transmission Electron Microscopy*, ch. 9, pp. 241–261, John Wiley & Sons, Ltd, 2011.

[101] O. Scherzer, "Über einige Fehler von Elektronenlinsen," *Zeitschrift für Physik*, vol. 101, no. 9–10, pp. 593–603, 1936.

[102] S. J. Haigh, *Super Resolution Tilt Series Exit Wave Restoration from Aberration Corrected Images*. DPhil Thesis, University of Oxford, 2008.

[103] A. I. Kirkland, L.-Y. Chang, and J. L. Hutchison, "Atomic Resolution Transmission Electron Microscopy," in *Springer Handbook of Microscopy*, pp. 3–47, Springer International Publishing, 2019.

[104] C. Hetherington, "Aberration correction for TEM," *Materials Today*, vol. 7, no. 12, pp. 50–55, 2004.

[105] K. Ishizuka, "Contrast transfer of crystal images in TEM," *Ultramicroscopy*, vol. 5, no. 1, pp. 55–65, 1980.

[106] F. Thon, "Zur Defokussierungsabhängigkeit des Phasen-kontrastes bei der elektronenmikroskopischen Abbildung," *Zeitschrift für Naturforschung A*, vol. 21, no. 4, pp. 476–478, 1966.

[107] D. J. Smith, "Ultimate resolution in the electron microscope?," *Materials Today*, vol. 11, pp. 30–38, 2008.

[108] M. A. O'Keefe, ""Resolution" in high-resolution electron microscopy," *Ultramicroscopy*, vol. 47, no. 1-3, pp. 282–297, 1992.

[109] J. Zach and M. Haider, "Aberration correction in a low voltage SEM by a multipole corrector," *Nuclear Instruments and Methods in Physics Research, A*, vol. 363, no. 1–2, pp. 316–325, 1995.

[110] O. L. Krivanek, N. Dellby, A. J. Spence, R. A. Camps, and L. M. Brown, "Aberration correction in the STEM," in *Institute of Physics Conference Series: EMAG97*, vol. 153, pp. 35–40, 1997.

[111] M. Haider, S. Uhlemann, E. Schwan, H. Rose, B. Kabius, and K. Urban, "Electron microscopy image enhanced," *Nature*, vol. 392, no. 6678, pp. 768–769, 1998.

[112] N. Dellby, O. L. Krivanek, P. D. Nellist, P. E. Batson, and A. R. Lupini, "Progress in aberration-corrected scanning transmission electron microscopy," *Journal of Electron Microscopy*, vol. 50, no. 3, pp. 177–185, 2001.

[113] H. Lichte, "Electron holography of atomic structures - Prospect and limitations," *Physica B+C*, vol. 151, no. 1–2, pp. 214–222, 1988.

[114] A. I. Kirkland, W. O. Saxton, K. L. Chau, K. Tsuno, and M. Kawasaki, "Super-resolution by aperture synthesis: tilt series reconstruction in CTEM," *Ultramicroscopy*, vol. 57, no. 4, pp. 355–374, 1995.

[115] S. J. Haigh, B. Jiang, D. Alloyeau, C. Kisielowski, and A. I. Kirkland, "Recording low and high spatial frequencies in exit wave reconstructions," *Ultramicroscopy*, vol. 133, pp. 26–34, 2013.

[116] R. Danev, B. Buijsse, M. Khoshouei, J. M. Plitzko, and W. Baumeister, "Volta potential phase plate for in-focus phase contrast transmission electron microscopy," *Proceedings of the National Academy of Sciences*, vol. 111, no. 44, pp. 15635–15640, 2014.

[117] O. von Loeffelholz, G. Papai, R. Danev, A. G. Myasnikov, S. K. Natchiar, I. Hazemann, J.-F. Ménétret, and B. P. Klaholz, "Volta phase plate data collection facilitates image processing and cryo-EM structure determination," *Journal of Structural Biology*, vol. 202, no. 3, pp. 191–199, 2018.

[118] S. Hettler, E. Kano, M. Dries, D. Gerthsen, L. Pfaffmann, M. Bruns, M. Beleggia, and M. Malac, "Charging of carbon thin films in scanning and phase-plate transmission electron microscopy," *Ultramicroscopy*, vol. 184, pp. 252–266, 2018.

[119] F. Winkler, J. Barthel, A. H. Tavabi, S. Borghardt, B. E. Kardynal, and R. E. Dunin-Borkowski, "Absolute Scale Quantitative Off-Axis Electron Holography at Atomic Resolution," *Physical Review Letters*, vol. 120, p. 156101, 2018.

[120] M. Born, "Quantenmechanik der Stossvorgänge," *Zeitschrift für Physik*, vol. 38, no. 11–12, pp. 803–827, 1926.

[121] P. P. Ewald, "Zur theorie der interferenzen der röntgenstrahlen in kristallen," *Physikalische Zeitschrift*, vol. 14, no. 11, p. 465, 1913.

[122] R. Henderson, "The potential and limitations of neutrons, electrons and X-rays for atomic resolution microscopy of unstained biological molecules," *Quarterly Reviews of Biophysics*, vol. 28, no. 2, p. 171–193, 1995.

[123] C. Darwin, "The theory of X-ray reflexion," *Philosophical Magazine Series 6*, vol. 27, no. 158, pp. 315–333, 1914.

[124] D. V. Dyck and J. Chen, "A simple theory for dynamical electron diffraction in crystals," *Solid State Communications*, vol. 109, no. 8, pp. 501–505, 1999.

[125] T. Plamann and J. M. Rodenburg, "Electron Ptychography. II. Theory of Three-Dimensional Propagation Effects," *Acta Crystallographica Section A: Foundations of Crystallography*, vol. 54, no. 1, pp. 61–73, 1998.

[126] H. G. Brown, Z. Chen, M. Weyland, C. Ophus, J. Ciston, L. J. Allen, and S. D. Findlay, "Structure Retrieval at Atomic Resolution in the Presence of Multiple Scattering of the Electron Probe," *Physical Review Letters*, vol. 121, p. 266102, 2018.

[127] H.-P. Karnthaler and E. Wintner, "Weak beam TEM studies of composite dislocations in FCC alloys," *Acta Metallurgica*, vol. 23, no. 12, pp. 1501–1509, 1975.

[128] Y. Sun and P. Hazzledine, "A TEM weak-beam study of dislocations in γ' in a deformed Ni-based superalloy," *Philosophical Magazine A*, vol. 58, no. 4, pp. 603–617, 1988.

[129] J. Barnard, J. Sharp, J. Tong, and P. Midgley, "Three-dimensional analysis of dislocation networks in GaN using weak-beam dark-field electron tomography," *Philosophical Magazine*, vol. 86, no. 29–31, pp. 4901–4922, 2006.

[130] A. De Backer, G. T. Martinez, K. E. MacArthur, L. Jones, A. Béché, P. D. Nellist, and S. Van Aert, "Dose limited reliability of quantitative annular dark field scanning transmission electron microscopy for nano-particle atom-counting," *Ultramicroscopy*, vol. 151, pp. 56–61, 2015.

[131] O. L. K. Murfitt, N. Dellby, and M. F, "Aberration-corrected scanning transmission electron microscopy of semiconductors," *Journal of Physics: Conference Series*, vol. 326, no. 1, p. 12005, 2011.

[132] J. Gonnissen, A. De Backer, A. Den Dekker, G. Martinez, A. Rosenauer, J. Sijbers, and S. Van Aert, "Optimal experimental design for the detection of light atoms from high-resolution scanning transmission electron microscopy images," *Applied Physics Letters*, vol. 105, no. 6, p. 063116, 2014.

[133] R. Hovden and D. A. Muller, "Efficient elastic imaging of single atoms on ultrathin supports in a scanning transmission electron microscope," *Ultramicroscopy*, vol. 123, pp. 59–65, 2012.

[134] F. H. Baumann, "Very low angle annular dark field imaging in the scanning transmission electron microscope: A versatile tool for micro- and nanocharacterization," *Journal of Vacuum Science & Technology B*, vol. 30, no. 4, p. 041804, 2012.

[135] T. Smith, B. Esser, E. George, F. Otto, M. Ghazisaeidi, D. McComb, and M. Mills, "HAADF/MAADF Observations and Image Simulations of Dislocation Core Structures in a High Entropy Alloy," *Microscopy and Microanalysis*, vol. 21, no. S3, p. 2205–2206, 2015.

[136] S. D. Findlay, N. Shibata, H. Sawada, E. Okunishi, Y. Kondo, and Y. Ikuhara, "Dynamics of annular bright field imaging in scanning transmission electron microscopy," *Ultramicroscopy*, vol. 110, no. 7, pp. 903–923, 2010.

[137] S. D. Findlay, N. Shibata, H. Sawada, E. Okunishi, Y. Kondo, T. Yamamoto, and Y. Ikuhara, "Robust atomic resolution imaging of light elements using scanning transmission electron microscopy," *Applied Physics Letters*, vol. 95, no. 19, p. 191913, 2009.

[138] S. D. Findlay, T. Saito, N. Shibata, Y. Sato, J. Matsuda, K. Asano, E. Akiba, T. Hirayama, and Y. Ikuhara, "Direct Imaging of Hydrogen within a Crystalline Environment," *Applied Physics Express*, vol. 3, no. 11, p. 116603, 2010.

[139] C. Dinges, H. Kohl, and H. Rose, "High-resolution imaging of crystalline objects by hollow-cone illumination," *Ultramicroscopy*, vol. 55, no. 1, pp. 91–100, 1994.

[140] S. Lee, Y. Oshima, E. Hosono, H. Zhou, and K. Takayanagi, "Reversible contrast in focus series of annular bright field images of a crystalline LiMn2O4 nanowire," *Ultramicroscopy*, vol. 125, pp. 43–48, 2013.

[141] N. H. Dekkers and H. de Lang, "Differential Phase Contrast in a STEM," *Optik*, vol. 41, no. 4, pp. 452–456, 1974.

[142] R. Ishikawa, S. D. Findlay, T. Seki, G. Sánchez-Santolino, Y. Kohno, Y. Ikuhara, and N. Shibata, "Direct electric field imaging of graphene defects," *Nature Communications*, vol. 9, no. 1, p. 3878, 2018.

[143] E. M. Waddell and J. N. Chapman, "Linear imaging of strong phase objects using asymmetric detectors in STEM," *Optik (Jena)*, vol. 54, pp. 83–96, 1979.

[144] K. Müller, F. F. Krause, A. Béché, M. Schowalter, V. Galioit, S. Löffler, J. Verbeeck, J. Zweck, P. Schattschneider, *et al.*, "Atomic electric fields revealed by a quantum mechanical approach to electron picodiffraction.," *Nature Communications*, vol. 5, p. 5653, 2014.

[145] K. Müller-Caspary, F. F. Krause, T. Grieb, S. Löffler, M. Schowalter, A. Béché, V. Galioit, D. Marquardt, J. Zweck, P. Schattschneider, *et al.*, "Measurement of atomic electric fields and charge densities from average momentum transfers using scanning transmission electron microscopy," *Ultramicroscopy*, vol. 178, pp. 62–80, 2017.

[146] E. Yücelen, I. Lazić, and E. G. Bosch, "Phase contrast scanning transmission electron microscopy imaging of light and heavy atoms at the limit of contrast and resolution," *Scientific Reports*, vol. 8, no. 1, pp. 1–10, 2018.

[147] J. N. Chapman, I. R. McFadyen, and S. McVitie, "Modified differential phase contrast Lorentz microscopy for improved imaging of magnetic structures," *IEEE Transactions on Magnetics*, vol. 26, no. 5, pp. 1506–1511, 1990.

[148] J. Cowley and J. Spence, "Innovative imaging and microdiffraction in STEM," *Ultramicroscopy*, vol. 3, pp. 433–438, 1978.

[149] A. R. Lupini, "The Electron Ronchigram," in *Scanning Transmission Electron Microscopy: Imaging and Analysis*, pp. 117–161, Springer, 2011.

[150] L. Jones, H. C. Yang, T. J. Pennycook, M. S. J. Marshall, S. V. Aert, N. D. Browning, M. R. Castell, and P. D. Nellist, "Smart Align—a new tool for robust non-rigid registration of scanning microscope data," *Advanced Structural and Chemical Imaging*, vol. 1, pp. 1–16, 2015.

[151] R. N. Clough, G. Moldovan, and A. I. Kirkland, "Direct Detectors for Electron Microscopy," *Journal of Physics: Conference Series*, vol. 522, p. 012046, 2014.

[152] J. H. Mendez, A. Mehrani, P. Randolph, and S. Stagg, "Throughput and resolution with a next-generation direct electron detector," *IUCrJ*, vol. 6, no. 6, pp. 1007–1013, 2019.

[153] S. K. Mendis, S. E. Kemeny, R. C. Gee, B. Pain, C. O. Staller, Quiesup Kim, and E. R. Fossum, "CMOS Active Pixel Image Sensors for Highly Integrated Imaging Systems," *IEEE Journal of Solid-State Circuits*, vol. 32, no. 2, pp. 187–197, 1997.

[154] A.-C. Milazzo, P. Leblanc, F. Duttweiler, L. Jin, J. C. Bouwer, S. Peltier, M. Ellisman, F. Bieser, H. S. Matis, H. Wieman, *et al.*, "Active pixel sensor array as a detector for electron microscopy," *Ultramicroscopy*, vol. 104, no. 2, pp. 152–159, 2005.

[155] A.-C. Milazzo, G. Moldovan, J. Lanman, L. Jin, J. C. Bouwer, S. Klienfelder, S. T. Peltier, M. H. Ellisman, A. I. Kirkland, and N.-H. Xuong, "Characterization of a direct detection device imaging camera for transmission electron microscopy," *Ultramicroscopy*, vol. 110, no. 7, pp. 741–744, 2010.

[156] M. W. Tate, P. Purohit, D. Chamberlain, K. X. Nguyen, R. Hovden, C. S. Chang, P. Deb, E. Turgut, J. T. Heron, Schlom, *et al.*, "High Dynamic Range Pixel Array Detector for Scanning Transmission Electron Microscopy," *Microscopy and Microanalysis*, vol. 22, no. 1, pp. 237–249, 2016.

[157] J. Mir, R. Clough, R. MacInnes, C. Gough, R. Plackett, I. Shipsey, H. Sawada, I. MacLaren, R. Ballabriga, D. Maneuski, *et al.*, "Characterisation of the Medipix3 detector for 60 and 80 keV electrons," *Ultramicroscopy*, vol. 182, pp. 44–53, 2017.

[158] "The pnCCD (S)TEM Camera." https://pndetector.com/w/wp-content/uploads/2016/03/Flyer_TEM.pdf, 2016. Accessed: 9th April, 2020.

[159] J. Ciston, I. J. Johnson, B. R. Draney, P. Ercius, E. Fong, A. Goldschmidt, J. M. Joseph, J. R. Lee, A. Mueller, C. Ophus, *et al.*, "The 4D Camera: Very High Speed Electron Counting for 4D-STEM," *Microscopy and Microanalysis*, vol. 25, no. S2, p. 1930–1931, 2019.

[160] "MerlinEM Technical Datasheet." https://quantumdetectors.com/wp-content/uploads/2019/11/2347-MerlinEM-Technical-datasheet.pdf. Accessed: 1st February, 2020.

[161] S. Dey, A. Morawiec, E. Bouzy, A. Hazotte, and J. Fundenberger, "A technique for determination of / interface relationships in a (2+) TiAl base alloy using TEM Kikuchi patterns," *Materials Letters*, vol. 60, no. 5, pp. 646–650, 2006.

[162] N. Bozzolo, N. Dewobroto, H. R. Wenk, and F. Wagner, "Microstructure and microtexture of highly cold-rolled commercially pure titanium," *Journal of Materials Science*, vol. 42, no. 7, pp. 2405–2416, 2007.

[163] I. MacLaren, R. Villaurrutia, and A. Peláiz-Barranco, "Domain structures and nanostructures in incommensurate antiferroelectric $Pb_xLa_{1-x}(Zr_{0.9}Ti_{0.1})O_3$," *Journal of Applied Physics*, vol. 108, no. 3, p. 034109, 2010.

[164] J. A. Hachtel, J. C. Idrobo, and M. Chi, "Sub-Ångstrom electric field measurements on a universal detector in a scanning transmission electron microscope," *Advanced Structural and Chemical Imaging*, vol. 4, no. 1, p. 10, 2018.

[165] W. Gao, C. Addiego, H. Wang, X. Yan, Y. Hou, D. Ji, C. Heikes, Y. Zhang, L. Li, H. Huyan, *et al.*, "Real-space charge-density imaging with sub-ångström resolution by four-dimensional electron microscopy," *Nature*, vol. 575, no. 7783, pp. 480–484, 2019.

[166] S. Fang, Y. Wen, C. S. Allen, C. Ophus, G. G. D. Han, A. I. Kirkland, E. Kaxiras, and J. H. Warner, "Atomic electrostatic maps of 1D channels in 2D semiconductors using 4D scanning transmission electron microscopy," *Nature Communications*, vol. 10, no. 1, p. 1127, 2019.

[167] P. Schiske, "Image reconstruction by means of focus series," *Journal of Microscopy*, vol. 207, no. 2, p. 154, 2002.

[168] P. Hawkes, "An alternative to Schiske's least mean-square error filter," *Optik*, vol. 41, pp. 64–68, 1974.

[169] W. Saxton, "Accurate alignment of sets of images," *Journal of Microscopy*, vol. 174, no. 2, pp. 61–68, 1994.

[170] W. Coene, A. Thust, M. O. de Beeck, and D. V. Dyck, "Maximum-likelihood method for focus-variation image reconstruction in high resolution transmission electron microscopy," *Ultramicroscopy*, vol. 64, no. 1, pp. 109–135, 1996.

[171] M. A. O'Keefe, E. C. Nelson, Y. C. Wang, and A. Thust, "Sub-ångström resolution of atomistic structures below 0.8 Å," *Philosophical Magazine Part B*, vol. 81, no. 11, pp. 1861–1878, 2001.

[172] A. I. Kirkland, W. O. Saxton, and G. Chand, "Multiple beam tilt microscopy for super resolved imaging," *Journal of Electron Microscopy*, vol. 46, no. 1, pp. 11–22, 1997.

[173] D. Gabor, "A New Microscopic Principle," *Nature*, vol. 162, p. 680, 1948.

[174] M. E. Haine and T. Mulvey, "The Formation of the Diffraction Image with Electrons in the Gabor Diffraction Microscope," *Journal of the Optical Society of America*, vol. 42, no. 10, p. 763, 1952.

[175] G. Möllenstedt and H. Düker, "Fresnelscher Interferenzversuch mit einem Biprisma für Elektronenwellen," *Die Naturwissenschaften*, vol. 42, no. 2, p. 41, 1955.

[176] J. M. Cowley, "Twenty forms of electron holography," *Ultramicroscopy*, vol. 41, no. 4, pp. 335–348, 1992.

[177] F. Zheng, J. Caron, V. Migunov, M. Beleggia, G. Pozzi, and R. E. Dunin-Borkowski, "Measurement of charge density in nanoscale materials using off-axis electron holography," *Journal of Electron Spectroscopy and Related Phenomena*, vol. 241, p. 146881, 2020.

[178] M. R. McCartney, "Characterization of charging in semiconductor device materials by electron holography," *Journal of Electron Microscopy*, vol. 54, no. 3, pp. 239–242, 2005.

[179] D. Cooper, J.-P. Barnes, J.-M. Hartmann, and F. Bertin, "Off-axis electron holography of Si semiconductors prepared using FIB milling," *Journal of Physics: Conference Series*, vol. 209, p. 012062, 2010.

[180] M. Lehmann and H. Lichte, "Tutorial on Off-Axis Electron Holography," *Microscopy and Microanalysis*, vol. 8, no. 6, pp. 447–466, 2002.

[181] H. Lichte and M. Lehmann, "Electron holography: a powerful tool for the analysis of nanostructures," vol. 123 of *Advances in Imaging and Electron Physics*, pp. 225–256, Academic Press, 2002.

[182] A. Tonomura, "Electron Holography," in *Electron Holography*, pp. 29–49, Springer, 1999.

[183] W. Koch, A. Lubk, F. Grossmann, H. Lichte, and R. Schmidt, "Coherent and incoherent effects on the imaging and scattering process in transmission electron microscopy and off-axis electron holography," *Ultramicroscopy*, vol. 110, no. 11, pp. 1397–1403, 2010.

[184] T. Harvey, F. Yasin, J. Chess, J. Pierce, R. Dos Reis, V. Özdöl, P. Ercius, J. Ciston, W. Feng, N. Kotov, B. McMorran, and C. Ophus, "Interpretable and Efficient Interferometric Contrast in Scanning Transmission Electron Microscopy with a Diffraction-Grating Beam Splitter," *Physical Review Applied*, vol. 10, no. 6, 2018.

[185] W. Hoppe and G. Strube, "Beugung in inhomogenen Primärstrahlenwellenfeld. II. Lichtoptische Analogieversuche zur Phasenmessung von Gitterinterferenzen," *Acta Crystallographica Section A*, vol. 25, no. 4, pp. 502–507, 1969.

[186] W. Hoppe, "Beugung im inhomogenen Primärstrahlwellenfeld. III. Amplitudenâ und Phasenbestimmung bei unperiodischen Objekten," *Acta Crystallographica Section A*, vol. 25, no. 4, pp. 508–514, 1969.

[187] W. Hoppe, "Trace structure analysis, ptychography, phase tomography," *Ultramicroscopy*, vol. 10, no. 3, pp. 187–198, 1982.

[188] R. Bates and J. Rodenburg, "Sub-ångström transmission microscopy: A Fourier transform algorithm for microdiffraction plane intensity information," *Ultramicroscopy*, vol. 31, no. 3, pp. 303–307, 1989.

[189] J. M. Rodenburg, B. Mc Callum, and P. Nellist, "Experimental tests on double-resolution coherent imaging via STEM," *Ultramicroscopy*, vol. 48, pp. 304–314, 1993.

[190] P. D. Nellist, B. C. McCallum, and J. M. Rodenburg, "Resolution beyond the 'information limit' in transmission electron microscopy," *Nature*, vol. 374, no. 6523, pp. 630–632, 1995.

[191] P. D. Nellist and J. M. Rodenburg, "Electron Ptychography. I. Experimental Demonstration Beyond the Conventional Resolution Limits," *Acta Crystallographica Section A: Foundations of Crystallography*, vol. 54, no. 1, pp. 49–60, 1998.

[192] H. N. Chapman, "Phase-retrieval X-ray microscopy by Wigner-distribution deconvolution," *Ultramicroscopy*, vol. 66, no. 3–4, pp. 153–172, 1996.

[193] J. Lee and G. Barbastathis, "Denoised Wigner distribution deconvolution via low-rank matrix completion," *Optics Express*, vol. 24, no. 18, pp. 20069–20079, 2016.

[194] H. Yang, I. MacLaren, L. Jones, G. T. Martinez, M. Simson, M. Huth, H. Ryll, H. Soltau, R. Sagawa, Y. Kondo, *et al.*, "Electron ptychographic phase imaging of light elements in crystalline materials using Wigner distribution deconvolution," *Ultramicroscopy*, vol. 180, pp. 173–179, 2017.

[195] O. Krivanek and P. Mooney, "Applications of slow-scan CCD cameras in transmission electron microscopy," *Ultramicroscopy*, vol. 49, no. 1, pp. 95–108, 1993.

[196] Y. Jia, B. Mollon, P. Mooney, M. Pan, B. McGinn, M. Azimi, N. Cabilan, A. Gubbens, and M. Lent, "A New High Speed, High Resolution 2k x 2k CCD Camera for Transmission Electron Microscopes," *Microscopy and Microanalysis*, vol. 17, no. S2, p. 814–815, 2011.

[197] T. J. Pennycook, G. T. Martinez, P. D. Nellist, and J. C. Meyer, "High dose efficiency atomic resolution imaging via electron ptychography," *Ultramicroscopy*, vol. 196, pp. 131–135, 2019.

[198] H. Yang, L. Jones, H. Ryll, M. Simson, H. Soltau, Y. Kondo, R. Sagawa, H. Banba, I. MacLaren, and P. D. Nellist, "4D STEM: High efficiency phase contrast imaging using a fast pixelated detector," *Journal of Physics: Conference Series*, vol. 644, p. 012032, 2015.

[199] J. Song, C. S. Allen, S. Gao, C. Huang, H. Sawada, X. Pan, J. Warner, P. Wang, and A. I. Kirkland, "Atomic Resolution Defocused Electron Ptychography at Low Dose with a Fast, Direct Electron Detector," *Scientific Reports*, vol. 9, no. 1, p. 3919, 2019.

[200] A. M. Maiden, G. R. Morrison, B. Kaulich, a. Gianoncelli, and J. M. Rodenburg, "Soft X-ray spectromicroscopy using ptychography with randomly phased illumination," *Nature Communications*, vol. 4, p. 1669, 2013.

[201] A. M. Maiden, J. M. Rodenburg, and M. J. Humphry, "Optical ptychography: a practical implementation with useful resolution," *Optics Letters*, vol. 35, no. 15, pp. 2585–2587, 2010.

[202] G. B. Kitchen, P. S. Cunningham, T. M. Poolman, M. Iqbal, R. Maidstone, M. Baxter, J. Bagnall, N. Begley, B. Saer, T. Hussell, *et al.*, "The clock gene Bmal1 inhibits macrophage motility, phagocytosis, and impairs defense against pneumonia," *Proceedings of the National Academy of Sciences*, vol. 117, no. 3, pp. 1543–1551, 2020.

[203] S. Cao, P. Kok, P. Li, A. M. Maiden, and J. M. Rodenburg, "Modal decomposition of a propagating matter wave via electron ptychography," *Physical Review A*, vol. 94, p. 063621, 2016.

[204] Z. Chen, M. Odstrcil, Y. Jiang, Y. Han, M.-H. Chiu, L.-J. Li, and D. A. Muller, "Mixed-state electron ptychography enables sub-angstrom resolution imaging with picometer precision at low dose," *Nature Communications*, vol. 11, no. 1, pp. 1–10, 2020.

[205] S. Gao, P. Wang, F. Zhang, G. T. Martinez, P. D. Nellist, X. Pan, and A. I. Kirkland, "Electron ptychographic microscopy for three-dimensional imaging," *Nature Communications*, vol. 8, no. 1, p. 163, 2017.

[206] K. Ooe, T. Seki, Y. Ikuhara, and N. Shibata, "High contrast STEM imaging for light elements by an annular segmented detector," *Ultramicroscopy*, vol. 202, pp. 148–155, 2019.

[207] H. Yang, T. J. Pennycook, and P. D. Nellist, "Efficient phase contrast imaging in STEM using a pixelated detector. Part II: Optimisation of imaging conditions," *Ultramicroscopy*, vol. 151, pp. 232–239, 2015.

[208] W. Wan, J. Su, X. D. Zou, and T. Willhammar, "Transmission electron microscopy as an important tool for characterization of zeolite structures," *Inorganic Chemistry Frontiers*, vol. 5, no. 11, pp. 2836–2855, 2018.

[209] J. Hou, C. W. Ashling, S. M. Collins, A. Krajnc, C. Zhou, L. Longley, D. N. Johnstone, P. A. Chater, S. Li, M.-V. Coulet, *et al.*, "Metal-organic framework crystal-glass composites," *Nature Communications*, vol. 10, no. 1, pp. 1–10, 2019.

[210] P. M. Pelz, R. Bücker, G. Ramm, H. Venugopal, G. Kassier, D. Eggert, P.-H. Lu, R. E. Dunin-Borkowski, and R. J. D. Miller, "Electron Ptychography of Single Biological Macromolecules," *Microscopy and Microanalysis*, vol. 25, no. S2, pp. 72–73, 2019.

[211] L. Zhou, J. Song, J. S. Kim, X. Pei, C. Huang, M. Boyce, L. Mendonça, D. Clare, A. Siebert, C. S. Allen, *et al.*, "Low-dose phase retrieval of biological specimens using cryo-electron ptychography," *Nature Communications*, vol. 11, no. 1, pp. 1–9, 2020.

[212] A. V. Crewe, "Scanning electron microscopes: is high resolution possible?," *Science (New York, N.Y.)*, vol. 154, no. 3750, pp. 729–738, 1966.

[213] O. L. Krivanek, J. P. Ursin, N. J. Bacon, G. J. Corbin, N. Dellby, P. Hrncirik, M. F. Murfitt, C. S. Own, and Z. S. Szilagyi, "High-energy-resolution monochromator for aberration-corrected scanning transmission electron microscopy/electron energy-loss spectroscopy," *Philosophical Transactions of the Royal Society A: Mathematical, Physical and Engineering Sciences*, vol. 367, no. 1903, pp. 3683–3697, 2009.

[214] F. Hage, D. Kepaptsoglou, Q. Ramasse, and L. Allen, "Phonon Spectroscopy at Atomic Resolution," *Physical Review Letters*, vol. 122, no. 1, p. 016103, 2019.

[215] O. Krivanek, N. Dellby, and A. Lupini, "Towards sub-Å electron beams," *Ultramicroscopy*, vol. 78, no. 1–4, pp. 1–11, 1999.

[216] W. O. Saxton, "Observation of lens aberrations for very high-resolution electron microscopy. I. Theory," *Journal of Microscopy*, vol. 179, no. 2, pp. 201–213, 1995.

[217] D. Typke and K. Dierksen, "Determination of image aberrations in high-resolution electron microscopy using diffractogram and cross-correlation methods," *Optik (Stuttgart)*, vol. 99, no. 4, pp. 155–166, 1995.

[218] R. N. Bracewell and R. N. Bracewell, *The Fourier Transform and its Applications*, vol. 31999. McGraw-Hill New York, 1986.

[219] J. Rodenburg and A. Maiden, "Ptychography," in *Springer Handbook of Microscopy*, pp. 819–904, Springer International Publishing, 2019.

[220] H. Rose, "Nonstandard imaging methods in electron microscopy," *Ultramicroscopy*, vol. 2, pp. 251–267, 1976.

[221] W. H. Press, B. P. Flannery, S. A. Teukolsky, and W. T. Vetterling, "Numerical Recipes in C, Cambridge University," 1992.

[222] M. Huth, R. Ritz, C. M. O'Leary, I. Griffiths, P. Nellist, and H. Soltau, "Ultrafast Ptychography with 7500 Frames per Second," *Microscopy and Microanalysis*, vol. 25, no. S2, pp. 40–41, 2019.

[223] H. Sawada, T. Sannomiya, F. Hosokawa, T. Nakamichi, T. Kaneyama, T. Tomita, Y. Kondo, T. Tanaka, Y. Oshima, Y. Tanishiro, *et al.*, "Measurement method of aberration from Ronchigram by autocorrelation function," *Ultramicroscopy*, vol. 108, no. 11, pp. 1467–1475, 2008.

[224] E. Liberti, G. T. Martinez, C. M. O'Leary, P. D. Nellist, and A. I. Kirkland, "Three-dimensional Electron Ptychography of Catalyst Nanoparticles using Combined HAADF STEM and Atom Counting," *Microscopy and Microanalysis*, vol. 25, no. S2, p. 8–9, 2019.

[225] M. Humphry, B. Kraus, A. Hurst, A. Maiden, and J. Rodenburg, "Ptychographic electron microscopy using high-angle dark-field scattering for sub-nanometre resolution imaging," *Nature Communications*, vol. 3, p. 730, 2012.

[226] T. J. Pennycook, G. T. Martinez, C. M. O'Leary, H. Yang, and P. D. Nellist, "Efficient Phase Contrast Imaging via Electron Ptychography, a Tutorial," *Microscopy and Microanalysis*, vol. 25, no. S2, p. 2684–2685, 2019.

[227] B. H. Savitzky, L. A. Hughes, S. E. Zeltmann, H. G. Brown, S. Zhao, P. M. Pelz, E. S. Barnard, J. Donohue, L. R. DaCosta, T. C. Pekin, *et al.*, "py4DSTEM: a software package for multimodal analysis of four-dimensional scanning transmission electron microscopy datasets." arXiv:2003.09523v1 [cond-mat.mtrl-sci], 2020.

[228] I. Lobato and D. V. Dyck, "MULTEM: A new multislice program to perform accurate and fast electron diffraction and imaging simulations using Graphics Processing Units with CUDA," *Ultramicroscopy*, vol. 156, pp. 9–17, 2015.

[229] R. Danev and K. Nagayama, "Applicability of thin film phase plates in biological electron microscopy," *Biophysics*, vol. 2, pp. 35–43, 2006.

[230] H. Yang, P. Ercius, P. D. Nellist, and C. Ophus, "Enhanced phase contrast transfer using ptychography combined with a pre-specimen phase plate in a scanning transmission electron microscope," *Ultramicroscopy*, vol. 171, pp. 117–125, 2016.

[231] L. von Heimendahl, "Structure and dynamics of a two-component metallic glass," *Journal of Physics F: Metal Physics*, vol. 9, no. 2, pp. 161–169, 1979.

[232] M. Treacy and J. Gibson, "Variable coherence microscopy: A rich source of structural information from disordered materials," *Acta Crystallographica Section A: Foundations of Crystallography*, vol. 52, no. 2, pp. 212–220, 1996.

[233] T. Seki, Y. Ikuhara, and N. Shibata, "Theoretical framework of statistical noise in scanning transmission electron microscopy," *Ultramicroscopy*, vol. 193, pp. 118–125, 2018.

[234] D. Zhang, Y. Zhu, L. Liu, X. Ying, C.-E. Hsiung, R. Sougrat, K. Li, and Y. Han, "Atomic-resolution transmission electron microscopy of electron beam-sensitive crystalline materials," *Science*, vol. 359, no. 6376, pp. 675–679, 2018.

[235] L. Liu, Z. Chen, J. Wang, D. Zhang, Y. Zhu, S. Ling, K.-W. Huang, Y. Belmabkhout, K. Adil, Y. Zhang, *et al.*, "Imaging defects and their evolution in a metal–organic framework at sub-unit-cell resolution," *Nature Chemistry*, vol. 11, no. 7, pp. 622–628, 2019.

[236] M. Pan and P. Crozier, "Low-dose high-resolution electron microscopy of zeolite materials with a slow-scan CCD camera," *Ultramicroscopy*, vol. 48, no. 3, pp. 332–340, 1993.

[237] K. Yoshida and Y. Sasaki, "Optimal accelerating voltage for HRTEM imaging of zeolite," *Journal of Electron Microscopy*, vol. 62, no. 3, pp. 369–375, 2012.

[238] V. Ortalan, A. Uzun, B. C. Gates, and N. D. Browning, "Direct imaging of single metal atoms and clusters in the pores of dealuminated HY zeolite," *Nature Nanotechnology*, vol. 5, no. 7, pp. 506–510, 2010.

[239] X. Sang and J. M. LeBeau, "Revolving scanning transmission electron microscopy: Correcting sample drift distortion without prior knowledge," *Ultramicroscopy*, vol. 138, pp. 28–35, 2014.

[240] P. Coppens, "Electron density from X-ray diffraction," *Annual Review of Physical Chemistry*, vol. 43, no. 1, pp. 663–692, 1992.

[241] S. Chandrasekhar, "Extinction in X-ray crystallography," *Advances in Physics*, vol. 9, no. 36, pp. 363–386, 1960.

[242] J.-M. Zuo, M. Kim, M. O'Keeffe, and J. Spence, "Direct observation of d-orbital holes and Cu–Cu bonding in Cu_2O," *Nature*, vol. 401, no. 6748, pp. 49–52, 1999.

[243] P. N. Nakashima, A. E. Smith, J. Etheridge, and B. C. Muddle, "The Bonding Electron Density in Aluminum," *Science*, vol. 331, no. 6024, pp. 1583–1586, 2011.

[244] C. M. O'Leary, C. S. Allen, C. Huang, J. S. Kim, E. Liberti, P. D. Nellist, and A. I. Kirkland, "Phase reconstruction using fast binary 4D STEM data," *Applied Physics Letters*, vol. 116, no. 12, p. 124101, 2020.

[245] P. Cachier, X. Pennec, and N. Ayache, "Fast Non Rigid Matching by Gradient Descent: Study and Improvements of the "Demons" Algorithm," *INRIA*, RR-3706, ffinria-00072962, 1999.

[246] H. Wang, L. Dong, J. O'Daniel, R. Mohan, A. S. Garden, K. K. Ang, D. A. Kuban, M. Bonnen, J. Y. Chang, and R. Cheung, "Validation of an accelerated 'demons' algorithm for deformable image registration in radiation therapy," *Physics in Medicine & Biology*, vol. 50, no. 12, p. 2887, 2005.

[247] R. Szeliski, "Image Alignment and Stitching: A Tutorial," *Foundations and Trends in Computer Graphics and Vision*, vol. 2, no. 1, p. 1–104, 2006.

[248] C. T. Metz, S. Klein, M. Schaap, T. van Walsum, and W. J. Niessen, "Non-rigid registration of dynamic medical imaging data using nD+ t B-splines and a groupwise optimization approach," *Medical Image Analysis*, vol. 15, no. 2, pp. 238–249, 2011.

[249] T. J. Pennycook, L. Jones, H. Pettersson, J. Coelho, M. Canavan, B. Mendoza-Sanchez, V. Nicolosi, and P. D. Nellist, "Atomic scale dynamics of a solid state chemical reaction directly determined by annular dark-field electron microscopy," *Scientific Reports*, vol. 4, p. 7555, 2014.

[250] A. B. Yankovich, B. Berkels, W. Dahmen, P. Binev, S. I. Sanchez, S. A. Bradley, A. Li, I. Szlufarska, and P. M. Voyles, "Picometre-precision analysis of scanning transmission electron microscopy images of platinum nanocatalysts," *Nature Communications*, vol. 5, no. 1, pp. 1–7, 2014.

[251] L. Jones, S. Wenner, M. Nord, P. H. Ninive, O. M. Løvvik, R. Holmestad, and P. D. Nellist, "Optimising multi-frame ADF-STEM for high-precision atomic-resolution strain mapping," *Ultramicroscopy*, vol. 179, pp. 57–62, 2017.

[252] L. Jones, S. Wang, X. Hu, S. ur Rahman, and M. R. Castell, "Maximising the resolving power of the scanning tunneling microscope," *Advanced structural and chemical imaging*, vol. 4, no. 1, pp. 1–8, 2018.

[253] A. Roche, X. Pennec, G. Malandain, and N. Ayache, "Rigid registration of 3-D ultrasound with MR images: a new approach combining intensity and gradient information," *IEEE Transactions on Medical Imaging*, vol. 20, no. 10, pp. 1038–1049, 2001.

[254] B. H. Savitzky, I. El Baggari, C. B. Clement, E. Waite, B. H. Goodge, D. J. Baek, J. P. Sheckelton, C. Pasco, H. Nair, N. J. Schreiber, *et al.*, "Image reg-

istration of low signal-to-noise cryo-STEM data," *Ultramicroscopy*, vol. 191, pp. 56–65, 2018.

[255] A. A. Cole-Rhodes and R. D. Eastman, "Gradient descent approaches to image registration," in *Image Registration for Remote Sensing*, p. 265–275, Cambridge University Press, 2011.

[256] A. N. Penn, R. Trappen, N. Mottaghi, C.-Y. Huang, A. Kumar, M. Holcomb, and J. M. LeBeau, "Explaining the Magnetic Properties of Oxygen Deficient LSMO Thin Films by iDPC," *Microscopy and Microanalysis*, vol. 25, no. S2, pp. 1748–1749, 2019.

[257] A. B. Yankovich, C. Zhang, A. Oh, T. J. Slater, F. Azough, R. Freer, S. J. Haigh, R. Willett, and P. M. Voyles, "Non-rigid registration and non-local principle component analysis to improve electron microscopy spectrum images," *Nanotechnology*, vol. 27, no. 36, p. 364001, 2016.

[258] S. Wenner, L. Jones, C. D. Marioara, and R. Holmestad, "Atomic-resolution chemical mapping of ordered precipitates in Al alloys using energy-dispersive X-ray spectroscopy," *Micron*, vol. 96, pp. 103–111, 2017.

[259] L. Jones, A. Varambhia, R. Beanland, D. Kepaptsoglou, I. Griffiths, A. Ishizuka, F. Azough, R. Freer, K. Ishizuka, D. Cherns, *et al.*, "Managing dose-, damage-and data-rates in multi-frame spectrum-imaging," *Microscopy*, vol. 67, no. suppl_1, pp. i98–i113, 2018.

[260] S. J. Clark, M. D. Segall, C. J. Pickard, P. J. Hasnip, M. I. Probert, K. Refson, and M. C. Payne, "First principles methods using CASTEP," *Zeitschrift für Kristallographie – Crystalline Materials*, vol. 220, no. 5/6, pp. 567–570, 2005.

[261] T. Naginey, *Applications of electronic structure theory in electron microscopy*. DPhil Thesis, University of Oxford, 2018.

[262] S. Van Aert, A. De Backer, G. T. Martinez, B. Goris, S. Bals, G. Van Tendeloo, and A. Rosenauer, "Procedure to count atoms with trustworthy single-atom sensitivity," *Physical Review B*, vol. 87, p. 064107, 2013.

[263] G. Martinez, A. Rosenauer, A. D. Backer], J. Verbeeck, and S. V. Aert], "Quantitative composition determination at the atomic level using model-based high-angle annular dark field scanning transmission electron microscopy," *Ultramicroscopy*, vol. 137, pp. 12–19, 2014.

[264] "Absolute Integrator." http://lewysjones.com/software/absolute-integrator/. Accessed: 6th May, 2020.

[265] R. Fernandez-Leiro and S. H. Scheres, "Unravelling biological macromolecules with cryo-electron microscopy," *Nature*, vol. 537, no. 7620, pp. 339–346, 2016.

[266] J. Frank, "Advances in the field of single-particle cryo-electron microscopy over the last decade," *Nature Protocols*, vol. 12, no. 2, pp. 209–212, 2017.

[267] J. Miao, P. Ercius, and S. J. L. Billinge, "Atomic electron tomography: 3D structures without crystals," *Science*, vol. 353, no. 6306, 2016.

[268] M. Born and E. Wolf, *Principles of Optics: Electromagnetic Theory of Propagation, Interference and Diffraction of Light*. Elsevier, 2013.

[269] G. Behan, E. C. Cosgriff, A. I. Kirkland, and P. D. Nellist, "Three-dimensional imaging by optical sectioning in the aberration-corrected scanning transmission electron microscope," *Philosophical Transactions of the Royal Society A: Mathematical, Physical and Engineering Sciences*, vol. 367, no. 1903, pp. 3825–3844, 2009.

[270] K. van Benthem, A. R. Lupini, M. Kim, H. S. Baik, S. Doh, J.-H. Lee, M. P. Oxley, S. D. Findlay, L. J. Allen, J. T. Luck, *et al.*, "Three-dimensional imaging

of individual hafnium atoms inside a semiconductor device," *Applied Physics Letters*, vol. 87, no. 3, p. 034104, 2005.

[271] H. Yang, J. Lozano, T. Pennycook, L. Jones, P. Hirsch, and P. Nellist, "Imaging screw dislocations at atomic resolution by aberration-corrected electron optical sectioning," *Nature Communications*, vol. 6, no. 1, pp. 1–7, 2015.

[272] C. Placek and E. North, "Uranium Dioxide Nuclear Fuel," *Industrial & Engineering Chemistry*, vol. 52, no. 6, pp. 458–464, 1960.

[273] H. Stehle, H. Assmann, and F. Wunderlich, "Uranium dioxide properties for LWR fuel rods," *Nuclear Engineering and Design*, vol. 33, no. 2, pp. 230–260, 1975.

[274] T. Petit, C. Lemaignan, F. Jollet, B. Bigot, and A. Pasturel, "Point defects in uranium dioxide," *Philosophical Magazine B*, vol. 77, no. 3, pp. 779–786, 1998.

[275] L.-F. He, M. Gupta, C. A. Yablinsky, J. Gan, M. A. Kirk, X.-M. Bai, J. Pakarinen, and T. R. Allen, "In situ TEM observation of dislocation evolution in Kr-irradiated UO_2 single crystal," *Journal of Nuclear Materials*, vol. 443, no. 1–3, pp. 71–77, 2013.

[276] S. Rennie, E. Lawrence Bright, J. E. Darnbrough, L. Paolasini, A. Bosak, A. D. Smith, N. Mason, G. H. Lander, and R. Springell, "Study of phonons in irradiated epitaxial thin films of UO_2," *Physical Review B*, vol. 97, p. 224303, 2018.

[277] M. Amaya, J. Nakamura, and T. Fuketa, "The effects of irradiation condition and microstructural change on lattice parameter, crystal lattice strain and crystallite size in high burnup UO_2 pellet," *Journal of Nuclear Materials*, vol. 392, no. 3, pp. 439–446, 2009.

[278] C. Sabathier, G. Martin, A. Michel, G. Carlot, S. Maillard, C. Bachelet, F. Fortuna, O. Kaitasov, E. Oliviero, and P. Garcia, "In-situ TEM observation of nano-void formation in UO_2 under irradiation," *Nuclear Instruments and Methods in Physics Research Section B: Beam Interactions with Materials and Atoms*, vol. 326, pp. 247–250, 2014.

[279] D. Van Dyck and M. Op de Beeck, "A simple intuitive theory for electron diffraction," *Ultramicroscopy*, vol. 64, no. 1–4, pp. 99–107, 1996.

[280] A. Resnick, K. Mitchell, J. Park, E. B. Farfán, and T. Yee, "Thermal transport study in actinide oxides with point defects," *Nuclear Engineering and Technology*, vol. 51, no. 5, pp. 1398–1405, 2019.

[281] B. Song, Z. Ding, C. S. Allen, H. Sawada, F. Zhang, X. Pan, J. Warner, A. I. Kirkland, and P. Wang, "Hollow Electron Ptychographic Diffractive Imaging," *Physical Review Letters*, vol. 121, p. 146101, 2018.

[282] A. Stevens, L. Luzi, H. Yang, L. Kovarik, B. Mehdi, A. Liyu, M. Gehm, and N. Browning, "A sub-sampled approach to extremely low-dose STEM," *Applied Physics Letters*, vol. 112, no. 4, p. 043104, 2018.

[283] A. Stevens, H. Yang, W. Hao, L. Jones, C. Ophus, P. D. Nellist, and N. D. Browning, "Subsampled STEM-ptychography," *Applied Physics Letters*, vol. 113, no. 3, p. 033104, 2018.

[284] G. Zeng, "Facial Recognition with Singular Value Decomposition," in *Advances and Innovations in Systems, Computing Sciences and Software Engineering*, (Dordrecht), pp. 145–148, Springer Netherlands, 2007.

[285] H. S. Prasantha, H. L. Shashidhara, and K. N. Balasubramanya Murthy, "Image Compression Using SVD," in *International Conference on Computational*

Intelligence and Multimedia Applications (ICCIMA 2007), vol. 3, pp. 143–145, 2007.

[286] P. Potapov and A. Lubk, "Optimal principal component analysis of STEM XEDS spectrum images," *Advanced Structural and Chemical Imaging*, vol. 5, no. 1, p. 4, 2019.